UNIVERSITY OF CALIFORNIA, MERCED

Dispersions of Semiconductor Nanoparticles in Thermotropic Liquid Crystal: From Optical Modification to Assisted Self-Assembly

A dissertation submitted in the partial satisfaction

of the requirements for the degree of

Doctor of Philosophy

in

Physics

by

Andrea L. Rodarte

Committee in Charge

Professor Tao Ye, Chair

Professor Ajay Gopinathan

Professor Sayantani Ghosh

Professor Linda S. Hirst

Professor Roummel Marcia

2014

The dissertation of Andrea L. Rodarte is approved, and it is acceptable in quality and form for publication on microfilm and electronically:

Sayantani Ghosh

Linda S. Hirst

Roummel Marcia

Ajay Gopinathan

Tao Ye Chair

University of California, Merced

2014

To my parents. For all those trips to the science center, and for teaching me it's ok to strive to be best.

To Jussi. Having a husband for a lab mate turned out nicely. But mostly because even when I didn't believe in myself you believed enough for both of us.

Contents

List of Figures

List of Tables

1 Acknowledgments

I would like to thank my advisors Sayantani Ghosh and Linda S. Hirst for their encouragement and support throughout my graduate studies. They have served as incredible mentors for me both academically and personally. I owe much of my success to their guidance and high expectations and will not soon forget the lessons they taught me.

I would also like to thank Dr. Jason Hein and his group for their work functionalizing quantum dots with mesogenic ligands. They enabled us to take the next logical step in our research and I greatly appreciate the hours his students put into making the compounds for us.

I would also like to thank my lab mates for their collaboration and assistance. In particular, I would like to thank Christopher Ferri for his superb work automating our data collection and processing and Ronald Pandolfi for his assistance taking X-ray scattering data. I would also like to thank Corrine Gray, Laurel Shcherbatyuk, Lauren Edwards and Fredie Cisneros for their contributions to my work. The time and effort they put into our projects will not be forgotten.

I also acknowledge the funding support I was fortunate to have during my studies. UC MERI, UC MEXUS and UC Merced for the internal funding opportunities that they offer. My final years would have been much different if not for the Faculty Mentor Fellowship and President's Dissertation Year Fellowship.

Chapter 6 was previously published has been published under A. L. Rodarte, C. Gray, L. S. Hirst and S. Ghosh, Physical Review B, 85, 035430, 2012.[1] Copyright 2012 by the American Physical Society.

Chapter 7 was previously published in RSC Advances. Link to article [2] I would like to acknowledge my co-authors Georgiy V. Shcherbatyuk, Laurel Shcherbatyuk, Linda S. Hirst and Sayantani Ghosh. Chapter 8 was previously published in the Journal of Materials Chemistry C. Link to article [3] I would like to acknowledge my co-authors Ronald J. Pandolfi, Sayantani Ghosh and Linda S. Hirst. The dissertation author is first author on the publications. The published work is reproduced by permission of the Royal Society of Chemistry.

Chapter 9 was previously published in Liquid Crystals. [4] I would like to acknowledge my co-authors Fredy Cisneros, Linda S. Hirst and Sayantani Ghosh. The dissertation author is first author on the publications. The published work is reproduced by permission of Taylor & Francis.

Chapter 10 was published in ChemPhysChem. [5] I would like to acknowledge my co-authors Zachary S. Nuño, Blessing H. Cao, Ronald J. Pandolfi, Makiko T. Quint, Sayantani Ghosh, Jason E. Hein, and Linda S. Hirst. The dissertation author is the first author on the publication. The published work is reproduced under license 3414441005473.

2 Curriculum Vitae

Andrea L. Rodarte

Ph.D. Candidate, Physics
University of California, Merced, School of Natural Sciences
5200 N. Lake Rd. Merced, Ca 95344
Advisors: Dr. Linda S. Hirst and Dr. Sayantani Ghosh

Education

- University of California, Merced, Merced, Ca. August 2009 - current
  - Ph.D. in Physics (GPA=4.0/4.0; 4.0=A)
- California State University, Fresno, Fresno, Ca. September 1999 - June 2004
  - B.S. in Physics, June 2004 (GPA=3.49/4.0; 4.0=A)

Appointments and elected positions

- Women in Science and Engineering at UC Merced (WiSE) August 2010 - current
  - Founding member and Vice President
- Society of Physics Students (SPS) September 2001 - June 2004

Fellowships and Awards

- President's Dissertation Year Fellowship AY 2013-14
  - Awarding institution: University of California, Merced
- Physics Summer Research Fellowship Summer 2013
  - Awarding institution: University of California, Merced
- Faculty Mentor Program Fellowship AY 2012-13
  - Awarding institution: University of California, Merced
- Graduate and Research Council (GRC) fellowship Summer 2012
  - Awarding institution: University of California, Merced
- Margaret Burbidge Award for Best Experimental Research by a Graduate Student, Second Place Fall 2012
  - Awarding institution: APS-California/Nevada Section

- Graduate Division General Fellowship Spring 2012
  - Awarding Institution: University of California, Merced
- Graduate and Research Council (GRC) fellowship Summer 2011
  - Awarding Institution: University of California, Merced
- Dan David Fellowship Spring 2011
  - Awarding Institution: University of California, Merced
- UC Merced Energy Research Institute (MERI) Research Fellowship Fall 2011
  - Awarding Institution: University of California, Merced
- Margaret Burbidge Award for Best Experimental Research by a Graduate Student, First Place Fall 2011
  - Awarding institution: APS-California/Nevada Section

Experience

- University of California, Merced Graduate Research Assistant June 2010 - current
  - Investigate dispersion of quantum dots in a liquid crystal matrix. Experience in polarized optical microscopy, atomic force microscopy, differential scanning calorimetry, scanning photoluminescence spectroscopy, confocal microscopy, small angle x-ray scattering.
- University of California, Merced Teaching Assistant Aug. 2009 – May 2012
  - Taught bi-weekly discussion sections for Intro to Electricity and Magnetism and Thermal Physics
- Voltage Multipliers, Inc. Visalia, Ca. Process Engineer August 2005 - July 2009
  - Design and fabrication of high voltage diodes. Experience in semiconductor doping, vacuum evaporation, clean-room environment, sputtering.

Publications in refereed journals

1. A. L. Rodarte, C. Gray, L. S. Hirst and S. Ghosh, "Spectral and polarization modulation of quantum dot emission in a one-dimensional liquid crystal photonic cavity". Phys. Rev. B 85, 03540 (2012).
2. A. L. Rodarte, G. G. L. Ferri, C. Grey, L. S. Hirst and S. Ghosh, "Directed assembly and in-situ manipulation of semiconductor quantum dots in liquid crystal matrices". Proceedings of SPIE (2012).

3. A. L. Rodarte, G. V. Shcherbatyuk, L. Shcherbatyuk, L. S. Hirst and S. Ghosh, "Dynamics of spontaneous emission of quantum dots in a one-dimensional cholesteric liquid crystal photonic cavity". RSC Advances 2, 12759 (2012).

4. A. L. Rodarte, R. Pandolfi, S. Ghosh and L. S. Hirst, "Quantum dot/liquid crystal composite materials: Self-assembly driven by liquid crystal phase transition templating". J. Mat. Chem. 1, 5527 (2013).

5. A. L. Rodarte, Z. S. Nuño, B. H. Cao, R. J. Pandolfi, M. T. Quint, S. Ghosh, J. E. Hein and L. S. Hirst, "Tuning quantum dot organization in liquid crystal for robust photonic applications". Chem. Phys. Chem. 15(7), 1413 (2014).

6. A. L. Rodarte, F. Cisneros, L. S. Hirst and S. Ghosh, "Cholesteric liquid crystal based luminescent solar concentrator" Liquid Crystals DOI:10.1080/02678292.2014.924163.

7. J. J. Amaral, J. Wan, A. L. Rodarte, M. T. Quint, R. J. Pandolfi, M. Scheibner, L. S. Hirst and S. Ghosh, "Magnetic field induced brightening in liquid crystal synergized magnetic and semiconducting nanoparticle composite assemblies" Advanced Functional Materials (submitted).

8. A. L. Rodarte, B. Cao, Z. Nuno, R. J. Pandolfi, M. T. Quint, S. Ghosh, J. Hein and L. S. Hirst, "Nanoparticle shells templated by liquid crystal phase separation" Nature Chemistry (in preparation).

Conference and workshop presentations

1. "Self Assembly of CdSe Quantum Dots in Cholesteric Liquid Crystal" A. L. Rodarte, L. S. Hirst, S. Ghosh. Presentation to the APS California-Nevada Section. Pasadena, Ca. October, 2010.

2. "WiSE Graduate Student Speaker Series" A. L. Rodarte. Presentation to Women in Science and Engineering at UC Merced. Merced, Ca. February, 2011.

3. "Directed Assembly of CdSe/ZnS Quantum Dots in Cholesteric Liquid Crystal Matrix" A. L. Rodarte, L. S. Hirst, S. Ghosh. Presentation to the APS March Meeting. Dallas, Tx. March, 2011.

4. "Spectral and polarization modulation of quantum dot emission in a one-dimensional liquid crystal photonic cavity" A. L. Rodarte, L. S. Hirst, S. Ghosh. Presentation to the APS California/Nevada Section. October, 2011.

5. "Spectral and polarization modulation of quantum dot emission in a one-dimensional liquid crystal photonic cavity" A. L. Rodarte, L. S. Hirst, S. Ghosh. Presentation to the APS March Meeting. March, 2012.

6. "Directed Assembly and In situ Manipulation of Semiconductor Quantum Dots in Liquid Crystal Matrices" A. L. Rodarte, L. S. Hirst, S. Ghosh. Presentation to MRS Spring Meeting. April, 2012.

7. "Quantum dot suspensions in a liquid crystal matrix" A. L. Rodarte, S. Ghosh and L. S. Hirst. Presentation to the 2012 International Liquid Crystal Conference. August, 2012.

8. “Ordering Quantum Dot Clusters via Nematic Liquid Crystal Defects” A. L. Rodarte, R. Pandolfi, L. S. Hirst and S. Ghosh. Presentation to the APS California/Nevada Section. October, 2012.

9. “Liquid Crystal Phase Transition driven three-dimensional Quantum Dot Organization” A. L. Rodarte, R. Pandolfi, L. S. Hirst and S. Ghosh. Presentation to the APS March Meeting. March 2013.

10. “Liquid Crystal Phase Transitions and Defects to Sort and Soft-Assemble Microstructures” A. L. Rodarte, L. S. Hirst and S. Ghosh. Presentation to the APS March Meeting. March 2014.

Presented Posters

1. “Wavelength Grating Created by CdSe/ZnS Quantum Dots Dispersed in Chiral Nematic Liquid Crystal Media” A. L. Rodarte, S. Ghosh, L. S. Hirst. Student Research Poster Competition. Merced, Ca. April, 2011.

2. “Improvement of Luminescent Solar Concentrators Using Vertically Aligned Dye “ M. Ricketts, A. L. Rodarte, L. Jiang, R. Winston, L. S. Hirst. UC Solar Symposium. Merced, Ca. Dec, 2011.

3. “Utilizing 1-D Photonic Cavity of a Cholesteric Liquid Crystal to Increase Efficiency of Solar Concentrators” A. L. Rodarte, S. Ghosh, L. S. Hirst. UC Solar Symposium. Davis, Ca. May, 2013.

Society Memberships

American Physical Society

3 Abstract of the Dissertation

Dispersions of Semiconductor Nanoparticles in Thermotropic Liquid Crystal: From Optical Modification to Assisted Self-Assembly

by

Andrea L. Rodarte

Doctor of Philosophy in Physics

University of California, Merced, 2014

Prof. Tao Ye, Chair

Prof. Linda S. Hirst and Prof. Sayantani Ghosh, Advisors

Abstract

The interaction of semiconducting quantum dot nanoparticles (QDs) within thermotropic liquid crystalline (LC) materials are studied in this thesis. LC materials are ideal for bottom-up organization of nanoparticles as an active matrix that can be externally manipulated via electric or magnetic fields. In addition, the optical properties of QDs can be modified by the surrounding LC resulting in novel devices such as a quantum dot/liquid crystal laser. The first system studies the dispersion of spherical nanoparticles in the phase. The dispersion is investigated with the use of polarized optical microscopy, fluorescence microscopy and confocal scanning microscopy. Quantum dots well dispersed in the isotropic phase are expelled from ordered domains of LC at the phase transition. Under controlled conditions, the majority of QDs in the system can form ordered three dimensional assemblies that are situated at defect points in the liquid crystal. The internal order of the assemblies is probed utilizing Förster resonance energy transfer (FRET), combined with small angle X-ray scattering (SAXS). Furthermore, the location of these assemblies can be predetermined with the use of beads as defect nucleation points in the cell.

The interaction of QDs in a cholesteric liquid crystal (CLC) is also investigated. The reflection band created by the periodic change of index of refraction in a planar aligned CLC acts as a 1-D photonic cavity when the CLC is doped with a low concentration of QDs. A Cano-wedge cell varies the pitch of the CLC leading to the formation of Grandjean steps. This spatially tunes the photonic stop band, changing the resonance condition and continuously altering both the emission wavelength and polarization state of the QD ensemble. Using high resolution spatially and spectrally resolved photoluminescence measurements, the emission is shown to be elliptically polarized and that the tilt of the ellipse, while dependent on the emission wavelength, additionally varies with distance across the Grandjean steps. Using ultrafast spectroscopic techniques the time-resolved emission from QD ensembles in CLC matrices with either planar or homeotropic alignment is observed. In the case of planar alignment and a well-defined spectral stop band the emergence of a second, faster decay time of less than 2 ns is observed. This short recombination pathway is observed only in samples where the QD emission spectrum partially overlaps the CLC stop band by 50% or more. Samples prepared with homeotropic alignment do not have a stop band and, consequently, do not lead to spectral or

dynamical modulation of the QD emission. These observations indicate that coupling between the excitonic and the photonic cavity modes results in an enhancement and modulation of spontaneous emission in the liquid crystal medium. This work opens up the possibility of designing new QD based optical devices, such as tunable single photon sources, where spatial control of wavelength and polarization of the embedded QDs would allow great flexibility and added functionalities.

For hybrid materials such as soft tunable photonic devices like liquid crystal lasers, stable dispersions of nanoparticles in LC are desired. For the system we investigate functionalizing the nanoparticles with LC like ligands. Isotropic and mesogenic ligands attached to the surface of CdSe (core only) and CdSe/ZnS (core/shell) QDs. The mesogenic ligand's flexible arm structure enhances ligand alignment with the local liquid crystal director, enhancing QD dispersion in the isotropic and nematic phases. To characterize QD dispersion on different length scales, fluorescence microscopy, x-ray scattering and scanning confocal photoluminescent imaging are used. These combined techniques demonstrate that the LC-modified QDs do not aggregate into the dense clusters observed for dots with simple isotropic ligands when dispersed in liquid crystal, but loosely associate in a fluid-like aggregate with an average inter-particle spacing of >10nm.

The major goal in this research is to identify the strengths and weaknesses of utilizing liquid crystal materials for hybrid and metamaterials. The techniques developed within this thesis will be useful for the next step of bottom-up metamaterial fabrication.

4 Introduction

4.1 Liquid Crystalline Materials

Liquid crystal (LC) materials are a class of materials that exhibit at least one ordered mesophase that lies between the isotropic liquid phase and the crystalline phase in which the molecules have short range order. The molecules that create LC phases are anisotropic which means that there is some sort of directionality to its physical properties. We will consider molecules that have one axis that is different from the others, though spherical particles can be considered anisotropic if they are charged on one side or have one side that is more hydrophobic than the other. Liquid crystalline materials are birefringent, often colorful and can be used in many applications. They were first observed by Reinitzer in 1888 [6] when he observed that cholesterol appeared to have two melting points. Heated to one temperature the material would melt from solid into a cloudy liquid but heated to a higher temperature that cloudy mixture would melt again and become a clear liquid. The optical and electrical properties of LC materials make them useful for electronic displays [7], as temperature sensors [8] and as a lasing medium [9, 10, 11]. Liquid crystal materials can be grouped into two classifications, thermotropic and lyotropic. Thermotropic LCs change phase with temperature and have distinct "melting points" like the cholesterol observed by Reinitzer. Lyotropic liquid crystals are formed by molecules dissolved in a solvent. The phase of the LC is dependent on the concentration of the solvent. In this dissertation we will work only with thermotropic LC materials. We use rodlike molecules that form LC phases at room temperature. At high temperatures the anisotropic molecules have no order and form an isotropic or liquid phase. As the temperature is reduced the molecules form a fluid but ordered liquid crystal phase

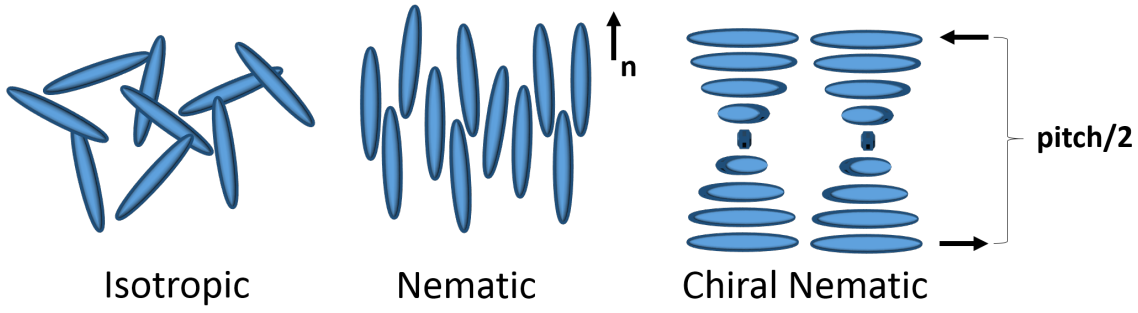

Figure 1: Cartoon of liquid crystal phases and the direction of the director, **n**, denoted by the arrow

The least ordered liquid crystal mesophase is the nematic phase (see Figure 1). In the nematic phase it is energetically favorable for the molecules to align with one another while remaining fairly fluid with the ability to diffuse. They have short range orientational order in which the molecules tend to point in one direction which is called the director axis, **n**. When placed on a glass slide to create a cell, the director may shift over long length scales unless the cell is given an alignment layer. Alignment can be induced in one of two ways, parallel with the cell, planar, or perpendicular to the surface of the cell, homeotropic. To induce a planar alignment, a thin film polymer such as polyvinyl alcohol (PVA) is applied and given a rubbing direction usually by dragging a cloth gently over the surface. The rod shaped molecules will tend to align with the rubbing direction close to the interface. If the system is cooled slowly from the isotropic phase into the nematic phase, the alignment will propagate throughout the sample giving a very uniform LC domain. Homeotropic alignment can

be achieved by treating the glass with a surfactant such as hexadecyltrimethylammonium bromide (CTAB). The treated glass then has hydrocarbon chains oriented perpendicular to the surface which makes it energetically favorable for the LC to also align perpendicular to the surface.

The chiral nematic or cholesteric phase adds another layer of order. The molecules have an inherent handedness and as such the director axis rotates through the bulk material. When aligned in a planar cell the cholesteric forms a helix whose axis of rotation is perpendicular to the surface of the cell. The distance over which the director rotates 360º is the pitch of the material.[12] The index of refraction in the system changes periodically, creating a one dimensional photonic band gap. The photonic band gap prevents light from propagating within the band gap and selectively reflects light incident on the device.[13]

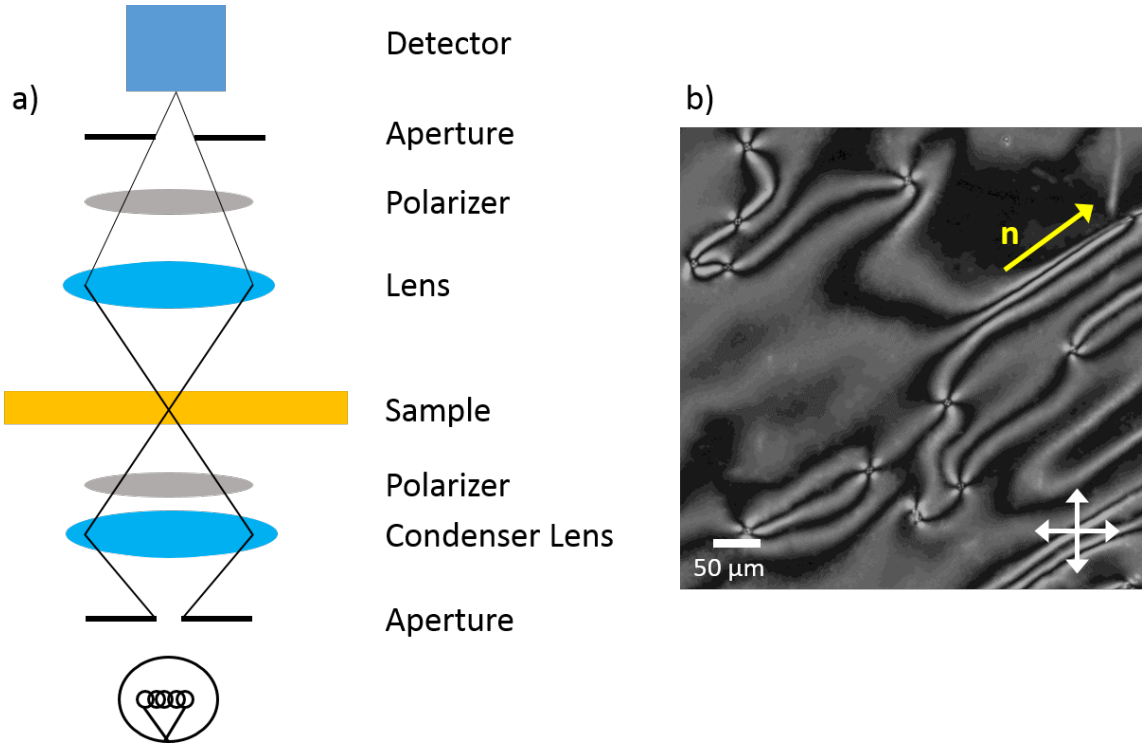

Figure 2: a) Schematic of polarized optical microscope setup and b) characteristic Schlieren texture of nematic LC

Because the molecules are anisotropic the liquid crystal phases are birefringent. When light enters a birefringent material the component of the light that is parallel to the axis of anisotropy of the medium is subject to the extraordinary refractive index, n_e, and propagates at a different speed than the component of light perpendicular to the axis of anisotropy which is subject to the ordinary refractive index, n_o. The birefringence of the material is defined as $\Delta n = n_e - n_o$ The difference in propagation creates a phase difference defined by $\Delta\phi = \frac{2\pi}{\lambda} d(n_o - n_e)$ where d is the thickness of the material and λ is the incident wavelength. Because the thickness of the material affects the phase difference, liquid crystal materials can be used to generate any polarization state by selecting the adequate thickness. Liquid crystal phases can be characterized by placing them in a polarized optical microscope in order to view the birefringence textures that are created when viewed between crossed polarizers as in Figure 2a. Without a birefringent sample between the polarizers the incoming light

is extinguished by the analyzer and the sample appears dark. When a planar aligned nematic liquid crystal is placed between the polarizers the LC acts as a waveguide and rotates the polarization of light, allowing some light to pass through the analyzing polarizer. The orientation of the molecules in a planar aligned sample can be visualized using polarized optical microscopy (POM) because dark and light areas correspond to the orientation of the director. In Figure 2b we see the characteristic Schlieren texture. The dark areas correspond with the director axis oriented parallel to one of the polarizers, the bright areas correspond to an area where the director is oriented at another angle and point defects have two or four brushes surrounding the defect. When white light is used in the microscope, the polarization of different wavelengths is rotated by differing amounts, creating a colorful and bright defect texture. Since the retardation of the light is dependent on the thickness of the sample, the thickness of a sample of known birefringence can be measured by matching the color with the Michel-Levy chart (Figure 3).[14]

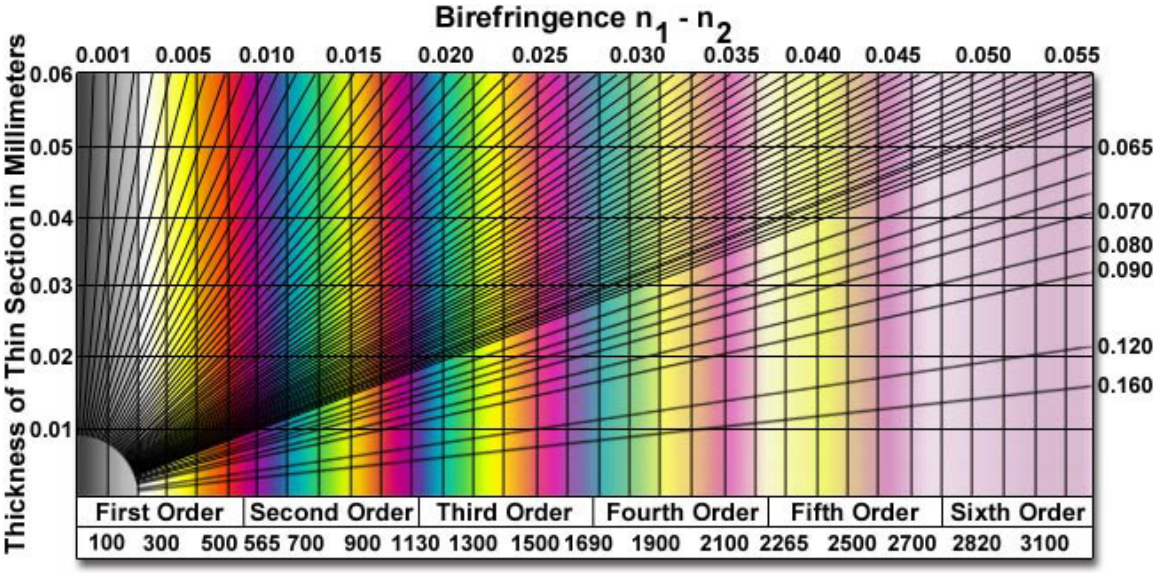

Figure 3: The Michel-Levy chart can be used to determine the thickness of a known liquid crystal based on the color observed between crossed polarizers.[14]

In addition to being birefringent, the anisotropy of the LC molecules leads to the material having dielectric anisotropy. The dielectric constant or permittivity, ε, of a material expresses the extent to which an insulating material will be polarized by an electric field. Isotropic materials have one dielectric constant but in an ordered anisotropic material such as a LC, the direction of the electric field is important. The material has one dielectric constant for electric fields parallel to the long axis, $\varepsilon_{\parallel}$, and a different one for electric fields perpendicular to the long axis, $\varepsilon_{\perp}$. From these we can define the dielectric anisotropy for a material, $\Delta\varepsilon = \varepsilon_{\parallel} - \varepsilon_{\perp}$ where materials with positive $\Delta\varepsilon$ will align with long axis in the direction of the applied electric field and those with negative $\Delta\varepsilon$ will align with the long axis perpendicular to the applied field[12]. A threshold exists below which an electric field can be applied to a bulk LC sample with no change. Above the threshold the molecules will reorient to align with the applied field. The reorientation of the director with applied field is call the Fréedericksz transition. This transition is used to create liquid crystal displays.

There are many configurations that can be used to create a liquid crystal display but all of them exploit the Fréedericksz transition to switch pixels on and off. The twisted nematic is one of the

simplest configurations for an LCD where a 90º twist is induced in the pixel by applying orthogonal planar alignment layers on the pixel surfaces. The 90º twist acts as a waveguide, efficiently rotating the polarization of light so that the natural state is a bright state as in Figure 4a. When an electric field is applied the LC molecules rotate to align with the field and the polarization of light is no longer rotated and the pixel appears dark as in Figure 4b. The twisted nematic displays can be designed to operate in both transmissive and reflective modes with good contrast. However, they have a poor viewing angle because they are best viewed from straight on. These displays were used often in early digital watch and calculator displays. Other display modes such as super twisted nematic, in plane switching and the vertical alignment display use different orientations of LC molecules and field geometry but all function from the same idea: the birefringence of a LC can be varied using an electric field, switching the pixel state from bright to dark.

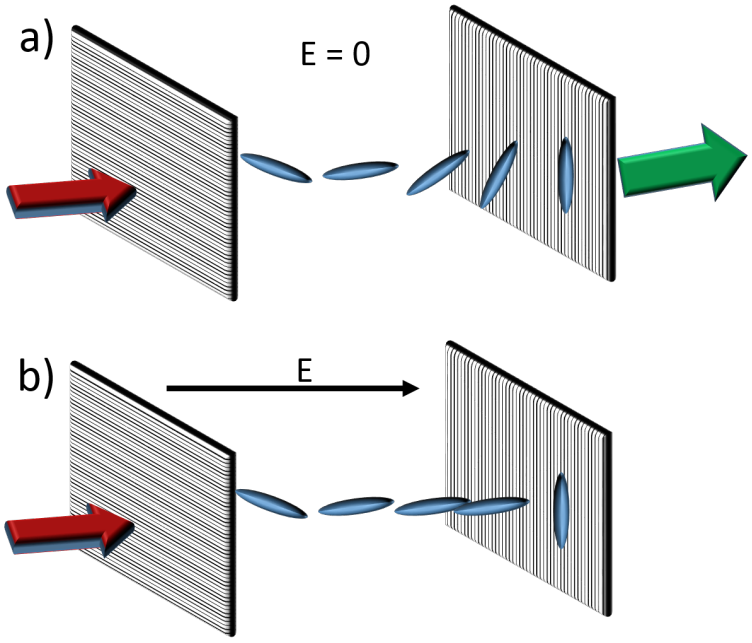

Figure 4: Cartoon of a twisted nematic LCD pixel in the a) on and b) off positions.

4.2 Quantum Dots

Quantum dots (QDs), sometimes referred to as 'artificial atoms,' are semiconductor nanostructures that confine the motion of the electron-hole pairs, or excitons. In a bulk material an electron can freely move throughout the valence band of the material. When the size of the nanostructure shrinks to smaller than about 10 nanometers the structure is comparable to or smaller than the natural wavelength scale of the electron-hole pair. This confines the exciton in one, two or three dimensions depending on the nanostructure (quantum wells, wires and dots respectively) causing the energy levels to become quantized which can be described by the particle-in-a-box model. [15] The particle-in-a box model considers an arbitrary particle of mass $m_o$in a potential well of length L. Where the potential is $V(x) = 0$ for $0 < x < L$ and $V(x) = \infty$ for $x < 0$ and $x > L$. Solving the Schrodinger

equation with boundary conditions results in wavefunctions:

$$\Psi_n(x) = \sqrt{\frac{2}{L}} sin\left(\frac{n\pi x}{L}\right)$$

where n identifies the energy level. The energy of the particle is given by:

$$E_n = \frac{\pi^2\hbar^2}{2mL^2}n^2$$

Note that the energy of the particle is proportional to $1/L^2$ and is thus strongly dependent on the size of the particle. Due to this quantum confinement the material's band gap is increased over the bulk band gap as:

$$E_{gap}^{QD} \approx E_{gap} + \frac{\hbar^2\pi^2}{2L^2}\left[\frac{1}{m_e} + \frac{1}{m_h}\right]$$

where E_{gap} is the band gap energy of the bulk material, m_e is the effective mass of an electron moving in the material and m_h is the effective mass of a "hole" in the material[16]. The band gap of the quantum dot is increased as the diameter of the nanoparticle decreases as seen in Fig 5. This strong size dependence is an advantage in QDs since the emission can easily be tuned by changing the nanoparticle size. For example, CdSe quantum dots of different sizes can emit from 450 to 650 nm, across the visible spectrum.

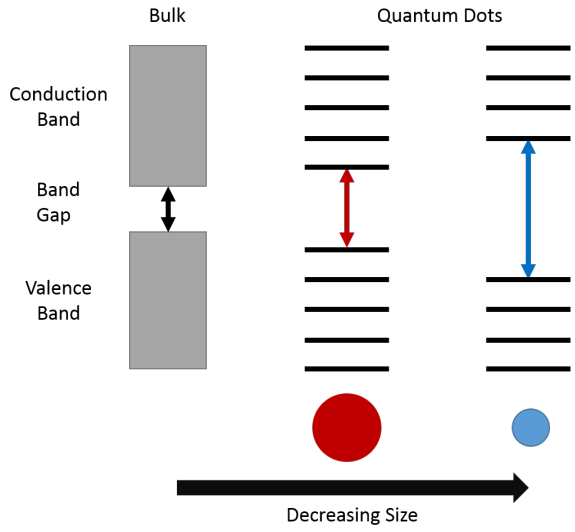

Figure 5: Bulk semiconductor has a band gap defined by the material. As the size decreases into the nanometer range quantum confinement creates discrete energy states and a size dependent QD energy gap.

There are several ways to synthesize QDs. In general, the dots can be epitaxially grown or chemically synthesized as colloidal particles. Molecular beam epitaxy (MBE) utilizes the lattice mismatch of the selected semiconductor with the surrounding material to create small, often ordered, QD islands. [17] QDs can also be created using lithography techniques. [18] This dissertation focuses on colloidal QDs. Colloidal QDs can be synthesized with a core of semiconductor material

capped with a shell of another material with a larger band gap. Without the passivation layer the surface of the quantum dot provides sites for nonradiative recombination, reducing quantum yield or the ratio of photons absorbed to photons emitted through fluorescence. Capping the QD with a thin shell of larger bandgap acts to eliminate all the energy levels inside the gap. Additionally, organic ligands are attached to the surface to confer solubility and prevent aggregation in solution. [19]

Applications of QDs are numerous due to their tuneability. They have been used in biological analysis as fluorophores as they are bright and less susceptible to photobleaching than traditional dyes. [20] QDs have also been used increasingly in next generation solar cells [21] as well as light emitting diodes, [22] lasers, [23] and information processing. [24] Separation between quantum dots can be indirectly measured using Förster resonance energy transfer (FRET). An excited donor quantum dot, a smaller dot with a large band gap, may transfer its energy to a larger acceptor quantum dot with a smaller band gap through non-radiative dipole-dipole coupling. The efficiency of the energy transfer is $E_{FRET} = \frac{R_0^6}{R_0^6+R^6}$ where R_0 is the Förster radius at which the FRET efficiency is 50% and R is the separation between the donor and acceptor. In addition, the FRET efficiency can be expressed through the lifetime of the quantum dots. Lifetime is the average time the QD remains in the excited state before recombining and emitting a photon. FRET efficiency can be expressed in terms of the donor lifetime, τ_D, and lifetime in the presence of the acceptor, τ_{DA}: $E_{FRET} = 1 - \frac{\tau_{DA}}{\tau_D}$ Because the efficiency of transfer is extremely sensitive to small changes in distance, FRET can be used as a spectroscopic ruler.

4.3 Motivation

It has been discussed that nanoparticles have their own size dependent characteristics that differ from bulk material, however it is important to note that ensembles of nanoparticles can have properties that differ even from the individual nanoparticles. For example semiconductor quantum dots are shown to have high carrier mobility and high conductivity at low separation distances[25]. Metallic nanoparticles individually act as an insulator but when the inner particle separation is reduce an insulator to metal transition is observed. A material can be constructed using metallic nanoparticles with a set distance between particle surfaces, around 12Å, that acts as an insulator until it is compressed and the separation drops below 5Å. The material can then act as a conductor until the compression is removed, the particles are returned to their original separation and the material becomes an insulator again[26]. Because collective particles have characteristics different from individual nanoparticles, arrays of nanoparticles make a multitude of applications possible. For example, in ordered arrays of quantum dots discrete energy levels split into minibands which can enhance light absorption and carrier transport in solar cells allowing for a higher efficiency next-generation solar cell[27]. Arrays of metallic nanoparticles can be used as a subwavelength microscope sensor allowing us to observe things that an optical microscope could not[28]. Theoretical simulations indicate that gold nanoparticles lattices yield a paramagnetic response despite having nonmagnetic constituents[29].

Many applications require a well ordered superlattice, where lattice points consist of nanoparticles instead of atoms. Current methods for producing high quality super lattices often involve lithography or focused ion beam technique. These top-down processes can be extremely expensive, time-consuming and it can only be prepared on small scales on specific substrates. Bottom-up processes colloidal nanoparticles that are manipulated into an ordered array. These processes are more cost-effective can be prepared on numerous substrates and have the potential for large-scale production. Bottom-up processes include nano manipulation in which individual nanoparticles are

physically placed into their final position[30]. Solutions of colloidal nanoparticles can be used to create ordered arrays by either chemically removing the nanoparticles from the solution [31] or by evaporation of the solvent in a controlled manner leaving behind ordered nanoparticles[32]. What is missing from the current methods is the ability to reconfigure or switch completed assemblies which is where liquid crystal materials enter the picture. Liquid crystal materials allow for *in situ* manipulation via external electric and magnetic fields as well as temperature variation. Early work with liquid crystal quantum dot mixtures used indirect measurements of the nanoparticles and indicated the presence of long anisotropic strands of quantum dots[33]. Work with discotic quantum dots in a nematic liquid crystal revealed that anisotropic quantum dots aligned in stacks and those stacks can be rotated by switching the liquid crystal with an electric field[34]. It has been observed that quantum dots in aligned smectic liquid crystals tend to align with the rubbing direction of the cell[35]. The Hegmann group has done extensive work with modifying surface ligands of gold nanoparticles on dots facilitate better dispersion in liquid crystal materials[36, 37].

In this dissertation we will use liquid crystal materials as the template for organizing nanoparticles. This is ideal because the molecular orientation can be changed using temperature, electric field and magnetic fields. Because the size of the nanoparticles is on the same order as the size of the crystal molecules, by changing the molecular orientation of liquid crystal molecules we should be able to change the orientation of the quantum dots. We will use quantum dots as the nanoparticle dopant because it allows fluorescence and confocal microscopy to identify the position and spectrum of the assembled nanoparticles. We will not need to rely on indirect measurements to tell us where the quantum dots may be in the system, the emission will tell us the exact location.

In this work, chapter 5 describes the experimental methods used in this dissertation. Chapter 6 explores a system of quantum dots dispersed in cholesteric liquid crystal. When the cholesteric stop-band is tuned to the quantum dot emission the intensity of the emission is increased and the ensemble wavelength shifts due to the resonance condition at the edge of the stop-band. Chapter 7 further explores this resonance, observing the dynamics of the QD emission in the CLC. The cavity coupling is confirmed for systems tuned to resonance.

Chapter 8 explores a system of QDs dispersed in a nematic LC. Through controlled cooling into the nematic phase a homogeneous dispersion of QDs can be formed into closely packed clusters situated at defect points in the LC. The inter-dot spacing within these clusters is determined to be approximately 7.6 nm. Additionally, the location of the clusters is shown to be controllable by nucleating defect points in the LC.

Chapter 9 investigates a system in which the fluorophore is required to be homogeneously distributed in the LC phase. A dye is dispersed in a CLC for use in a luminescent solar concentrator (LSC). The stop-band of the CLC is integrated into the body of the LSC and acts to confine emission and prevent escape from the LSC when the stop-band is tuned with the dye emission. Quantum dots are not suitable for this application and others like it due to their tendency to aggregate in the LC phase. Chapter 10 addresses this issue and covers our endeavors to increase solubility of QD in LC by attaching mesogenic ligands to the surface of the QDs. Chapter 11 summarizes our conclusions and chapter 12 considers future directions for the research.

5 Methods

5.1 Sample Preparation

All samples referenced in this dissertation were prepared with a similar method. CdSe/ ZnS core/shell QDs suspended in toluene (from NN Labs) are added in low weight percentages (.01 to .15 wt %) to liquid crystal. The nematic LC 4'-pentyl'4-biphenylcarbonitrile (5CB from Sigma Aldrich) is used without further purification for nematic samples and it is added to cholesteryl oleyl carbonate (COC from Sigma Aldrich) to create a cholesteric liquid crystal with a tuneable pitch. The LC/toluene/QD mixture is then placed into a bath sonicator that has been heated to 43 ºC which is above the clearing point for both LC materials. The mixture is sonicated for 1 to 8 hours to achieve a homogeneous dispersion of QD in the isotropic LC while at the same time evaporating the excess toluene from the system. For low concentrations, below .1 wt %, the amount of toluene added to a sample will evaporate within 4 hours of sonication. If the toluene is not fully evaporated from the LC it will lower the isotropic to nematic transition temperature and if enough toluene is present the LC will not transition into the nematic phase at room temperature. When higher concentrations are attempted or other solvents are used it is important to test the transition temperature of the LC to ensure the sovent has been removed. Once the dispersion is complete the mixture is removed to a 50 ºC oven to create sample cells. Glass slides are first washed with soap and then sonicated in a progression of acetone, methanol and ethanol for 20 minutes each. The glass should then be rinsed thoroughly with Millipore water and sonicated in the water for 20 minutes. Finally the glass should be blown dry with ultra high purity nitrogen. Clean glass is prepared with an alignment layer depending on the desired orientation of the LC. For planar alignment the glass is spin coated with a 1 wt % aqueous PVA solution and subsequently rubbed with velvet to induce an alignment direction. For homeotropic orientation clean glass is flooded with 5 μM aqueous CTAB solution for one hour and then blown dry with ultra high purity nitrogen. All cells are prepared in the 50 ºC oven to maintain the isotropic phase throughout. Once the cells are completed they are moved to a Linkham LTS350 hotstage in order to control the cooling rate into the LC phase while simultaneously observing the QD fluorescence and LC texture with a Leica DM2500P upright microscope equipped with a Q-image Retiga camera.

5.2 Polarized Optical Microscopy

Polarized optical microscopy (POM) uses the liquid crystal birefringence to observe the characteristic texture associated with each phase brought about by the orientation of the anisotropic molecules. A nematic liquid crystal sandwiched between glass slides without alignment layers does not have long range order throughout the sample. The changing director means some areas will appear bright and some dark, depending on the orientation of the director compared to the crossed polarizers. The texture shown in Figure 6a is the Schlieren texture and is characteristic of the nematic liquid crystal phase with planar orientation. The director of the LC can be visualized using optical microscopy because dark areas correspond to an area where the director is parallel with one of the polarizers while the brightest areas appear where the director is at a 45º to the polarizers. When a planar aligned cell is rotated the bright areas become dark when the director becomes parallel with either of the crossed polarizers. Homeotropically aligned nematic liquid crystal is not birefringent because it is isotropic with respect to the light traveling through the microscope and thus appears dark at all times as shown in Figure 6b. Bright points in the birefringence texture indicate point defects.

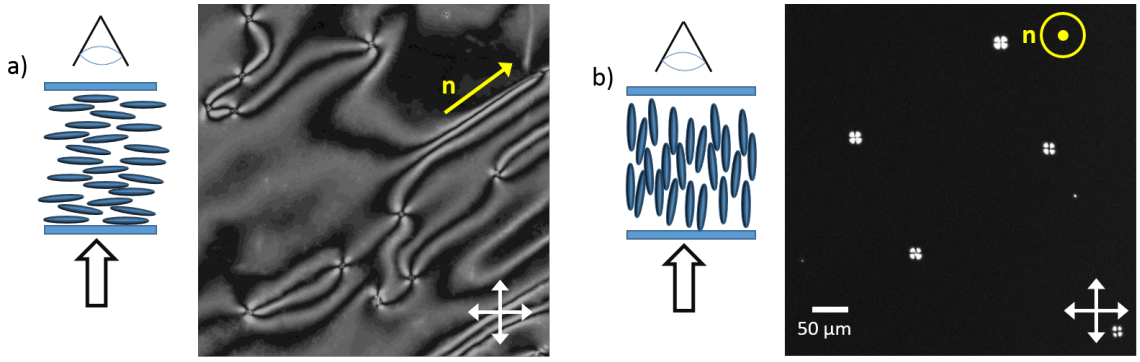

Figure 6: Schematic and POM images for a) planar and b) homeotropic orientations of nematic LC. Defects are observed in the homeotropic alignment as bright points.

Nematic liquid crystal samples have a colorful birefringence texture when observed with white light. The color of the sample is dependent on the thickness of the sample as discussed in section 4.1. Planar oriented cholesteric liquid crystal (CLC) materials however, have a distinct observed color regardless of the thickness of the cell. This color is determined by the pitch of the material and can be tuned by adding nematic LC to the cholesteric LC to expand the pitch as shown in Figure 7. The color and intensity of the cholesteric remains the same when the sample is rotated, it does not change or turn dark. The cholesteric can also be observed using reflection microscopy. When white light is incident upon the cholesteric light outside of the stop band is allowed to pass through while light whose circular polarization matches the handedness of the liquid crystal is reflected.

When quantum dots are mixed into the liquid crystal the dispersion can be observed using fluorescence microscopy as shown in Figure 8. The sample is illuminated from above by light that can excite the quantum dots and the emission from the dots is observed. Figure 8b shows fluorescence images of a quantum dot/liquid crystal dispersion and the corresponding birefringence texture of the liquid crystal is shown in Figure 8c.

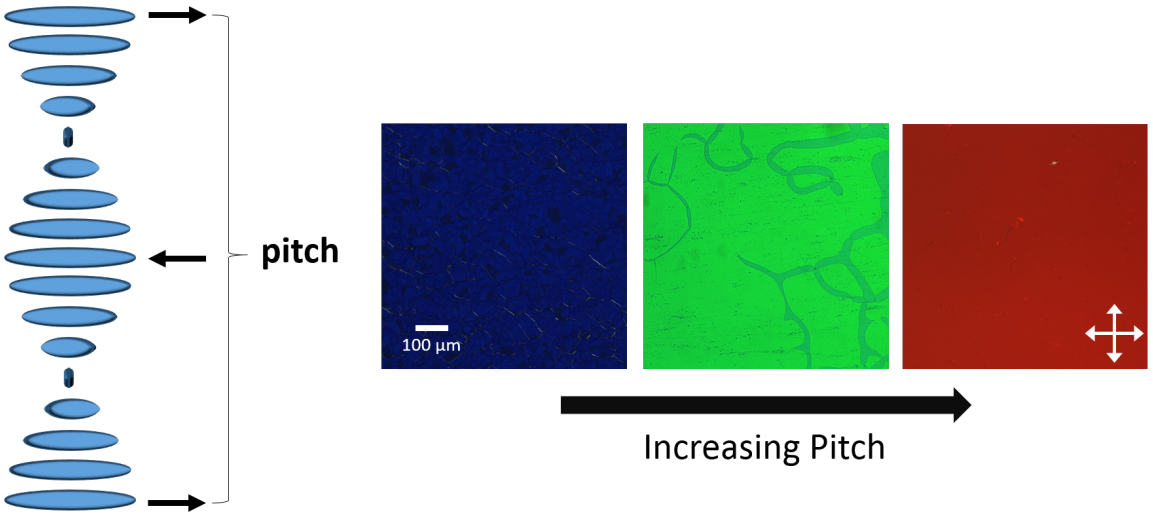

Figure 7: Schematic of planar aligned CLC and POM images of compounds of increasing pitch.

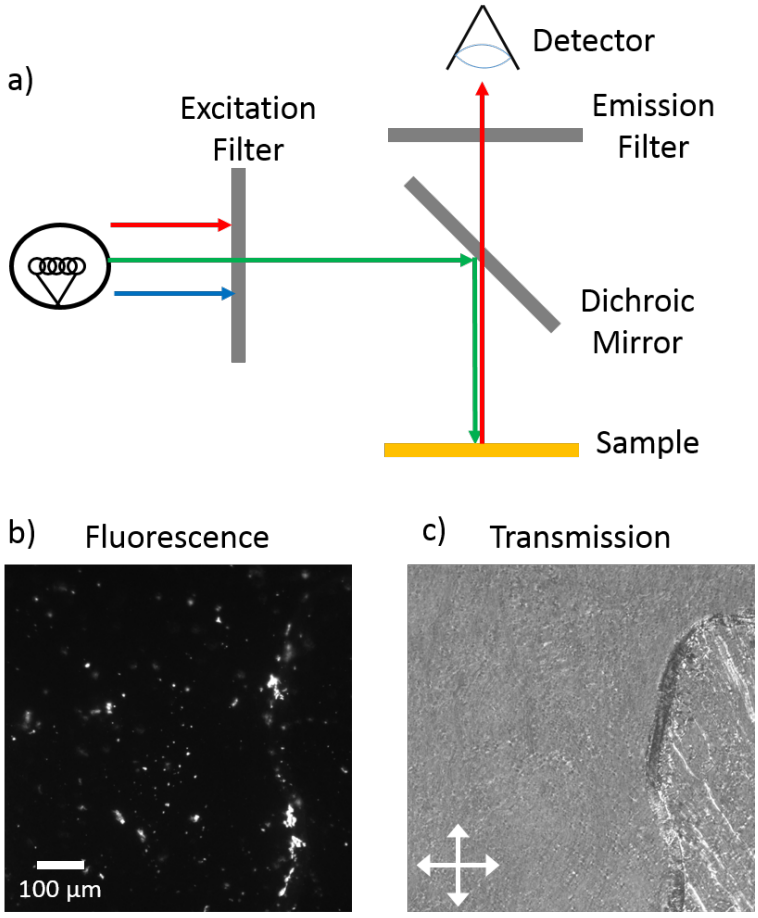

Figure 8: Fluorescence image showing emission from QDs and corresponding polarized transmission image of LC.

5.3 Scanning Photoluminescence Microscopy

For higher resolution imaging we custom built a high-resolution scanning optical microscope to perform a spectral analysis of the materials (Figure 9). The excitation sources are ultra fast, tunable mode-locked lasers that cover the spectral region 350-1200nm. The excitation polarization is controlled by a linear polarizer, a liquid crystal based variable wave plate and a quarter wave plate. Using this system we can determine a linear excitation polarization or modify to use circularly polarized pulses. The excitation beam is focused on the sample through an objective to produce a spot size that is diffraction limited (~600nm). The sample is mounted on a heat controlled motorized 3D scanning stage with step size resolution of 40nm. The emission from the NPs is collected by the same objective and is then directed through polarization analysis optics and is focused on the 100µm aperture of a collection fiber. This acts as a confocal microscope with a lateral resolution of 1µm. The fiber then transmits the PL to a spectrometer coupled to a thermo-electrically cooled CCD camera for spectral analysis. Alternatively, the emission can be directed to a time-correlated single photon counting (TCSPC) detector coupled to a monochromator for spectrally-resolved time-resolved analysis. Spectra from the dots is collected as the sample is raster scanned. Once the scan is completed we analyze the data to produce spatial maps of the peak intensity of the emission as

well as the peak wavelength.

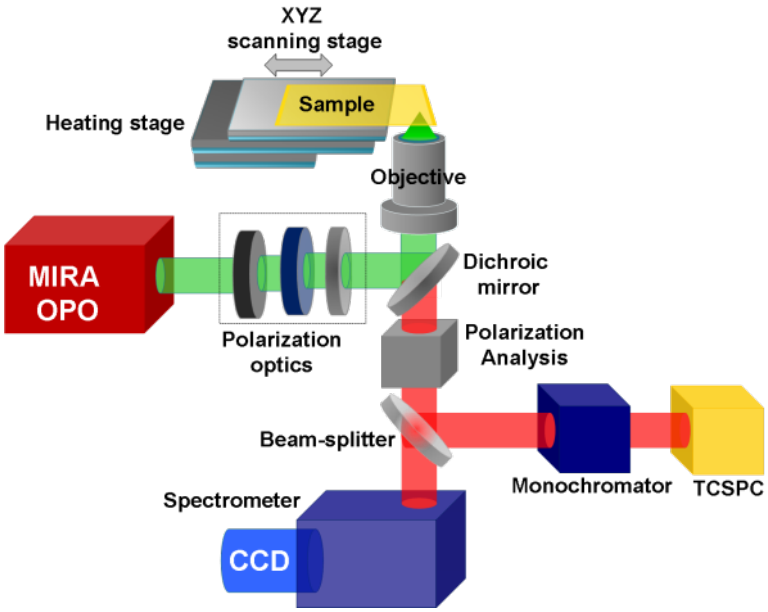

Figure 9: High Resolution scanning optical microscope setup.

5.4 Time-Correlated Single Photon Counting

Time-Correlated Single Photon Counting is used to understand the decay profile of fluorophores. After excitation a quantum dot has a characteristic time before the excitons recombine and light is emitted. Using periodic excitation from a pulsed laser we can collect data over multiple cycles of excitation and emission. The excitation pulse begins the timer and fluorescence from the quantum dot is registered by a single photon avalanche diode. As long as the probability of detecting more than one photon per cycle is low, over several excitation events a histogram can be created which will show the exponential drop of photon counts towards later times. Fitting this decay shows the fluorescence lifetime.

6 Spectral and polarization modulation of quantum dot emission in a one-dimensional liquid crystal photonic cavity

6.1 Introduction

In recent years there has been increasing interest in research at the interface of hard and soft condensed matter. Soft materials, by definition, are easily modified by external forces, such as those exerted by relatively weak electric or magnetic fields. Therefore, they can provide a reconfigurable medium in which nanoscale structures can be assembled and manipulated. One particularly rich area for investigation in this field is the interaction between dispersed particles and liquid crystal (LC) materials. [38] Liquid crystals are complex fluids in which the constituent molecules have orientational and short-range positional order. A large number of distinct LC phases have been observed and the phase exhibited by a specific material depends on several factors, including molecular structure, temperature, or concentration in a solvent. The well-known thermotropic nematic and cholesteric phases have found wide commercial applicability in display technologies and optical modulation devices. One of the key properties of LC materials is their optical anisotropy, which causes them to be birefringent, which can then be tuned by the application of an external electric field. LC materials can also be confined in a device to produce macroscopic ordered domains with a defined optical axis. This combination of molecular switchability and orientational control offers the potential for novel device geometries with highly tunable optical properties.

Dispersions of a variety of particle geometries such as spherical colloids, [39, 40, 41] carbon nanotubes, [42, 43] clay platelets, [44, 45] and other anisotropic morphologies [46, 47] have produced some fascinating results regarding the interplay between particle shape and alignment in the LC phase. Several studies have additionally shown that various LC phases can be used as a template for directed nanoparticle assembly [48, 49] and that the electro-optic response of the LC can be influenced by the addition of nanoparticles.[50, 36] In addition, nanoparticles and colloids have been utilized to control and stabilize topological defects in the anisotropic phase. [51] Recently, stabilization of the LC blue phase over a broad temperature range was achieved using gold nanoparticles localized to the defect cores. [52] While the effects of nanoparticles on an LC host phase have been studied, less is known about how the LC medium affects the properties of the dispersed nanoparticles, and whether it is possible to use LC materials to achieve new types of directed nanoscale assemblies that would manifest novel functionality.

6.2 Experimental Details

In this paper, we focus on using the optical activity of an LC host material to influence the photoluminescence (PL) from embedded semiconducting quantum dots (QDs). [34] Light-matter interactions in confined geometries can result in a wide range of applications, such as optical communications, [53] quantum information processing, [54] and quantum computation schemes. [55] The cholesteric LC phase, composed of rodlike chiral molecules, can be tailored to give rise to such a confined optical system. Similar to the nematic phase, the cholesteric phase has short-range orientational order defined by the LC director but with the additional feature that the director rotates through the bulk material [Fig 10(a)]. [8] The periodicity of this arrangement results in an alternating modulation of the refractive index, creating a one-dimensional photonic band-gap material. The distance required for the director axis to complete a full rotation is called the pitch (p) and it determines the spectral stop band (reflection band) of the cholesteric liquid crystal (CLC). In typical materials with a stop band, all incident light with wavelengths within the band is preferentially

reflected. In CLCs, the chiral geometry adds a special flavor. Even within the stop band only circularly polarized light that has the same handedness as the CLC helix is selectively reflected. Light polarized with the opposite handedness and light with wavelengths outside the stop band are both transmitted through the CLC film. [13, 56] A general case is illustrated in Fig. 10(a) where linearly polarized incident light spectrally matched to the stop band is partly reflected and partly transmitted (as any linear polarization is a sum of right and left circular polarizations). An added attraction of the CLC photonic structure is that it can be modified *in situ* by varying the temperature or applying an electric field, thereby allowing spectral tuning of its optical properties and confinement parameters.

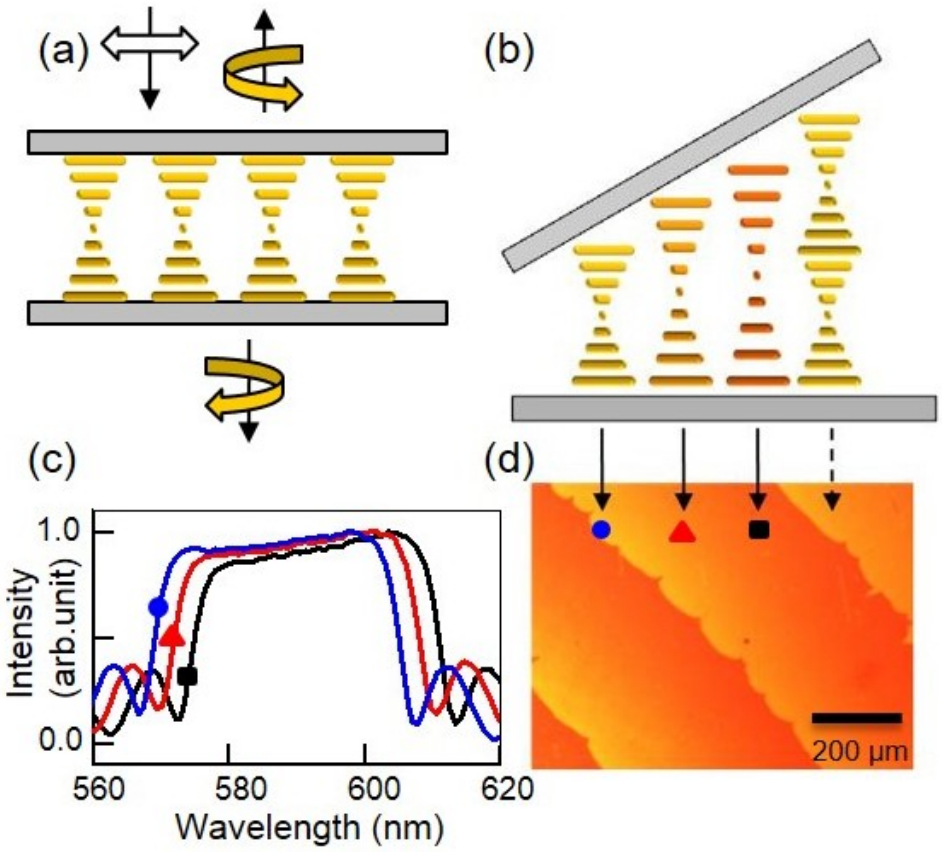

Figure 10: (a) Schematic demonstrating the helical arrangement of the CLC between parallel glass slides. This device geometry selectively reflects and transmits different circular components of linearly polarized incident light. (b) The CLC in a Cano-wedge cell. (c) The spectral stop band (reflection band) of the CLC in the cell at three different points across a single Grandjean step demonstrating the shift of the stop band. (d) Polarized optical microscopy transmission image of the CLC in (b) showing the Grandjean steps. The symbols denote the corresponding stop bands of (c) and the arrows show the corresponding pitch.

If, instead of enclosing the CLC between parallel surfaces, a wedge-shaped arrangement is used, the pitch can be varied across the film, as shown in Fig. 10(b). Commonly known as a Cano-wedge cell, [57, 58] in this device the CLC fills a glass cell where the inside surfaces have been

treated with a rubbed planar alignment layer, polyvinylalcohol (PVA, Sigma Aldrich). Because the LC molecules at the surface are constrained by this alignment layer, the helix stretches as more space is available, elongating the pitch continuously by an amount Δs. When $\Delta s = p/2$, there is a discontinuity as the system relaxes to the initial pitch p but with an added extra half turn [dashed arrow in Fig. 10(b)], before the stretching repeats again. The spectral effects of the changing pitch are shown in Figs. 10(c) and 10(d). In Fig. 10(c), as the pitch increases the corresponding stop band is observed to red-shift. When the cell is viewed between crossed polarizers the CLC texture shows the well-known Grandjean steps in Fig. 10(d). The colors observed from a device placed between crossed polarizers are dependent on the pitch of the material and, in our case, a color variation from yellow to orange is seen across each step. The corresponding spatial positions of the stop bands in Fig. 10(c) in the Grandjean step of Fig. 10(d) are marked using symbols.

For our CLC samples we used mixtures of a chiral LC, cholesteryl oleyl carbonate (COC, Sigma Aldrich), and a nematic LC, 4'-pentyl'4-biphenylcarbonitrile (5CB, Sigma Aldrich). The initial (unstretched) pitch of the CLC depends on the relative concentrations of the chiral component in the nematic material. For the sample shown in Fig. 10(d), a mixture of 60 wt% COC to 40 wt% 5CB was prepared by heated bath sonication. The bath was maintained at a temperature above the isotropic transition temperature for both COC and 5CB (38ºC and 36ºC, respectively) and the sample sonicated for approximately 1 h to ensure complete mixing.To determine the pitch of the material, the mixture was filled between parallel glass plates coated with a rubbed poly-vinyl alcohol (PVA) alignment layer to induce planar alignment of the molecules. The stop band was measured using a Perkin Elmer UV-VIS absorption spectrophotometer. For this sample the pitch was observed to be approximately 590 nm at the center of the stop band [curve marked with solid circle in Fig. 10(c)]. After preparation of the desired cholesteric material, CdSe/ZnS core-shell QDs (N-N Labs, emission peak at 609 nm) were added at a concentration of 0.2 mg/ml and the mixture was sonicated for an additional 3 h at the same elevated temperature. The final mixture was then filled into a Cano-wedge cell at 50ºC before cooling on a controlled heating stage (Linkam LTS350) at a rate of 1ºC/min to room temperature. On verifying the presence of the Grandjean steps using polarized optical microscopy, spectroscopic measurements were carried out using a custom-made diffraction-limited scanning confocal microscope with an optical resolution of 600 nm and a continuous-wave 532-nm diode laser as the excitation source. The QD PL was collected by an Acton 300i spectrometer and dispersed onto a thermoelectrically cooled CCD (spectral resolution $\sim$0.18 nm). By raster scanning selected regions of the sample, spatially resolved PL maps were created to monitor the variation of both emission intensity and wavelength with position.

6.3 Results and Discussion

Figure 11 shows three spatially resolved maps of the peak wavelength (λ_{PEAK}) of QD emission measured across a region of the sample that demonstrated clear Grandjean steps when imaged using polarized optical microscopy. In Fig. 11(a) λ_{PEAK} varies across the sample following the Grandjean step pattern closely. The difference in λ_{PEAK} from the beginning (marked "L") to the end (marked "R") of a step is approximately 7 nm, increasing from left to right. The sample is then heated past the isotropic transition temperature (to 43ºC) and the scan repeated [Fig. 11(b)]. Now we observe that the prior systematic wavelength gradient is replaced by a random distribution of λ_{PEAK}, as is expected from QDs suspended in an isotropic mixture. When cooled back into the CLC phase (25ºC), another PL scan [Fig. 11(c)] shows that the associated λ_{PEAK} gradient has returned. While the emission wavelengths appear slightly blue shifted overall in Fig. 11(c), the pattern and directionality are similar to those observed in Fig. 11(a). The blue shift is most likely a result of photo-oxidation of the

QDs under irradiation. [59] Photoluminescence intensity maps corresponding to each of the three experimental stages do not exhibit this stripe formation either in the CLC or the isotropic phase. However, from the clear similarities between the QD spectral emission patterns of Figs. 11(a) and 11(c) and the CLC defect texture of Fig. 10(d), it is obvious that there is a connection between the Grandjean steps and the measured QD PL emission stripes.

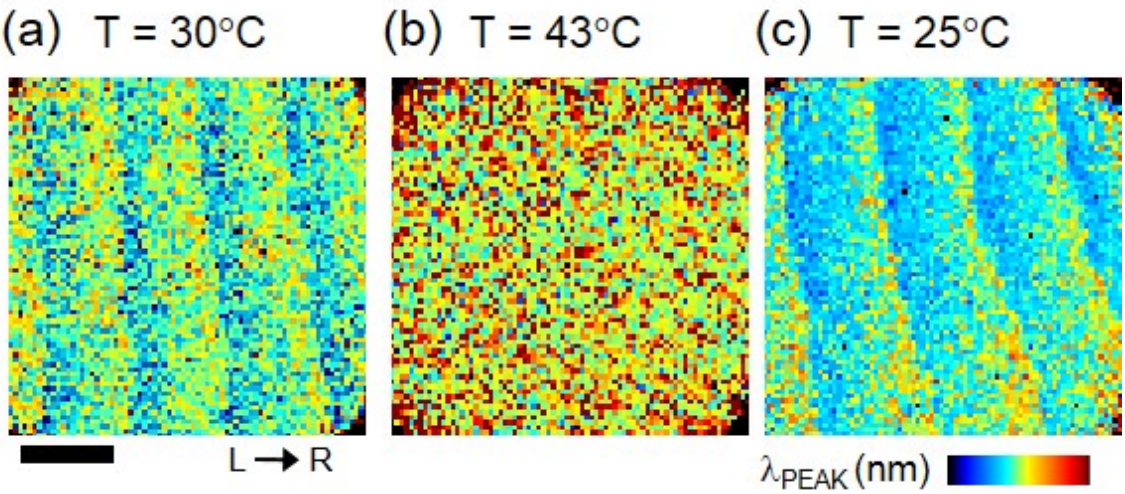

Figure 11: Spatially resolved PL scans of QD-CLC mixture at (a) 35ºC, (b) heated to 43ºC, and (c) cooled back to 25ºC, mapping the emission λ_{PEAK}. L denotes the left edge of a Grandjean step where the pitch is at the minimum value within the step and R denotes the right where the pitch is at the maximum.

To understand this pattern formation, we make a spectral comparison of the CLC stop band and the QD emission in Fig. 3 in three samples prepared with different ratios of 5CB to COC to tune the pitch. Fig. 12(a) shows spectra for a sample prepared with 44 wt% 5CB to COC and a pitch of approximately 620 nm. Here, the peak emission of the QDs dispersed in the isotropic phase (circle) overlaps with the short wavelength side of the CLC stop band (square), and the first observations we make are an overall red shift of the QD emission (triangle) and an increase in intensity when the sample is cooled into the cholesteric phase. A detailed analysis of the data reveals a more complicated behavior. It has been predicted that, due to the inherent dichroism, even in the isotropic phase a cholesteric system can modify optical transmission through it. [60] We notice the effects of such modifications in the following two ways: (a) although the QD emission in solution occurs at 608 nm, in the isotropic phase the emission has blue shifted and (b) the peak is not a Gaussian distribution but has a more asymmetric shape. To understand the latter, we perform a multipeak fit analysis using a standard nonlinear Levenberg-Marquardt algorithm where the peak positions and peak widths remain constant and only the relative amplitudes of the peaks are allowed to vary when fitting data from the same sample under different conditions. We find that both emissions (in the isotropic and CLC phases) are best explained as a cumulative effect of three subsets of QDs. These three consist of QDs emitting to the far left and completely outside, at the very edge, and completely inside the stop band (supplementary material, Fig. 15). In the isotropic phase the emission is dominated by the subset that lies to the far left of the stop band while PL from those within the band is quenched, accounting for the asymmetric shape. When cooled to the CLC phase,

the spectral weight shifts to the QDs emitting at the edge of the stop band, causing the spectrum to exhibit an overall red shift of 5 nm. The typical error in our fits λ_{PEAK} is $\sim$0.5 nm.

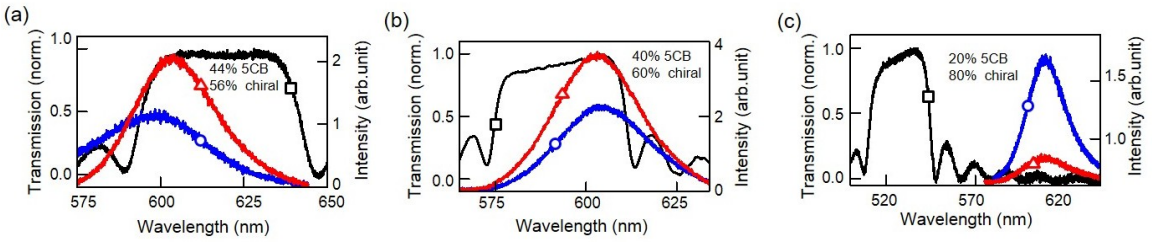

Figure 12: Emission spectra of the QD-CLC mixture in the cholesteric (triangle) and isotropic phases (circle) superimposed on the corresponding stop bands (square) for (a) 44% nematic and 56% chiral LC, (b) 40% nematic and 60% chiral LC, and (c) 20% nematic and 80% chiral LC. Proportions are by weight.

Figure 12(b) plots the emission of the QDs (circle) from an arbitrary spot in the sample shown in Fig. 11 when it is in the isotropic phase. The multipeak protocol executed above is repeated and shows a similar result for this phase, with the emission again being dominated by the QDs that emit outside (but, this time, to the right) of the stop band (supplementary material, Fig. 16). The spectrum though still blue shifted from the solution emission, is not as affected as in the previous sample. As the sample is cooled and the CLC phase forms, we observe that now the QD emission overlaps with the long wavelength edge of the CLC stop band. The QD spectrum from that same spot (triangle) is again predominantly from the QDs emitting at the edge of the stop band and, as a result, blue shifted by 3 nm, with the peak intensity greater than the peak intensity from QDs in the isotropic phase by a factor of 2. Figure 12(c) shows the stop band of a mixture of 20 wt% of 5CB to COC with a pitch of approximately 525 nm. The QD emission spectrum in the isotropic phase (circle) does not overlap with the stop band at all, and we now observe several points. First, the emission in the isotropic phase now occurs exactly at 608 nm, where the QDs emit in solution. Second, the distribution of spectral weight among different subsets of QDs is unchanged between the spectra obtained in the isotropic and the CLC phases (supplementary material, Fig. 17), resulting in no discernible overall spectral shift. And, finally, there is a decrease in the emission intensity of the QDs (triangle) in the CLC phase compared to that in the isotropic solution. From these results shown in Fig. 12, it is clear that the spectral modification of the QD emission is caused by the optical confinement provided by the CLC and that the magnitude of this modification depends on the extent to which the QD and CLC spectra overlap. When there is an overlap [Figs. 12(a) and 12(b)], the QD emission is amplified at the very edges of the stop band, resulting in a small spectral shift as the intensity weight redistributes. But when there is no overlap [Fig. 12(c)] there is no such enhancement. In Fig. 11 the QD emission lies near the long wavelength edge of the CLC stop band, similarly to that shown in Fig. 12(b), and as the stop band shifts toward the red with position from L to R, it continuously amplifies an increasingly redder portion of the QD spectrum, resulting in the observed pattern where the emission red shifts across a Grandjean step. When the pitch abruptly returns to its original value the QD emission pattern repeats itself.

We are effectively utilizing the CLC phase as a one dimensional photonic band-gap material and tuning the emission of the ensemble of QDs by spatially altering the pitch of the CLC medium using the wedge cell. When the cholesteric helix is destroyed by raising the sample temperature above the isotropic phase transition [Fig. 11(b)], without a well-defined pitch to sustain a stop band,

the QD emission randomizes. This stripe formation is thermally reversible and robust. The idea of emission amplification at the long-wavelength edge of the cholesteric reflection band has been employed previously to create a liquid crystal laser. [9, 61] The dyes used in these measurements have been rod-shaped molecules with emission linearly polarized along their long axis. This leads to multiple reflections and amplification of the emission that lies only near the long edge of the stop band. CdSe/ZnS QDs have a more isotropic emission compared to dyes, even when embedded in nematic LC. [34, 62] The fact that the amplification is still observed, and occurs at both ends of the stop band, is surprising and suggestive of a more complicated modulation by the CLC medium than in the case of dyes. [63]

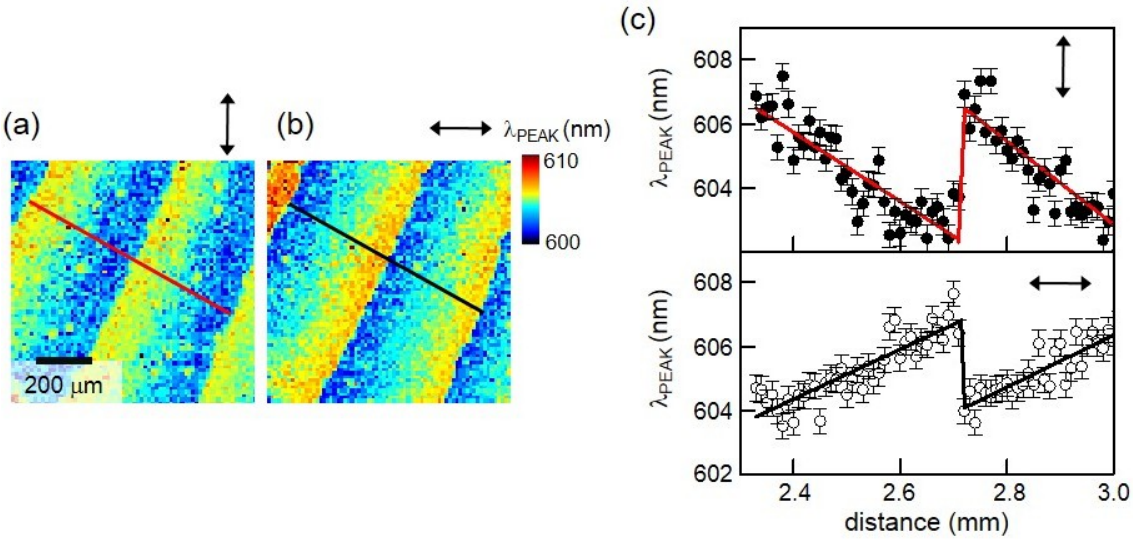

Figure 13: Polarization resolved PL maps of λ_{PEAK} when observed (a) perpendicular (90º) and (b) parallel (0º) to the rubbing direction. (c) Plot of λ_{PEAK} for (a) and (b) along the lines shown on the maps. λ_{PEAK} of (a) are plotted as solid circles (top) and (b) as open circles (bottom). Lines are linear fits to data.

To investigate the transmission of QD emission through the cholesteric phase in detail we have carried out further work to characterize the emission polarization of the QD-CLC sample. Figures 13(a) and 13(b) are spatially resolved PL maps showing the λ_{PEAK} variations over the same region of the sample but observed through a linear polarizer aligned vertically and horizontally, respectively. The horizontal direction, denoted $\vartheta = 0º$ in our setup, is parallel to the rubbing direction of the Cano-wedge cells. Again, as before, a wavelength gradient is observed similar to that in Fig. 11. However, while Fig. 13(a) shows the gradient moving from longer to shorter wavelengths across the step, in Fig. 13(b) the gradient is reversed. In Fig. 13(c) we have plotted data along the lines indicated in Figs. 13(a) and 13(b), where we see the sawtooth pattern of the QD peak emission, and that the horizontally ($\vartheta = 0º$) and vertically ($\vartheta = 90º$) polarized components are essentially reversed. The corresponding spectrally integrated intensity maps display neither stripes nor any clear difference between the two polarization configurations, although it is interesting to note that the data collected without polarization optics in Figs. 11(a) and 11(c) resembles the pattern in Fig. 13(b), implying the emission intensity along that 0º is slightly larger than that observed along 90º. We attribute this to the fact that 0º is aligned along the rubbing direction which defines the director of the nematic component (5CB) in the CLC composite. Emission intensity is typically greater along that direction

due to reduced scattering irrespective of any other effect (supplementary material, Fig. 184).

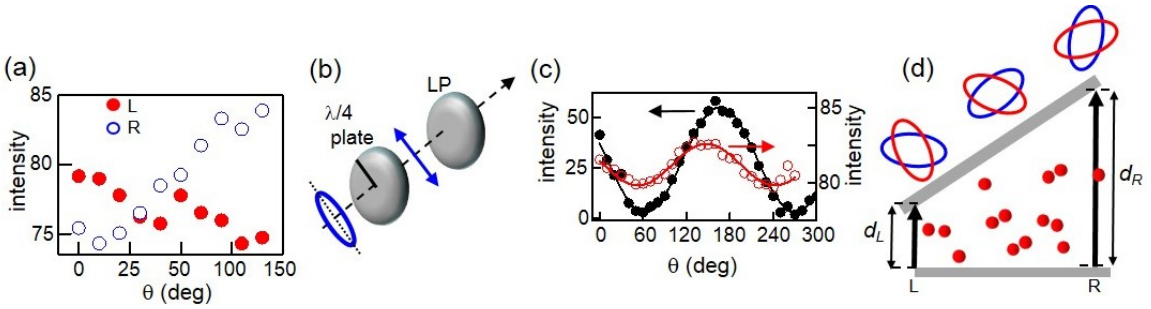

Figure 14: (a) PL emission varying with the angle with respect to the rubbing direction, ϑ, at the two edges (L and R) of one step. (b) Schematic of optical path used to analyze emission polarization using a combination of a quarter wave ($\lambda/4$) plate and a linear polarizer (LP). (c) Polarization resolved PL intensity as a function of angle ϑ between the rubbing direction and the LP with (solid circles) and without (open circles) the $\lambda/4$ plate. (d) Schematic depicting the QD emission polarization states changing across the Grandjean steps with increasing path difference d.

To investigate the polarization dependence further, we track the spectrally discrete peak intensities of QD emission for two spots at the beginning and end of a Grandjean step, as a function of ϑ, shown in Fig. 14(a). Here we observed that the peak intensity at the beginning of a step (marked "L") is highest when the polarizer is aligned along the rubbing direction and decreases with increasing ϑ. At the same time, the intensity at the end of the edge (marked "R") is initially small but increases with ϑ. Together with the differences between Figs. 13(a) and 13(b), these results suggest that as the emission from the left edge of a step red-shifts between the 0º and 90º directions, the intensity simultaneously decreases. The exact reverse occurs at the right edge. These variations are small (on the order of 6–10%) but systematic. To confirm the effect, a more detailed measurement of QD PL intensity from an arbitrary region is carried out. Shown in Fig. 14(c) (open circles) we see that although the emission intensity exhibits a sinusoidal variation with ϑ, the signal does not fall to zero at any angular position of the linear polarizer. This is a surprising result because it is generally assumed that the emission from a cholesteric device should be circularly polarized following the helicity of the CLC. [64] Our results clearly demonstrate that the transmitted PL is not circularly polarized (in which case there should be zero or negligible variation in intensity with ϑ) but is partially linearly polarized, elliptically polarized, or a mixture of the two. To determine which, we insert a $\lambda/4$ plate before the linear polarizer in the collection path [Fig. 14(b)], with the fast axis of the $\lambda/4$ plate aligned along the direction of maximum transmission, which in our case is 145º [Fig. 14(c), open circles]. Then we rotate the linear polarizer again and plot the resulting intensity as a function of ϑ in Fig. 14(c) (solid circles). Now we can clearly observe that the resultant intensity does go to zero, although the maximum occurs at a different angle. This is a definite indication that the emission is elliptically polarized. We can approximate that the ellipse major axis is tilted by 35º to the rubbing direction, where the emission intensity was maximized prior to inserting the $\lambda/4$ plate.

This confirmation of elliptically polarized emission implies the CLC medium is exhibiting circular dichroism in addition to the expected circular birefringence and that it imparts an arbitrary phase to the electromagnetic radiation traveling through it. This phase δ is given by $\delta = (\pi \Delta n/\lambda)d$, where d is the path length through the sample and n is the difference in refractive indices as is typical

of a birefringent material. [65] For elliptically polarized light the tilt of the ellipse is a function of δ, and since δ is dependent of the wavelength λ, it follows that the different parts of the QD PL spectrum will be polarized at slightly different angles to the rubbing direction. This allows us to come up with a simple pictorial representation as shown in Fig. 14(d). At the beginning of a Grandjean step at "L" $d_L = p$, and from the data in Figs. 13(a) and 13(b), this appears to satisfy the condition where the shortest wavelength of the QD emission is polarized with the major axis closer to the horizontal direction with reference to our measurement scheme. The other "colors" form ellipses titled along different angles, ending with the longest wavelength closest to the 90º axis. Moving across the step, d changes until at the end of a step at R $d_R \rightarrow 3p/2$. Using typical values of Δn in CLC materials, [66] this corresponds to a negligible phase difference between points L and R. However, in a confined geometry the reflection-induced multiple passes through the CLC medium enhances the phase difference greatly.A simple approximation for our system gives us an estimate of a photon confinement time $\sim$10−13 s, which translates to about 25 passes. In turn, this implies a total phase difference 25 times bigger than the previously calculated δ, which would lead to a considerable reorientation of the emission ellipses between L to R (as shown by the blue and red ellipses). This explains why we observe the complimentary spectral maps when viewed along 0º and 90º.

6.4 Conclusions

We have demonstrated the fabrication of a QD embedded one-dimensional photonic cavity constructed from a cholesteric liquid crystal. The liquid crystal medium selectively enhances the PL from a subset of QDs whose emission spectrally overlaps with the edges of the stop band. The mechanism of such amplification is most likely due to the Purcell effect [67] as preliminary time-resolved data show an increase in the recombination rates in the QD-CLC samples when compared to the recombination rates of the QDs in solution. However, unlike typical photonic band gap materials, such as naturally occurring crystalline solids [68] or those fabricated from semiconducting structures, [69] the stop band of the CLC can be easily tuned by altering the ratio of its components and additionally externally modulated using temperature or electric fields. This greatly enhances the spectral flexibility of the photonic device. The controllable spatial variation in spectral emission and polarization that is imparted by the CLC medium provides excellent possibilities for increased device functionality,making this liquid crystal matrix a very attractive platform for designing new QD-based optical materials.

6.5 Supplemental Material

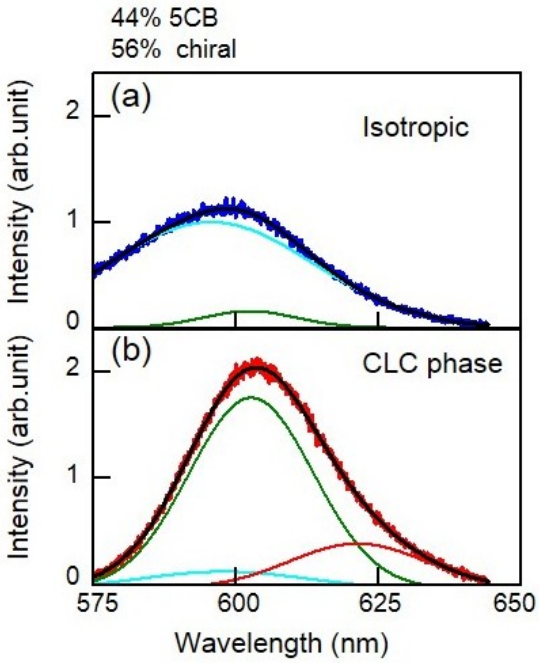

Figure 15: Multi-peak fits to emission spectra in (a) isotropic and (b) CLC phase for 44% nematic and 56% chiral LC mixture. In (a) the shorter wavelength peak has more spectral weight but when the sample is cooled to the CLC phase in (b) the spectral weight shifts to the mid-wavelength subset, and a longer wavelength peak starts to emerge.

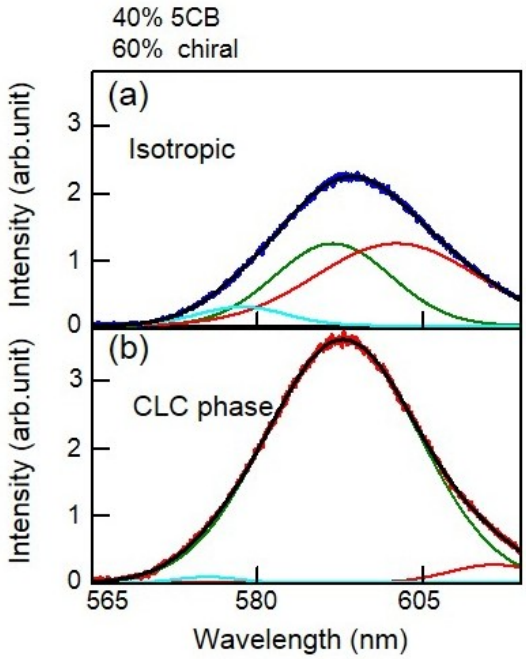

Figure 16: Multi-peak fits to emission spectra in (a) isotropic and (b) CLC phase for 40% nematic and 60% chiral LC mixture. In (a) the long and mid-wavelength peaks have more spectral weight but when the sample is cooled to the CLC phase in (b) the spectral weight shifts is concentrated in the mid-wavelength subset, while emission from both the long and short wavelength subsets is suppressed.

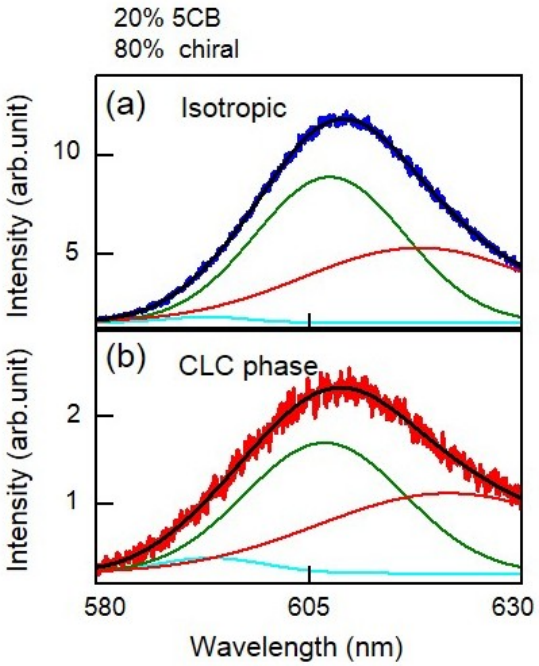

Figure 17: Multi-peak fits to emission spectra in (a) isotropic and (b) CLC phase for 20% nematic and 80% chiral LC mixture. In both phases, the spectral distribution is the same.

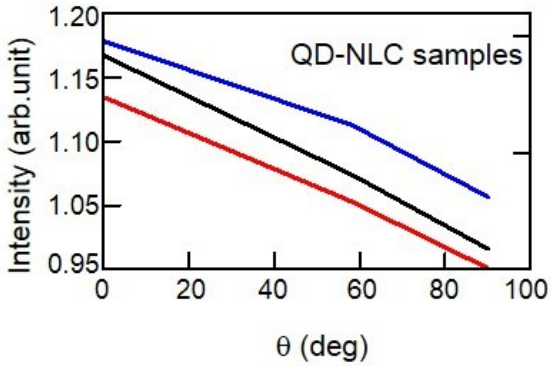

Figure 18: Peak emission intensity for CdSe/ZnS QDs in 100% nematic LC as a function of relative angle ϑ between the rubbing direction (aligned to 0º) and a linear polarizer in the collection path, shown for three different samples. Emission along the rubbing direction is consistently higher in all three and falls off by 10-15% as ϑ increases from 0 to 90º. As the proportion of nematic LC is reduced in the CLC samples, this effect decreases but is still present as seen from the similarities between figs. 11(a) and 13(b).

7 Dynamics of spontaneous emission of quantum dots in a one-dimensional cholesteric liquid crystal photonic cavity

We have established that the cholesteric liquid crystal can modify the peak emission and modulate the polarization of QDs that are embedded within. We now consider the resonance condition created by matching the QD emission to the edge of the CLC's photonic cavity. We show that we are indeed coupling the emission to the cavity and stimulating spontaneous emission of the QDs.

7.1 Introduction

Tailoring basic light-matter interactions for advanced applications is a major focus of researchers in photonics, semiconductor physics and materials science. Advances over the last decade in electron microscopy, sample fabrication and synthesis have presented the means for manipulation and control of these interactions with remarkable precision down to micro and nanoscales. A typical example is the development of optical microresonators, with very high quality (Q) factors, which interact with light confined within their volumes to create lasing. [70] Their size makes them attractive candidates for incorporation in on chip devices that require small footprints and low threshold powers. [71] These devices can be fabricated in a variety of geometries, and one of these is the planar micro-cavity design based on the well-known photonic crystal template. This has the advantage of a very small mode volume, resulting in ultra-high Q emission. [72] Photonic band gap (PBG) cavities fabricated from semiconducting materials can support lasing emission of Q . 105 in the near infrared region.4 In spite of these attractive properties, PBG cavities are very fabrication intensive and cannot be tuned easily *in situ*. An alternative approach to PBG cavities with micron scale active regions was developed in the last decade using liquid crystal (LC) materials. [73, 74, 75] Certain chiral LC molecules self-assemble to form the cholesteric phase, characterized by a helical rotation of the director axis with a characteristic pitch (Fig. 19A, left inset). [8] This helical pitch results in a spectral stop-band (the reflection band) analogous to that seen in photonic crystals, and therefore cholesteric liquid crystal (CLC) materials can act as a fluid one-dimensional photonic cavity. CLCs have the advantage of not only being far easier to fabricate than their semiconducting counterparts, but their stopbands can be spectrally tuned using either temperature or LC composition. Furthermore, the cavity effect can be reversibly switched on and off by an externally applied electric field. Dye doped CLC films exhibit resonant emission at the long wavelength band-edge of the stop-band, which has led to the development of LC-based dye lasers. [76, 77, 9]

In this paper we investigate modulation of the dynamical spectral properties of chemically synthesized quantum dots (QDs) dispersed in CLC photonic cavities. QDs can be more suitable than organic dyes for certain applications, especially given the optical tuneability offered by their size-dependent energy band-gaps and their higher photo-stability compared to most dyes. [78] Furthermore, they are isotropic emitters and therefore are not subject to the polarization constraint that allows efficient amplification only at the long wavelength edge in anisotropic dyes. [79, 61] The study of chemically synthesized QDs dispersed in LC materials is a relatively new research area. While it is expanding rapidly, prior work has been limited to nematic [36] and smectic [80] LC materials, where greater emphasis has been given to the effect of the QDs on the LC electro-optic properties. Most recently, we have demonstrated that in these systems QD emission is enhanced at both edges of the CLC stop-band, accompanied by a spectral red shift at the short wavelength edge of the stop-band and blue shift at the long edge. In addition, the resonant emission is elliptically polarized by the CLC cavity, with the ellipticity being a function of the emission wavelength. [1]

As a result, in a set-up such as a Cano-wedge cell, [81] the polarization phase of the QD emission is both *spatially* and *spectrally* controllable. This last property is especially attractive. It not only opens up new possibilities to use these materials as novel opto-electronic and photonic components, but also has important implications for QD-based quantum information processing schemes where precise modulation of emission frequency and phase is vital.

7.2 Experimental Procedures

7.2.1 Sample Preparation

CLC samples were prepared by mixing cholesteryl oleyl carbonate (COC, Sigma Aldrich) and the nematic liquid crystal, 49-pentyl'4-biphenylcarbonitrile (5CB, Sigma Aldrich) in varying proportions by weight. The LC mixtures were sonicated at 43 ºC (above the isotropic transition temperature for both compounds) for 1 h to ensure good mixing. CdSe/ZnS QDs with octadecylamine ligands (NN Labs) and an emission in toluene solution centered at 609 nm, were added to the LC mixtures at a concentration of 0.01–0.02 wt%, then sonicated again for 1–6 h to obtain the final QD–LC composite.

LC films were deposited between glass plates using two different alignment layers, planar (molecules lie parallel to the glass substrate) and homeotropic (molecules lie perpendicular to the substrate). To prepare a planar alignment coating, glass slides were spin coated with a 1 wt% aqueous polyvinyl alcohol (PVA) solution (Sigma Aldrich), dried in air and rubbed to establish the required orientation. To prepare a homeotropic alignment layer, glass slides were dip coated for 5 min in 0.5 mM aqueous hexadecyltrimethylammonium bromide (CTAB, Sigma Aldrich) solution. The isotropic liquid crystal mixture (at 40.0 ºC) was then pipetted onto the prepared glass slides, arranged to form a Cano-wedge cell and then cooled at 0.1 ºC min^{-1} to 30 ºC to form the CLC phase using a Linkam LTS350 hot-stage. Several different formulations were used in this study. Sample S1 contains 0.02 wt% QDs, dispersed in 59.6 wt% COC and 40.4 wt% 5CB. Samples S2, S3 and S4 contain 0.01 wt% QDs, dispersed in 59.4 wt% COC and 40.6 wt% 5CB. Sample S5 contains 0.01 wt% QDs dispersed in 59.1 wt% COC and 40.9 wt% 5CB. The control sample contains 0.01 wt% QDs dispersed in 74.8 wt% COC and 28.2 wt% 5CB. The purpose of varying the proportion of different LC compounds in the mix is to change the spectral position of the stop-band. After cooling into the CLC phase, all samples were allowed to anneal for the same time prior to beginning measurements.

7.2.2 Measurement Techniques

We verify the formation of the CLC phase in our samples using Polarized Optical Microscopy (POM). Fig. 19A (right inset) shows a transmission image of a QD–LC sample with planar alignment. The LC molecules are forced to align parallel to the glass slides, as shown in the schematic representation in Fig. 19A (left inset), but the increasing distance between the two slides forces the pitch to continuously elongate, which changes the spectral position of the stop-band and, hence, the colour of the CLC transmission. Once the distance between the glass plates is large enough to fit in another half-pitch, the colour gradient repeats itself, a pattern known as Grandjean steps. The stopband of an arbitrary region of this sample is plotted in Fig. 19A, measured using a UV-Vis spectrophotometer. Fig. 19B shows the corresponding results for a homeotropicaly aligned sample. The helices are now randomly oriented in a focal conic texture (Fig. 19B, left inset) and the transmission image in Fig. 19B (right inset) does not show the Grandjean steps. Initially after preparation, the

homeotropic samples appear white in colour, implying wavelength independent scattering. However, as these samples anneal, a characteristic length scale forms and, as a result, the reflectivity (Fig. 19B, main) shows a much weaker, broad peak instead of a well-defined stop-band.

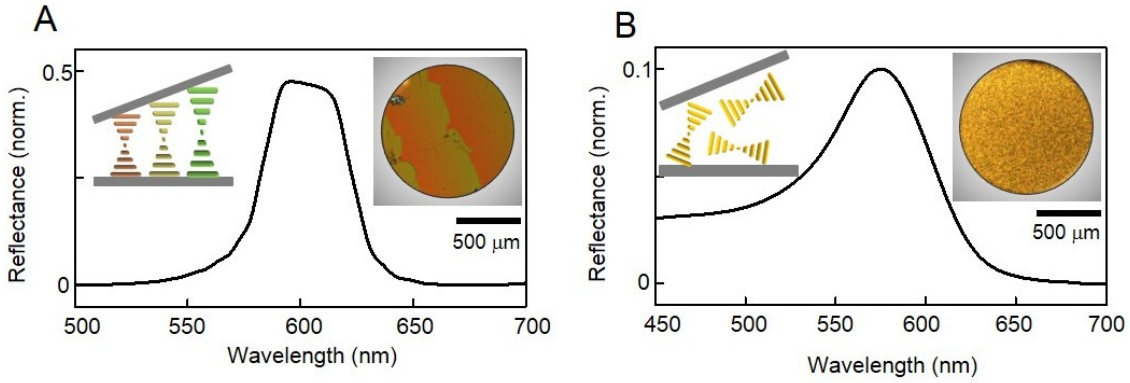

Figure 19: (A) Reflectance showing a well-defined stop-band in a CLC sample with planar alignment. A schematic representation (left inset) demonstrates the helical arrangement of the CLC in a Cano-wedge cell. The changing pitch creates the stripe pattern observed under POM (right inset). (B) Reflectance of a CLC sample with homeotropic alignment. A schematic representation (left inset) depicts the random orientation of helices, which results in a homogenous transmission (right inset).

Further spectral characterization is done using a custom designed scanning photoluminescence (PL) confocal microscopy system. The excitation source used is a 532 nm continuous wave laser focused on the sample through a high NA objective to produce a diffraction-limited spot size (~600 nm). The samples are mounted on a heat controlled motorized 3D scanning stage with lateral resolution of 40 nm. The PL from the QDs is collected by the same objective and dispersed by an Acton 300i spectrometer onto a thermoelectrically cooled CCD (spectral resolution ~0.18 nm). Using this arrangement, we raster scan selected regions of the sample to create spatially resolved PL maps. For the time-resolved measurements we use an ultrafast Ti:Sapphire laser with 76 MHz repetition rate and pulse width of 150 fs as our excitation source. The laser output frequency is doubled to produce an excitation wavelength of 400 nm with the final power reduced to 7 mW. The spectrometer is coupled to a single photon avalanche detector with a time-correlated single photon counting system (PicoHarp 300) with an instrument response function of 12 ps.

7.3 Results and Discussions

In Fig. 20 we show the spatially-resolved maps of the peak QD emission wavelength (λ_{PEAK}) for sample S1. Fig. 20A and B correspond to the planar aligned sample when the emission is polarization-resolved at 0º and 90º to the rubbing direction (black arrow) from the same region. The dotted line in Fig. 20A highlights the QD emission red-shifting across a Grandjean step. It has been recently shown17 that this effect results from a coupling between QD emission and the cholesteric stop-band. When viewed from an orthogonal polarization, the λ_{PEAK} blueshifts across the same step in Fig. 20B. This complimentary pattern can be explained by the elliptical polarization of the QD cavity coupled emission. [1, 82] The ellipticity is both wavelength and position-dependent and is therefore dominated by the short (long) emission wavelength in the case of parallel (perpendicular)

polarization set up at the start of each step. Fig. 20C and D are similar PL scans of the same area in a QD–LC sample with homeotropic alignment, taken along one spatial axis (which we designate 0º) and then along another after a 90º sample rotation. As expected, without the presence of a well-defined stop-band and resulting Grandjean steps, the QD emission is uniform and polarization-independent.

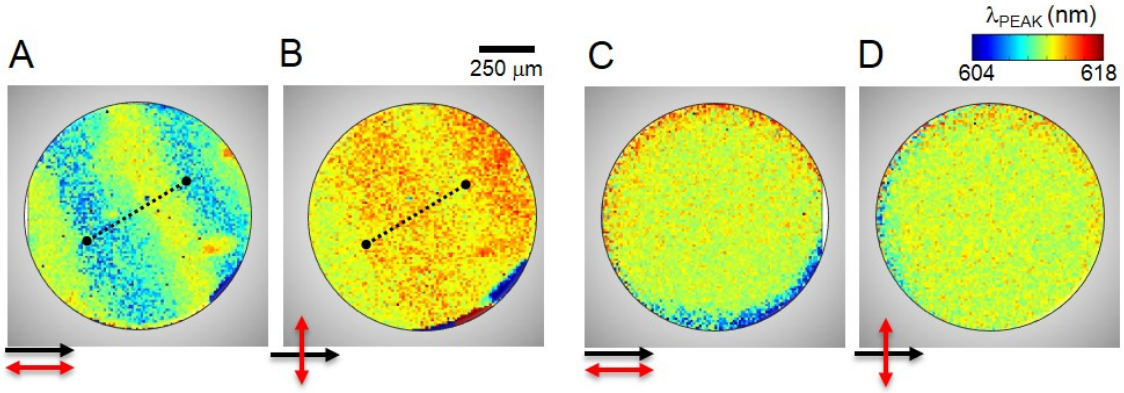

Figure 20: Scanning PL images of the QD–CLC sample S1. Spatially resolved QD peak emission wavelength is plotted for a planar alignment with collection polarization direction (A) parallel and (B) perpendicular to the rubbing direction. The images show a complementary color change across a step along the dotted lines. Similar scans for homeotropic alignment with (C) parallel and (D) perpendicular polarization configurations showing homogenous and polarization-independent QD emission.

Spectral modulations of QD emission, as observed in Fig. 20, are often accompanied by changes in the recombination rate. When suspended in solution, chemically-synthesized QDs have a recombination process described by an exponential decay with a single time-scale $I(t) = A\exp(-t/\tau_s)$ and the recombination rate, which is wavelength independent, is given by $K_s = 1/\tau_s$. For the QDs used in our samples, the recombination lifetime (in solution) was τ_s ~13 ns.20

We begin our investigation of QD recombination lifetimes in the CLC photonic cavity with a control sample where the CLC stop-band does not overlap with the QD emission spectrum. Fig. 21A (inset) shows the QD emission spectrum at 43 ºC when the CLC is in the isotropic phase. The arrows indicate the points along the spectrum where time-resolved data is presented in the main part of Fig. 21A. The normalized curves for 590, 610 and 630 nm show that the recombination lifetime is now wavelength dependent and increases monotonically with the emission wavelength (inset, solid circles). This variation is most likely not a result of dispersion in the CLC, as it is typically observed in any ensemble where the QDs are not isolated, but have dipole– dipole inter-particle interactions that allow non-radiative energy transfer from the smaller QDs to the larger ones. This energy transfer introduces an additional relaxation channel for the smaller QDs, increasing their total recombination rate. [83] We can estimate the efficiency of this energy transfer as $\varepsilon = 1 - (\tau_\lambda/\tau_s)$ where τ_λ is the recombination lifetime in the CLC sample at a particular wavelength and τ_s is the lifetime in solution. [84] This gives us an ε of 62% at 590 nm, which decreases to 38% at 610 nm and by 630 nm is a very small 6%. In comparison, a close packed film of these QDs would have almost 90% efficiency at the lowest wavelengths. [85] Since dipole–dipole interactions fall off as ~$1/r^3$, the comparative smaller e values in the QD–CLC samples are not surprising. Fig. 21B shows

spectra and recombination lifetimes when the control sample is cooled to 25 ºC. The CLC has a distinct stop-band that has no overlap with the QD spectrum. As a result, the recombination process is relatively unperturbed and follows a single exponential decay. Across the spectral range of the emission curve, the lifetime τ varies from 4–11 ns (solid circles), similar to that observed in the isotropic phase.

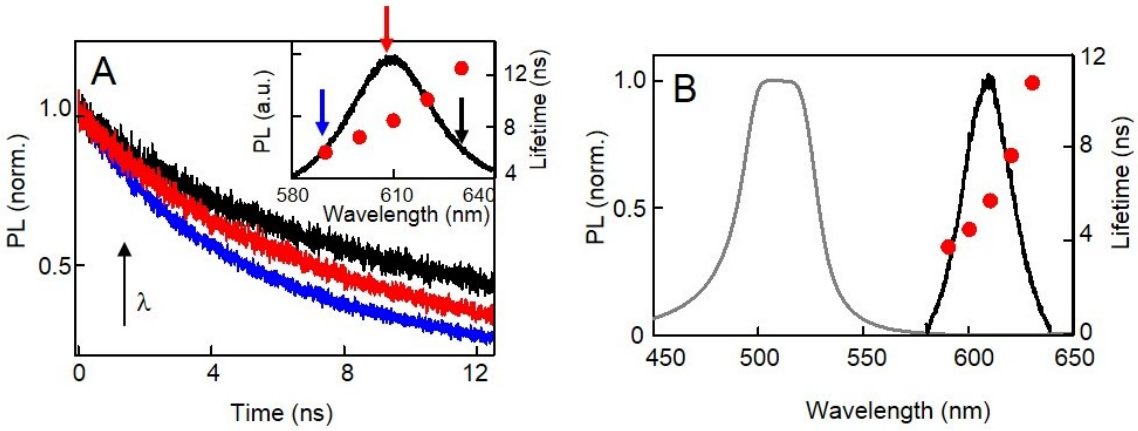

Figure 21: (A) Spectrally resolved, time-resolved PL taken at three points along the QD emission spectrum (indicated by arrows in the inset) for the control sample at 43 ºC. Recombination times obtained from exponential fits are plotted in the inset and show the QD lifetime increasing with wavelength as a consequence of inter-QD resonant energy transfer. (B) The CLC stop-band and QD emission spectrum for the control sample at 25 ºC. QD recombination decay shows one characteristic lifetime (solid circles).

As in the case of the dipole–dipole coupling between QDs, coupling between the photon of an emitter and the resonance mode of the cavity it is embedded in also causes faster decay of spontaneous emission, a phenomenon known as the Purcell effect. [86, 87, 88] Given that QD emission is amplified in the cholesteric phase due to photonic confinement, it is possible that recombination dynamics would be modulated as well. In Fig. 22A we plot the CLC stop-band and the QD emission spectra for sample S2, and superimposed on these are the recombination lifetimes extracted from the corresponding spectrally resolved, time-resolved PL curves. In the spectral region where the normalized QD emission has 50% or more overlap with the stopband, the QD PL has two characteristic lifetimes. The longer of the two, τ_1 (circles), is consistently shorter than the single recombination lifetime observed in the control sample, although it increases with emission wavelength as well. Furthermore, it is now accompanied by a faster lifetime, τ_2 (squares), less than 2 ns. The recombination process can now be described by the function, $I(t) = A_1 \exp(-t/\tau_1) + A_2 \exp(-t/\tau_2)$, with a total recombination rate equal to $K = 1/\tau_1 + 1/\tau_2$. We note that the spectral region outside the stop-band still has a single decay rate. Fig. 22B shows the time-resolved data from the two extremes of the emission spectra, at 590 nm and 640 nm, on a semi-log scale. The recombination curve at 590 nm clearly has two distinct slopes, signifying the two lifetimes, while the curve at 640 nm has a single lifetime. Fig. 22C and D show similar data from sample S4, and we again observe two recombination lifetimes in the spectral region where there is partial overlap between the stopband and QD emission spectra.

To correlate the lifetime changes to cavity effects further, we examine samples where the CLC cavity modes and alignment are different from those studied above. Fig.22E shows the results

from sample S3, where the QD emission spectrum lies entirely within the stop-band. In this case, there is suppression of the entire QD emission by the photonic cavity indicating no QD– cavity coupling. The time-resolved data is now characterized by a single exponential decay over the entire QD emission spectral range, as seen in Fig. 22F. Furthermore, the decay times in these QDs are consistently longer than the long lifetime t1 in the other two samples, where the cavity modulates the QD emission. In this sample, at the longest emission wavelength, the recombination time is almost equal to the average isolated QD lifetime observed in solution and similar to that observed in the control sample (Fig. 21B). In Fig. 23 we compare results from the planar and homeotropic versions of sample S5. The planar sample has a well-defined stop-band where the long edge overlaps with the QD spectrum. As a result, we observe the stripe pattern in the spatially-resolved PL map (Fig. 23B) signifying the expected QD spectral modulation, as well as a second decay time in the wavelength range that lies within the stop-band (Fig. 23A, solid circles). In comparison, the homeotropic sample does not exhibit a clear reflection band and shows a broad peak much lower in absolute intensity (Fig. 23C). While that peak does overlap with the QD emission, it does not result in either the stripe formation (Fig. 23D) in λ_{PEAK} or in introducing a second recombination pathway. As expected, the time-resolved data shows a single lifetime similar to Fig. 21B.

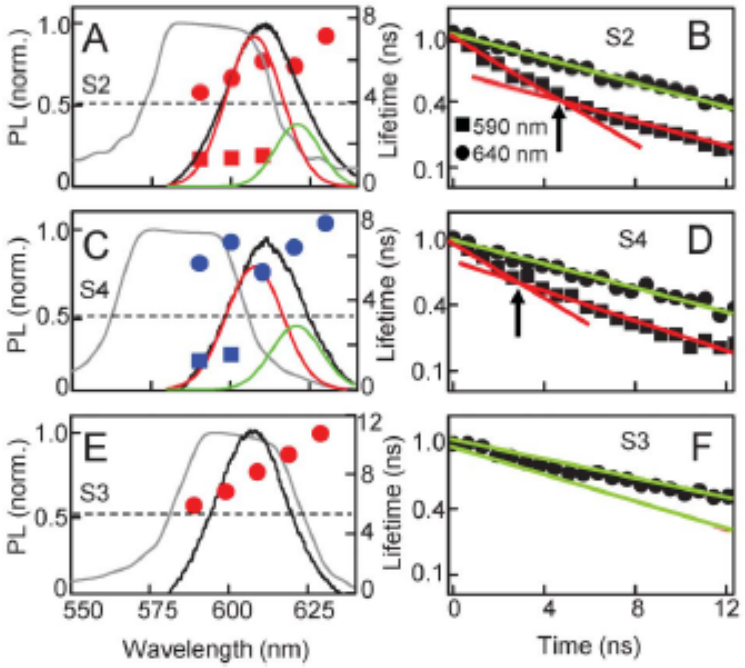

Figure 22: Recombination times for QD–CLC samples S2, S4 and S3, (planar alignment) superimposed on QD emission spectra and the CLC stop-bands. (A, C) QD emission in samples S2 and S4 have partial overlap with the CLC stop-band and can be resolved into two curves. Time-resolved QD PL demonstrates two characteristic lifetimes (solid circles and squares) for the wavelength range that has substantial spectral overlap with the stop-band. (B, D) The corresponding time-resolved data at 590 and 640 nm plotted on a semi-log scale. Linear fits show the presence of two lifetimes at 590 nm and one lifetime at 640 nm. (E) Sample S3, where the QD emission has complete overlap with the stopband and exhibits a single recombination time (solid circles) across all wavelengths. (F) The corresponding time-resolved data at 590 and 640 nm.

The data shown in Fig. 22E–F and 23A–B lead us to conclude that the alteration of recombination dynamics is not solely due to the emission suppression inside the stop-band, nor due to the presence of the CLC medium. The second, faster lifetime observed in Fig. 22A–D appears only in samples where two conditions are simultaneously satisfied. First, the CLC forms a photonic cavity with a well-defined spectral stop-band, and second, the QD spectrum has partial overlap with the stop-band to allow band-edge amplification. Analysis of the QD emission in Fig. 22A and C show that, while the QD spectra in the isotropic phase can be fitted by a single curve, each spectrum in the CLC phase is actually a superposition of two emission spectra. These fits, shown in Fig. 22A and C, suggest these are the contributions from two subsets of QDs, ones that emit inside and ones outside the stop-band. Emission from the former subset is amplified and these constitute the 'resonant' modes that dominate the total emission. The other subset is the collection of the 'non-resonant' modes. The cavity coupling enhances the spontaneous recombination rate, associated with the Purcell effect, only in the QDs that emit in the resonant modes, while the non-resonant modes are left unaltered.

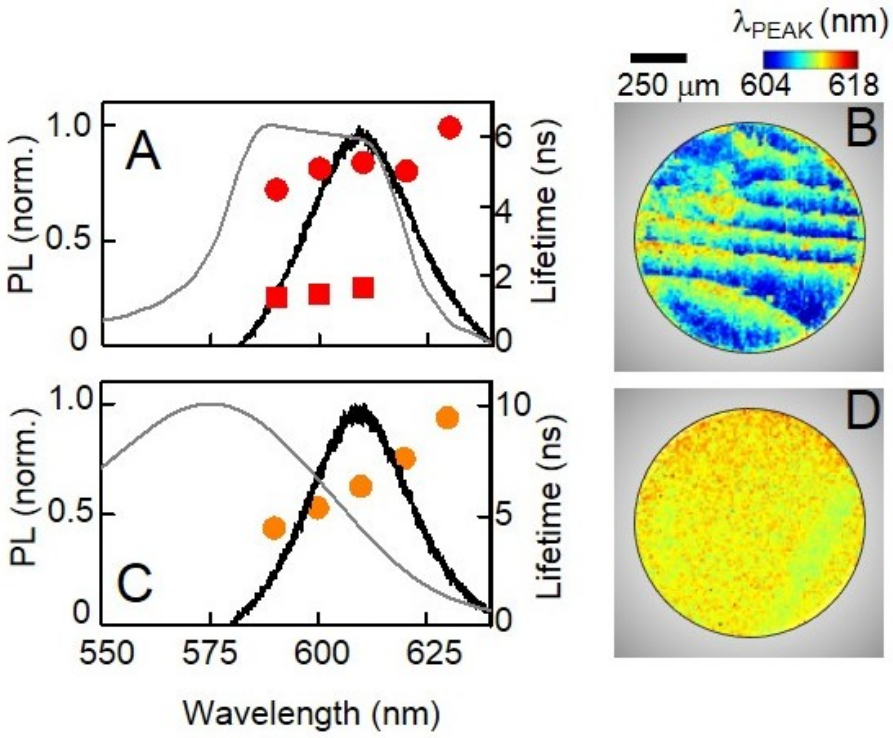

Figure 23: A comparison of recombination times in sample S5 with (A) planar and (C) homeotropic alignment. The corresponding spatially resolved PL maps of peak emission wavelengths are shown in (B) and (D).

7.4 Conclusions

Photonic cavities based on LC materials are attractive because their optical characteristics are easily tunable. For example, the spectral position of the stop-band can be altered by varying the proportion of different LC compounds in the mix, or the cavity effects can be switched on-off using temperature to change the LC phase or electric fields to disrupt the cholesteric texture. These properties have

been exploited to design LC-based dye lasers. Unlike these dyes, QDs are quantum systems that possess unique functionalities that allow them to function as ideal qubits in quantum information processing devices. The ability to control QD properties is therefore an important capability, and we have shown that these CLC cavities can control both the phase and the peak emission wavelengths of an ensemble of embedded QDs. In addition, here we have demonstrated dynamical modulation of QD spontaneous emission by the CLC photonic cavities, with Purcell factors between 3.8–4.2 for our samples (see Table 1), when expressed as the ratios of recombination times with and without cavity coupling. This rate increase is spectrally selective, as it is only observed for the subset of QDs that emit resonantly with the stop-band. This dynamic control can lead to the development of QD-based opto-electronic devices, such as single photon sources. Given the additional functionalities that the liquid crystal matrices can provide, the systems we have investigated can form the basis of other new applications, such as faster, interactive displays, and tunable and flexible components for 4th generation photovoltaics.

Sample	QD (% by wt.)	Composition (COC/5CB % by wt.)	Purcell factor
S1	0.02	59.6/40.4	3.9
S2	0.01	59.4/40.6	4.2
S3	0.01	59.4/40.6	none
S4	0.01	59.4/40.6	4.0
S5	0.01	59.1/40.9	3.8
Control	0.01	74.8/28.2	N.A.

Table 1: Calculated Purcell factors for samples

8 Quantum dot/liquid crystal composite materials: self-assembly driven by liquid crystal phase transition templating

Now instead of modifying the optical properties of the QDs we will use the phase transition of a nematic LC to create ordered clusters of QDs from an initially well dispersed solution. Because a QD forces the ordered LC molecules to undergo elastic deformation, the LC prefers to exclude QDs from well ordered domains. When the phase transition is controlled this forces the QDs into tight packed clusters where the interparticle spacing is such that the ligands of the QDs interdigitate. We find that the clusters have consistent interparticle spacing throughout the cluster and are not packed more tightly in the center.

8.1 Introduction

Ensembles of nanoparticles (NPs) demonstrate collective behaviors that are fascinating variations on their bulk and single particle properties. These include novel electronic, magnetic and photonic effects [89, 90] originating from inter-particle interactions, such as plasmonic resonances in metallic NP arrays, [91] superparamagnetism in assembled magnetic NPs [92] and Forster resonance energy transfer (FRET) between semiconductor NPs such as Quantum dots (QDs). [83] Controlling the assembly of interacting nanoparticles (NPs) is therefore an important goal in materials science as we aim to develop organized and close-packed two and three-dimensional NP superlattices to form metamaterials. Among all the NPs, QDs are particularly interesting for new metamaterials as these have unique size-tuneable properties arising from quantum confinement. Semiconducting particles are currently used in a wide variety of applications, including opto-electronic devices, [93] bio-chemical sensors, [94] photovoltaics, and as labels for biological microscopy. [95] This enhances the attractiveness of designing new multifunctional QD based materials.

The assembly of QDs (or any NPs) into clusters with a uniform packing density has been previously demonstrated in two and three dimensions using solution-based approaches, [96, 97] but these methods produce static arrays that are not amenable to any kind of *in situ* manipulation. Creating macroscopic ordered assemblies of QDs with actively tunable properties is a challenging problem that we can address by leveraging the spatial and orientational flexibility offered by a liquid crystalline template. In this paper, we report a novel method to control the assembly of CdSe/ZnS core/shell QDs into both (1) uniformly packed assemblies of both spatially separated clusters and (2) interconnected web-like patterns using a templating method based on the isotropic to nematic liquid crystal phase transition. The structural and spectral features of the cluster assemblies are fully characterized, revealing a well-defined particle separation with corresponding distinctive FRET and PL lifetime characteristics.

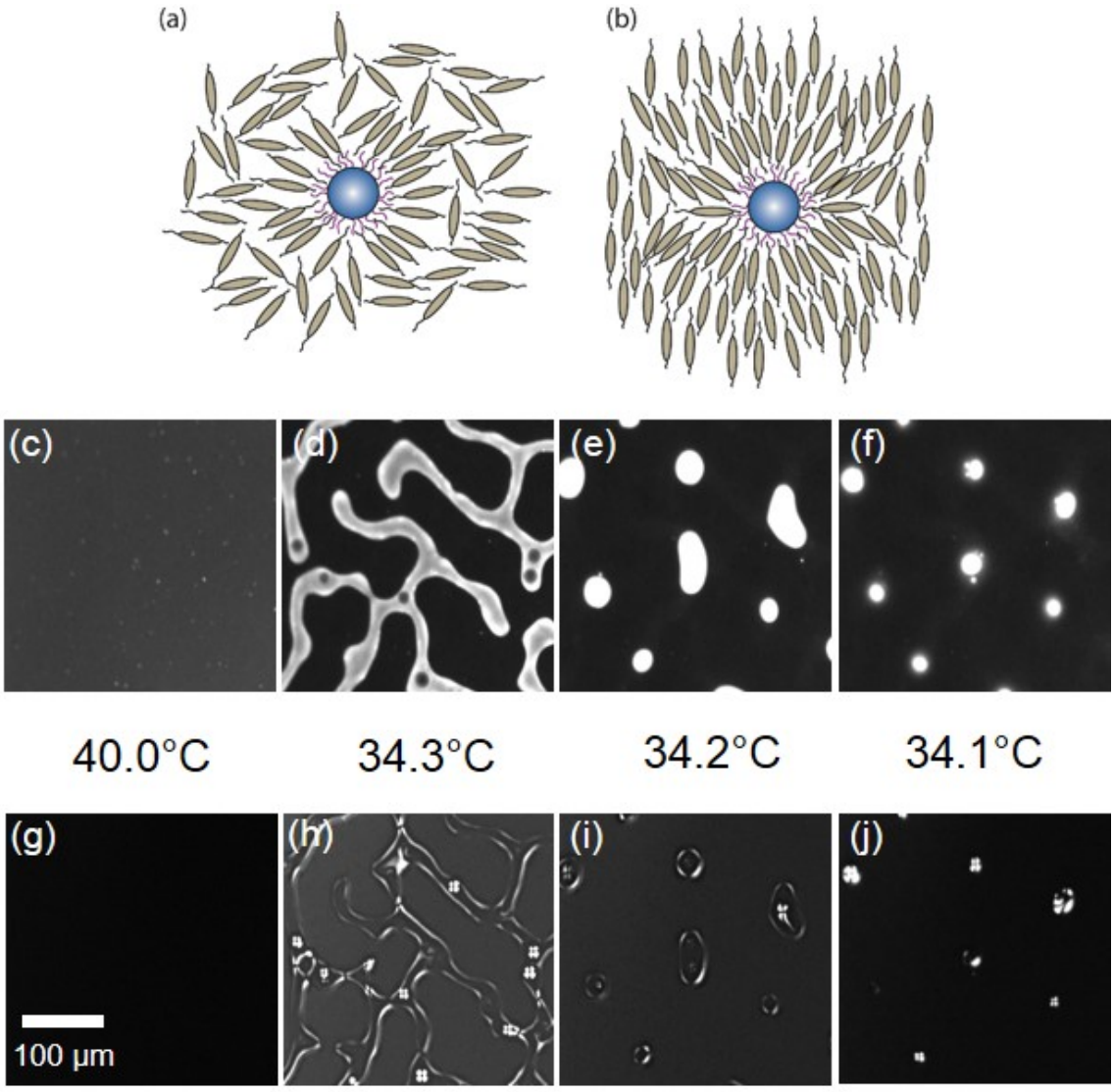

Figure 24: Schematics of a QD in the (a) isotropic and (b) nematic phase, (c–f) fluorescence microscopy images of QD ensemble emission and (g–j) polarized microscopy images of the liquid crystal texture throughout the transition from isotropic (40 ºC) into the nematic phase (34.1 ºC).

Thermotropic liquid crystals exhibit different thermodynamic phases between the isotropic liquid and the solid crystalline phase as a function of temperature. The most well known LC mesophase is the nematic phase, where anisotropically shaped molecules exhibit short-range orientational order, defined by a local vector (the director). Surface functionalized NPs can be designed to disperse or assemble in different liquid crystal solvents. This behavior is critically dependent on the interaction between the NP surface ligands, the molecular details of the LC material and the LC phase. In an LC, it is not enough just to consider solvent properties of the individual molecules, we must also look at the effect of including a particle on liquid crystalline order. Fig. 24 demonstrates this idea. In an isotropic liquid phase, the rod-like LC molecules are randomly oriented and a particle with alkyl chain ligands will disperse in this mixture, with the LC molecules close to the particle orienting in a radial arrangement (Fig. 24a). If this same particle is placed into a medium with nematic

order, there will be a competition between the tendency of the LC molecules to orient in a uniform direction as defined by the director and the radial distribution of molecules around the particle. This creates a topological mismatch between the director field at the particle surface and the nematic director far from the particle. The particle often creates a defect of +1 topological charge, [98] known as a radial hedgehog defect (Fig. 24b). There is much literature concerned with topological defects around colloidal particles included in a liquid crystal phase. [39] Most of these studies however, focus on the regime in which the particle is micron scale. Large colloidal particles have been shown to form structures such as linear chains, [41, 99] clusters, [100] arrays of defects [101] and particle stabilized gels [102] when dispersed in liquid crystal. Recently defects around colloidal particles were used to create controlled arrays in a liquid crystal matrix. [103]

There is an elastic energy cost whenever spherical particles are included in a nematic phase. Because of this effect we can expect the nematic phase to be a poorer solvent for our QDs than the isotropic phase, therefore promoting particle clustering in the nematic phase as a mechanism to minimize the free energy of the system. While there have also been some recent studies on liquid crystal–NP mixtures, these have generally been more focused on the effects of the dispersed NPs on the optical and electrical properties of the host LC phase. [36, 104, 105, 106] Some of this has looked at NP assembly in the defects of discotic [107] and nematic LCs. [108, 109, 110] Recently our group has reported progress in QD dispersion in LC using GaAs and CdSe QDs, including their effects on the optical properties of cholesteric and nematic LCs. [48, 34, 1, 2, 111]

In this paper, we take advantage of the solvent properties of a nematic liquid crystal to organize and assemble QDs with octadecylamine surface ligands. At the transition, QDs preferentially localize to the shrinking isotropic phase domains, producing spatial patterns templated by nematic phase nucleation. We observe that after the phase transition is complete, QD clusters, localized at defect points in the LC texture are formed. By combining small angle X-ray diffraction with FRET measurements we are able to perform a more complete structural characterization than previously reported in similar systems and find that the QD clusters are at least 50 mm in diameter with an average inter-dot spacing of 7.6 nm. With the goal of assembling these clusters in an ordered array, we also demonstrate that cluster location can be controlled by the inclusion of additional micron-scale particles in the system, designed to nucleate defect points. These points attract the QD clusters as the system cools, providing a method to organize cluster assembly in a controlled fashion.

8.2 Results and Discussion

For our study CdSe/ZnS core/shell QDs were chosen with octadecylamine surface ligands (NN Labs, core diameter 6.2 nm, absorption peak 600 nm) to promote homeotropic LC ordering at their surface. Fig. 24c–j show sequences of images collected almost simultaneously on the same QD/LC sample using fluorescence imaging and polarized optical microscopy (POM). We begin the experiment with an evenly dispersed distribution of QDs in the isotropic LC phase. On cooling slowly into the nematic phase, correlations between QD distribution and nematic phase formation are evident. The two imaging techniques are complementary; fluorescence reveals QD distribution in the LC medium, whereas POM provides a birefringence image, revealing liquid crystal alignment and orientation, including the location of defects. Fig. 24c–f are fluorescence images that show the distribution of QDs as the system is slowly cooled into the nematic phase. Fig. 24g through j show the corresponding defect texture of the liquid crystal. Notice that at 40 ºC (in the isotropic phase) the QDs are uniformly distributed across the imaged area. The small points of light are assumed to be clusters of QDs in the isotropic phase. On cooling to 34.3 ºC, the isotropic to nematic transition begins and some LC areas nucleate, as seen in Fig. 24h. The corresponding fluorescence image

for this temperature (Fig. 24d) clearly shows that the growing ordered domains expel most of the quantum dots from the nematic areas into nearby domains still in the isotropic phase. As the nematic domains grow and coalesce the QDs are seen to move into the remaining isotropic regions. The final locations of the QDs are in clusters located at defect points in the liquid crystal texture (Fig. 24f and j).

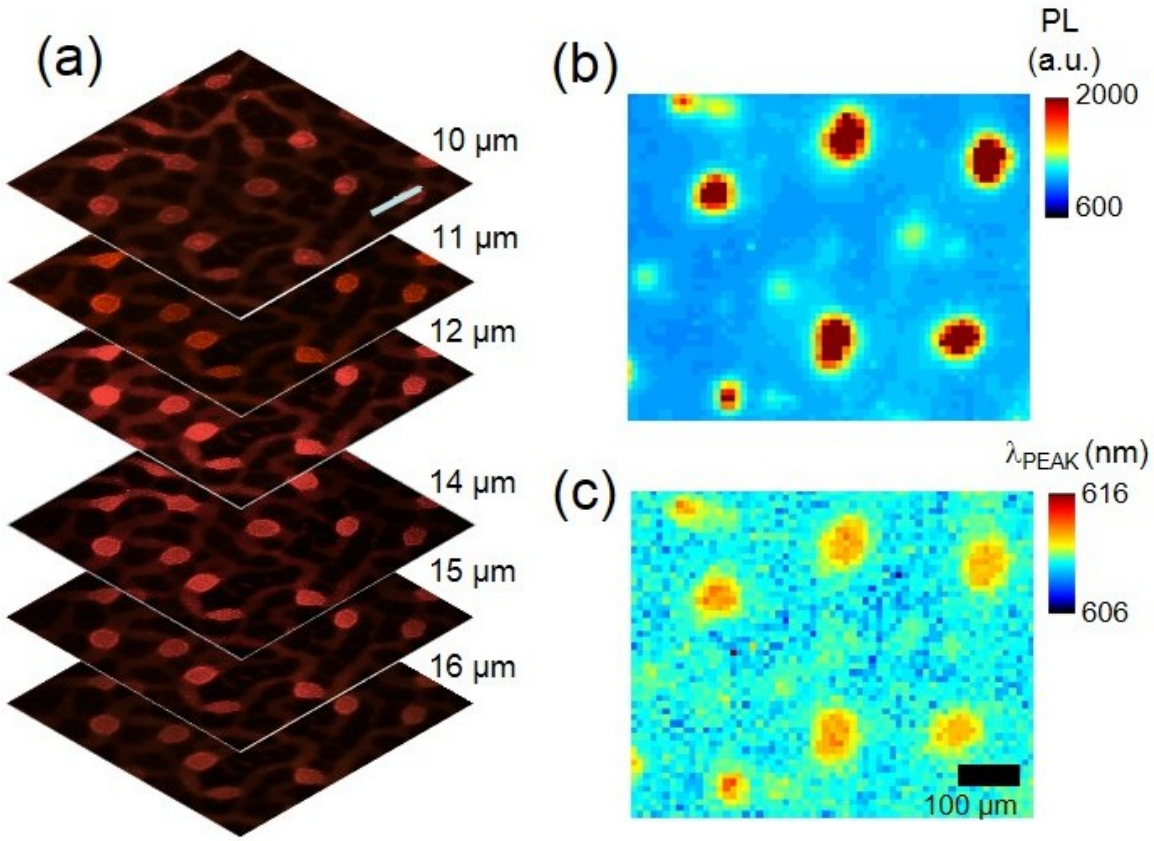

Figure 25: (a) Confocal images of the sample at depths indicated and spatially resolved PL maps of the sample imaged in Fig. 1. Large scale scan showing (b) QD emission intensity and (c) peak emission wavelength. All figures have the same scale bar.

To further characterize QD distribution in an 8 mm thick LC cell we carried out scanning confocal microscopy. Using this technique we can see that the QD clusters are not localized to the center of the cell in a spherical aggregate, but in fact have a more columnar shape, bridging between the glass surfaces. Fig. 25a shows several individual confocal slices taken from a z-stack image of QDs in the LC cell. In these images, we also observe trails of lower-concentration QDs forming a network connecting the bright QD clusters similar to results observed for gold NPs by Milette *et al.* [109] These networks are likely formed during the early stages of phase transition similar to those seen in Fig. 24d. It is not surprising that all the QDs are not able to migrate to the defect points before the nematic phase transition is complete. From the images in Fig. 24 and 25, it is clear that the LC phase transition can be used to spatially organize QDs in the mixture, however optical microscopy alone cannot reveal further detail on QD cluster structure. For a deeper look at QD assembly structure on smaller length-scales, we used two different techniques, scanning pho-

toluminescence (PL) confocal microscopy and small angle X-ray scattering (SAXS). Scanning PL confocal microscopy provides a high resolution image that includes spectral information. Fig. 25b shows a map of the spectrally-integrated peak intensity of the QD emission from the same sample shown in Fig. 24. From Fig. 25b we can note that there is PL emission across the entire imaged area. The clusters of QDs have an intensity ~2.5 times larger than the background, indicating that although there are clusters of QDs present, not all QDs are localized at those points. Fig. 25c shows a map of the corresponding peak wavelength for the sample. Comparing Fig. 25b and c we can see that the QDs assembled in clusters are redshifted by 3 nm compared to those in the background, indicating that they are close enough to exhibit Forster resonance energy transfer (FRET). [112]

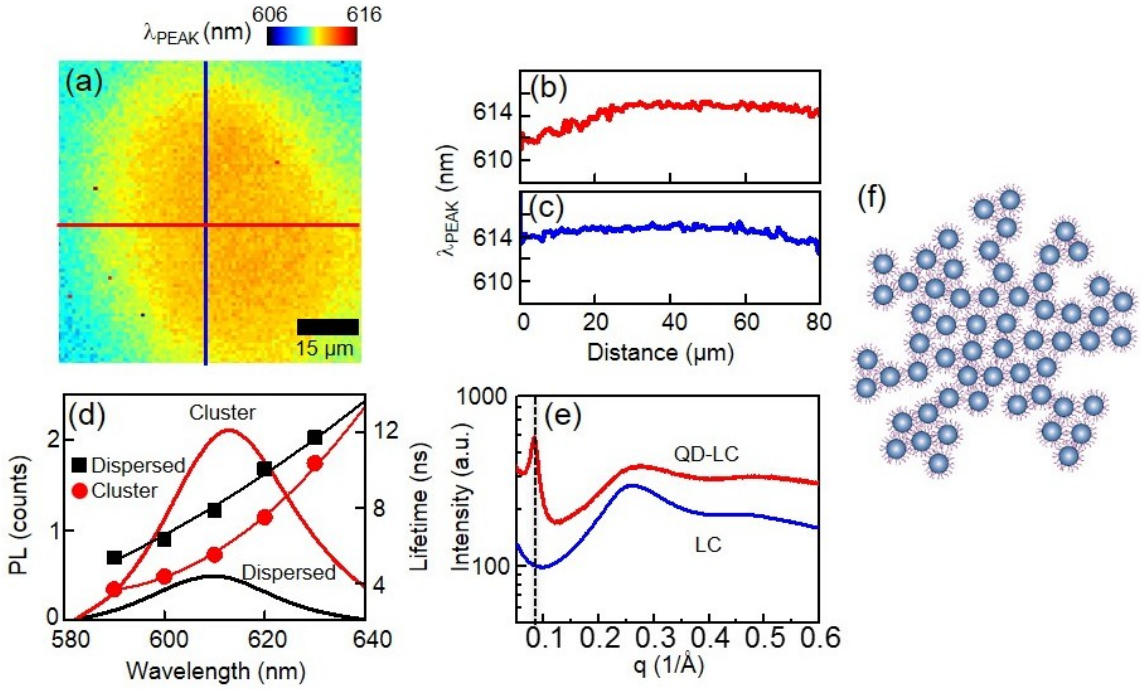

Figure 26: (a) Spatially resolved PL maps of peak emission wavelength focused on a single QD cluster. Line cuts of (a) along (b) horizontal and (c) vertical directions (d) Spectral data from disperse and clustered QDs in nematic liquid crystal. Recombination times for dispersed (squares) and clustered (circles) have been overlaid. (e) Small angle X-ray scattering data from pure LC and QD–LC mixture. Data has been offset for clarity. (f) Schematic model of a QD aggregate.

Fig. 26 shows more detailed characterization of a single QD cluster. A higher resolution PL scan was performed on one cluster (Fig. 26a). Intensity mapping of QD emission reveals that the clusters are more intense at their center but the emission wavelength map in Fig. 26a reveals a relatively uniform red shift throughout the cluster core (Fig. 26b and c). It is interesting to note that areas of higher emission intensity do not produce a larger redshift. This suggests that although there are areas of higher QD concentration in the material, the relative spacing, and hence, the packing density, between QDs within that area remains constant. We can explain this effect by considering the likely structure of a cluster. The QDs used in this study are functionalized with octadecylamine surface ligands that define a minimum spacing between adjacent QDs. In addition, QD clusters likely form by an aggregation process, that may result in a fractal-like structure (Fig. 26f). Such

a cluster, at the resolution of our imaging technique here, would appear uniform in intensity as a function of radius.

To further probe inter-particle distribution, spectrally and time-resolved PL data was collected in order to determine QD recombination times. Fig. 26d shows emission spectra for dispersed QDs (black) and for a cluster of QDs (red). Corresponding recombination times at specific emission wavelengths are plotted across the spectrum. We observe that in both cases the recombination lifetimes increase with emission wavelengths, an indication of some energy transfer from the smaller (lower wavelength) QDs to the larger (longer wavelength) ones. Additionally, while both the dispersed and clustered QDs exhibit exponential decay with a single characteristic lifetime, the clustered QDs recombine at a faster rate at shorter wavelengths while appearing to catch up to, and even surpass (on extrapolation), the recombination rates at longer wavelengths. These observations imply there is increased FRET in the clustered QDs, in agreement with the red-shift seen in Fig. 26a. The efficiency of energy transfer, E_{FRET}, can be determined by comparing the lifetime of the QDs in the cluster, τ_{C}, and in solution, τ_{S};

$$E_{FRET} = 1 - \left(\frac{\tau_C}{\tau_S}\right) \tag{1}$$

Using the lifetimes in Fig. 26d, we estimate a transfer efficiency of between 30.0 and 31.5% across the entire spectrum. The efficiency of the energy transfer can be related to the separation of donor and acceptor, *r*, by:

$$E_{FRET} = \frac{1}{1 + \left(\frac{r}{R_0}\right)^6} \tag{2}$$

where R_0 is the Förster radius, the distance at which the efficiency is 50%. Values for R_0 between separate donor and acceptor CdSe/ZnS QDs [113] should be modified to account for intra-ensemble energy transfer. [114] Taking these modifications into account we can estimate an R_0 of approximately 6.7 nm. Utilizing the measured efficiency we calculate an inter-dot spacing of 7.7 nm.

SAXS was carried out to complement the PL characterization of the QD clusters. A comparison of LC samples with and without QD clusters can be seen in Fig. 26e. The lower curve (blue) in Fig. 26e shows characteristic scattering from a nematic liquid crystal. The broad peaks correspond to average correlation distances between LC molecules. In the upper curve (red), QD clusters are present and a third peak is present at a lower q. We conclude that this peak, at 0.082 Å^{-1}, represents the scattering from QDs located in the clusters with an average QD correlation distance of 7.6 nm. This calculated value seems to indicate close-packing between the QDs. The nematic peaks are unchanged in this QD sample, as expected, since such a low concentration of QDs when dispersed, should have no significant effect on the bulk structure of the LC phase. In general, our nematic liquid crystal medium forms clusters containing QDs close enough to allow energy transfer, but in a typical sample (Fig. 24), the clusters nucleate with a fairly random spatial distribution, guided by the kinetics of the phase transition. For device applications it would be desirable to predict where QD clusters will form and to direct their assembly. To work towards a controllable mechanism for QD cluster assembly, we used a sample geometry in which defects are located in particular spots – prefabricated liquid crystal test cells (Instec Inc.). Randomly scattered 5 μm polystyrene beads are used to maintain an even spacing between the glass plates and for our purposes, each bead acts as a nucleation point for a defect in the LC texture. Now, instead of allowing the QD clusters to form in an uncontrolled distribution, we observed the QD clusters to preferentially locate at the pre-seeded defect points in an otherwise well aligned nematic phase. Fig. 27 shows fluorescence imaging

of the 5CB–QD mixture cooling in a homeotropically aligned LC cell. The spacer beads can be identified as black dots in these images in Fig. 27a–d and it is clear that each bead visible in the image nucleates a QD cluster. These images also reveal an interesting web-like pattern connecting the final clusters also seen in Fig. 25a. The PL maps in Fig. 27e and f from another area in the same sample show numerous small clusters each with a stronger but more localized redshift than observed for the samples prepared without large beads.

When small particles are introduced into an LC phase, the local orientation of the molecules is disturbed. The LC molecule responds to the particle's surface and the presence of a particle creates an elastic deformation of the nematic phase (Fig. 24b). The QDs with octadecylamine ligands used here generate a local splay deformation of the LC director when dispersed and a hedgehog defect. The elastic energy cost of including particles can be minimized by clustering. This explains the difficulty often encountered in trying to disperse different nanoparticles in a liquid crystal phase. In the isotropic phase this elastic deformation problem is eliminated and particles can disperse more readily provided the LC acts as a reasonably good solvent. In our experiments, as the LC phase begins to nucleate and regions of ordered molecules appear and grow, we also observe that previously uniformly dispersed QDs move to occupy the remaining and shrinking isotropic domains. This 'steric sorting', similar to phase separation is explained by considering the energy cost of inserting a single QD into the nematic phase any deformation of the uniform director field will result in an increase in free energy. An additional consequence of this sorting phenomena is that nanoparticles tend to form web-like networks reminiscent of the patterns seen as the nematic phase forms, with QDs concentrated at certain points in the material (Fig. 25 and 27).

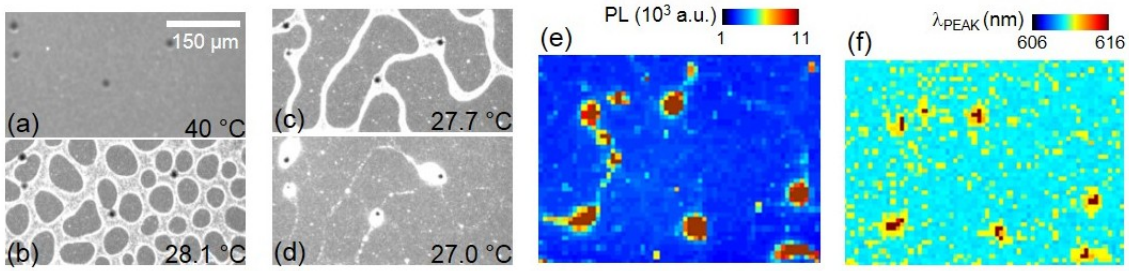

Figure 27: (a–d) Fluorescence microscopy images of a QD ensemble cooling in a cell seeded with polystyrene beads (dark spots in (a)). The QD clusters are centered around the beads. Corresponding QD PL maps showing peak intensity (e) and peak wavelength (f) for a section of the cell. All figures have the same scale bar.

Arrays of large colloidal particles have recently been seen to assemble into well-defined colloidal crystals mediated by the attractive potentials between different topological defects that form around the particles.18 Experimentally, the idea of using defect attractive potentials to assemble particles has not yet been extended to defects containing particles as small as QDs. In a recent study, however, the interactions between 150 nm particles were shown to be long ranged (~1 μm) and relatively weak (<5 k_BT), therefore appropriate for mediating reversible associations. [115] We expect that these effects contribute to observed nanoparticle clustering in the LC phase since particle-containing defects may be weakly attracted to each other. Quantification of this effect will make a fascinating subject for future work as we move toward the idea of directing the assembly of different nanoparticles into more well-defined lattice structures.

8.3 Conclusions

In conclusion, we demonstrate a method for the soft assembly of quantum dots in a composite material. Such materials, incorporating the optical properties of nanoparticles with the processability of liquid crystal are desirable for applications where solutions can be used to generate materials in a desired geometry or coated on a surface. The interaction between LC ordering and particle distribution is used to direct QD pattern formation at the phase transition, resulting in web-like networks, including columnar structures between the glass plates and QD clusters. Inside the clusters the QDs have a consistent interparticle spacing of approximately 7.6 nm, allowing for FRET efficiencies of approximately 30%. We also demonstrate a mechanism for controlling localization of the QD clusters, using defect-generating beads. Ordered clusters of nanoparticles created by liquid crystal templating represent a new class of soft-assembled metamaterials, similar to nanoparticle superlattices. The ideas presented in this paper can easily be expanded to metallic and magnetic nanoparticles by carefully selecting for particle size, surface ligands and the liquid crystal host, creating a wide variety of new materials and applications.

8.4 Experimental Section

Composite material preparation and imaging

Nematic liquid crystal 4'-pentyl-4-biphenylcarbonitrile (5CB, Sigma Aldrich) is mixed with 2 mg ml^{-1} octadecylamine coated CdSe quantum dots (NN Labs) in toluene to a concentration of 0.02–0.04 wt%. Some residual toluene can be left in the material using this method, reducing the isotropic transition temperature by a few degrees. The QD–LC mixture is bath sonicated above the LC clearing temperature (43 ºC) for a minimum of 5 hours to obtain even QD dispersion in the isotropic medium – verified by optical microscopy. A nematic material can be aligned such that the director is uniform over a large area using an alignment layer. A glass slide is cleaned, dip coated with aqueous hexadecyltrimethylammonium bromide (CTAB, Sigma Aldrich) and dried under nitrogen. This coating induces a homeotropic liquid crystal alignment (molecules oriented with their long axis perpendicular to the glass). Samples are sealed with a similarly coated glass cover slip. A Linkham LTS350 hotstage maintained at 40 ºC is used to initially keep the material in the isotropic phase.

Images are captured using a Leica DM2500P upright microscope equipped with a Q-image Retiga camera. This system allows us to observe QD dispersion in the isotropic fluid, while imaging the liquid crystal texture using polarized optical microscopy (POM). LC materials are optically anisotropic, therefore spatial variation in director orientation can be imaged using POM. In the homeotropic geometry used in this experiment, a uniformly aligned nematic appears dark when viewed between crossed polarizers. Defect points are visible and typically take the appearance of bright crosses. Confocal imaging was also carried out using a Nikon Eclipse Ti microscope with a 561 nm excitation laser and a z resolution of ~0.75 μm.

Photoluminescence spectroscopy

A 532 nm continuous wave excitation laser is focused on the sample through a high NA objective to produce a diffraction-limited spot of diameter ~600 nm. Thin LC–QD films similar to those used for microscopy and enclosed in glass slides were mounted on a motorized 3D scanning stage with a 40 nm lateral resolution. Emitted PL from the QDs is collected by the same objective and dispersed by an Acton 300i spectrometer onto a thermoelectrically cooled CCD detector (spectral resolution ~0.18 nm). A selected sample area is raster-scanned to create spatially resolved PL maps.

Time resolved photoluminescence spectroscopy

A 420 nm photo-excitation pulse using the frequency-doubled output of a tunable Ti:sapphire laser with a 76 MHz (13 ns) repetition rate and 150 fs pulse width was used. The excitation power density is kept constant at 45 W cm^{-2}. Time-resolved data are collected using a single photon avalanche detector coupled to a time-correlated single photon counting system (PicoHarp 300) with an instrument response function of 12 ps. Time-resolved PL traces are extracted at a series of emission wavelengths for the sample.

Small angle X-ray scattering (SAXS)

Measurements were carried out on Beamline 4-2 at Stanford Synchrotron Radiation Laboratory. LC.QD mixtures were prepared as described earlier with 0.04 wt% quantum dots dispersed in nematic liquid crystal and pipetted into 1.5 mm quartz X-ray capillaries for unaligned (powder) scattering and exposed to an 11 keV X-ray beam for 0.5 s. Diffraction patterns are recorded on a CCD detector, then plotted as integrated intensity as a function of q, the scattering vector using the SASTOOL analysis software available at the beamline.

9 Dye-integrated cholesteric photonic luminescent solar concentrator

Clustering nanoparticles using the liquid crystal is useful for many applications, but there are other applications that benefit from an even dispersion of fluorophores in the liquid crystal. This chapter explores just such an application using rod shaped dye molecules instead of QDs in order to maintain a high concentration as well as minimize the disruption of the LC director.

9.1 Introduction

First designed and studied in the 1970s, [116, 117] luminescent solar concentrators (LSCs) have recently regained prominence, although with a modified focus. At the time of their initial invention, the most advantageous premise of these devices was that they used smaller amounts of expensive silicon (Si) in comparison with the traditional solar panels. [118] Now, with Si being much cheaper, LSCs have lost that advantage. However, they have other unique properties, including flexibility, [119, 120] and functionality that covers both direct and diffuse lighting, removing the need for tracking mechanisms. [121] This makes them ideal candidates for incorporation in a typical city, where buildings have small footprints but large vertical areas. [122, 123] The usual design of an LSC consists of a transparent glass or polymer sheet, doped with a fluorescent material. The fluorophores are chosen to optimise broadband solar absorption and emission (quantum yield), minimise self-absorption and provide good spectral overlap with the electric band-gap of the photovolatic material located at the edges for the final photocurrent generation. [124, 125, 126, 127, 128] While the choice of fluorophores varies between a wide range of organic dyes, semiconducting polymers and quantum dots, the host is usually an inert matrix. [129, 130, 131, 132] Recently, photonic luminescent solar concentrators (PLSCs) have been developed, in which photonic crystal films are externally applied to an LSC to assist in photon management [133, 134] by reducing escape cone losses. In this configuration, the photonic films act as reflectors across a particular spectral band, enhancing photon confinement within the device. An alternate strategy for creating a PLSC is to use the photonic material itself as the concentrating slab – a concept that was recently explored theoretically. [135] In this work, we have developed a PLSC consisting of a slab of cholesteric liquid crystal (CLC) material. Organic dye molecules are dispersed in the cholesteric film, forming an active fluid one-dimensional photonic cavity with a tunable stop band.

A schematic representation of our LSC is shown in Figure 28(a). In the chiral CLC phase, the rod-like component molecules have short-range orientational order [12] and in our device, are arranged with their rotational axis perpendicular to the top and bottom glass surfaces (planar alignment). The distance over which the LC molecules complete a 360° orientational rotation about this axis is denoted the 'pitch' of the material. The CLC phase exhibits a spectral band-gap when the direction of incident radiation (bold green arrows) is parallel with the chiral rotational axis, therefore acting as a one-dimensional photonic cavity. [1] One critical variation between typical photonic band-gap materials and this CLC-based one is that here the band-gap is 50% reflective [136, 137, 138] as circularly polarized light matching the handedness of the CLC will propagate through the device. An important advantage of using a CLC in this application is that the spectral position of the band-gap can be easily tuned by varying the chirality of the CLC. The dye molecules dispersed in the CLC matrix absorb the incident light and the down-converted emission is waveguided to the edges by total internal reflection (red arrows) where it generates photocurrent in the attached Si PV cells. Normalised absorption and emission spectra of the dye used (Lumogen F Red 300) are shown in Figure 28(b). Figure 28(c) and (d) shows schematics representing the expected differences in device behaviour as the cholesteric band-gap changes. A photonic band-gap centred

on the absorption band will trap incident light more effectively (Figure 28(c)) but be unable to confine the emission, while a band-gap resonant with the emission will not be a very effective absorber, though it will allow better confinement of emitted photons that otherwise would escape the LSC.

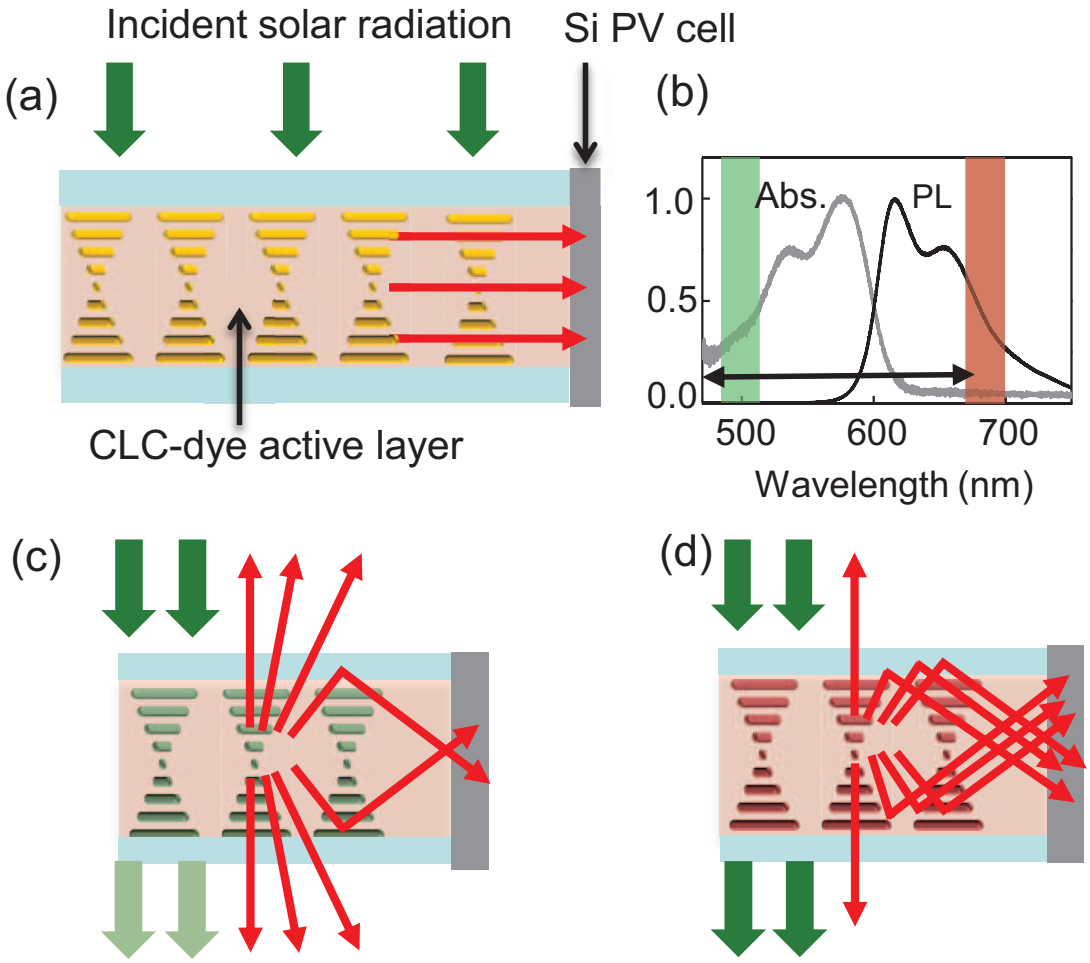

Figure 28: (a) Schematic representation of CLC-dye-based LSC; (b) Normalised absorption and photoluminescence (PL) of the dye. The double headed arrow denotes the spectral range over which we vary the photonic band-gaps for different LSCs; (c) Schematic representation of LSC *A* showing high absorption of incident radiation, but low confinement of emitted light; (d) Schematic representation of LSC *B* showing low absorption but high confinement of emitted light.

Lumogen F Red 300 has a planar molecular structure and is therefore expected to exhibit some tendency to align with the cholesteric host molecules. In a recent publication, [132] this effect was shown to enhance the output current of an LSC using a homeotropically aligned polymerisable nematic LC host slab with the dye Coumarin 6. In that device configuration, the dye molecules aligned with the LC and emitted preferentially to the edges of the device, reducing escape cone losses. In our device configuration, the planar configuration of the cholesteric molecules may produce a dye anisotropy that will act to reduce device efficiency if significant dye alignment occurs. However,

such losses could be offset by the action of the reflection band.

In this study, we design a dye-incorporated composite liquid crystalline LSC where we track optimal performance not only by varying dye concentration and LC phase, but also by tuning the photonic bandgap over the spectral region indicated in Figure 28(b) (double arrows), which allows us to address the contributions of device absorption, surface losses and self-absorption systematically.

9.2 Results and Discussion

The CLC used in the LSC devices is prepared using varying concentrations of the nematic LC, 4'-pentyl'4- biphenylcarbonitrile (5CB, Sigma Aldrich) mixed with the cholesteric LC, cholesteryl oleyl carbonate (COC, Sigma Aldrich). These room temperature LC materials are used as proof of concept only, and ultimately, the device would require LC materials with a significantly higher clearing point. Varying the proportions by weight of COC in 5CB allows us to tune the photonic band-gap of the CLC. Liquid crystal A contains 68% wt COC to create a photonic band-gap centred around 500 nm. Liquid crystal B contains 48% wt COC to create a photonic band-gap centred around 690 nm. The mixtures are sonicated in a heated bath above the clearing point for both component materials (43°C) for 1 h to achieve a homogeneous mixture. The dye, Lumogen F Red 300 (BASF), dissolved in toluene, is then added to the LC mixture to create concentrations of 4 mM, 9 mM and 14 mM composite LSCs. These are again sonicated in a heated bath for 1 h and subsequently removed to a 50°C vacuum oven and maintained at 635 Torr overnight in order to remove residual solvent. The samples are then sonicated one more time in a heated bath for 1 h prior to preparing the LSC.

For LSC production, 1 mm-thick clean glass slides are treated with a 1 wt% aqueous polyvinyl alcohol (Sigma Aldrich) solution on the active side. Once the slide is dry, the surface is rubbed with velvet to create a planar alignment layer for the CLC. Prepared glass is then glued together using Mylar spacers to create cells approximately 10 μm thick. Finished LSCs have an active area of 20 ~ 20 mm and are filled via capillary action while maintaining the isotropic phase and subsequently cooled at a rate of 1°C/minute to a final temperature of 25°C on a Linkam LTS350 hot-stage. Formation of the CLC phase is verified by using polarised optical microscopy to observe the characteristic birefringence texture. Once the cholesteric phase has been verified, we use transmission and reflection data to calculate the absorptance of the LSC. These are measured using a Motic- 150 halogen 150 W cold light source. The LSC is mounted on an Instec HCS302 hot and cold stage to maintain a constant 30°C temperature for cholesteric phase measurements and 40°C for isotropic phase measurements. Spectra collected by an Acton 300i spectrometer are dispersed onto a thermoelectrically cooled CCD with a spectral resolution of ~0.18 nm. The absorptance calculated for a 4 mM dye concentration in LSCs *A* (band-gap centred at 500 nm) and *B* (690 nm) is shown in Figure 29(a and b), for both the CLC (black, 30°C) and the isotropic (grey, 40°C) phases. In LSC *A*, where the band-gap overlaps the dye absorption spectrum, the CLC phase shows a clear increase in absorptance compared to the isotropic phase. In LSC *B*, there is a peak in the absorptance, but that is a result of the incident white light trapped by the LSC and does not enhance the dye properties. For this reason, for photocurrent measurements shown in Figure 32, we use a low-pass filter that cuts off at 650 nm in the incident path. In addition to absorptance, Figure 29 also compares the emission from the edge of the LSCs. While both LSCs have higher-intensity edge emission in the cholesteric phase than the isotropic, the increase is much larger in LSC B, as expected. In all other LSCs with intermediate photonic band-gaps, similar enhancements are seen in absorption and/or emission in the CLC phase when compared to the isotropic.

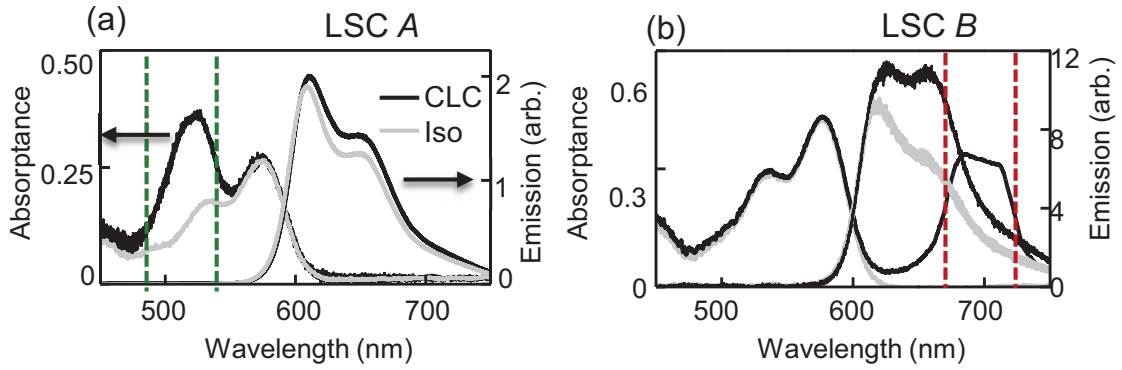

Figure 29: Dye absorption and emission spectra in isotropic (grey) and CLC (black) phases for stop band-gaps centred on (a) 500 nm – overlapping dye absorption and (b) 690 nm – overlapping dye emission. The dashed lines indicate the spectral positions of the band-gaps.

Apart from incident absorption and emission, self absorption is an additional factor that impacts the efficiency of any LSC. It is the result of spectral overlap between the absorption and emission bands (Figure 28(b)), which causes reabsorption of emitted photons by the dye molecules themselves. Self-absorption worsens with length of travel of the emitted photons and manifests itself as reduced emission intensity and overall spectral redshift in the light that finally reaches the edges. [139] To assess the role of concentration and photonic band-gap position in self-absorption in our cells, we perform spatially resolved spectral measurements. The cell is mounted on a motorised translation stage and coupled to an optical fibre at the edge. A collimated incident beam is used to excite a 2-mmdiameter spot on the cell. The distance between the excitation point and the collection fibre at the edge is continuously varied by translating the LSC.

Figure 30(a and b) shows the dye emission spectra at different distances between the excitation and collection spots for LSCs *A* and *B*, at 4 mM dye concentration. The emission is spectrally bimodal and as the distance between excitation and collection increases, we observe the weight distribution shifting from lower (labelled 'Peak 1') to higher (labelled 'Peak 2') wavelengths, accompanied by a decrease in intensity, both typical signatures of self-absorption by the dye molecules. Dye concentration is an additional parameter that influences self-absorption considerably. In Figure 30(c and d), we show the spectral weight of each peak for 2.5 mm and 10 mm separations for two different concentrations obtained from fits to spectral curves as shown in Figure 30(a and b). At 4 mM, (Figure 30(c)), the spectral shift is very similar in both LSCs, as is the overall intensity drop (ranging from22%to 23%). At 9mMof dye, differences show up. For LSC *A*, 15.2% of the lower peak weight shifts to the higher one, but for LSC *B* this shift is 23%, which would imply greater self-absorption. However, the weight shift does not correlate to overall decrease in intensity. The intensity loss for LSC *A* is 55% for 9mM, while for LSC *B* it is only 46%. This is unusual in typical LSCs, where greater relative spectral weight redshift almost always indicates increased self-absorption and corresponding loss of yield. [140] We speculate that most likely LSC *B* does have more self-absorption, but this effect is masked by the higher degree of confinement due to the photonic band-gap.

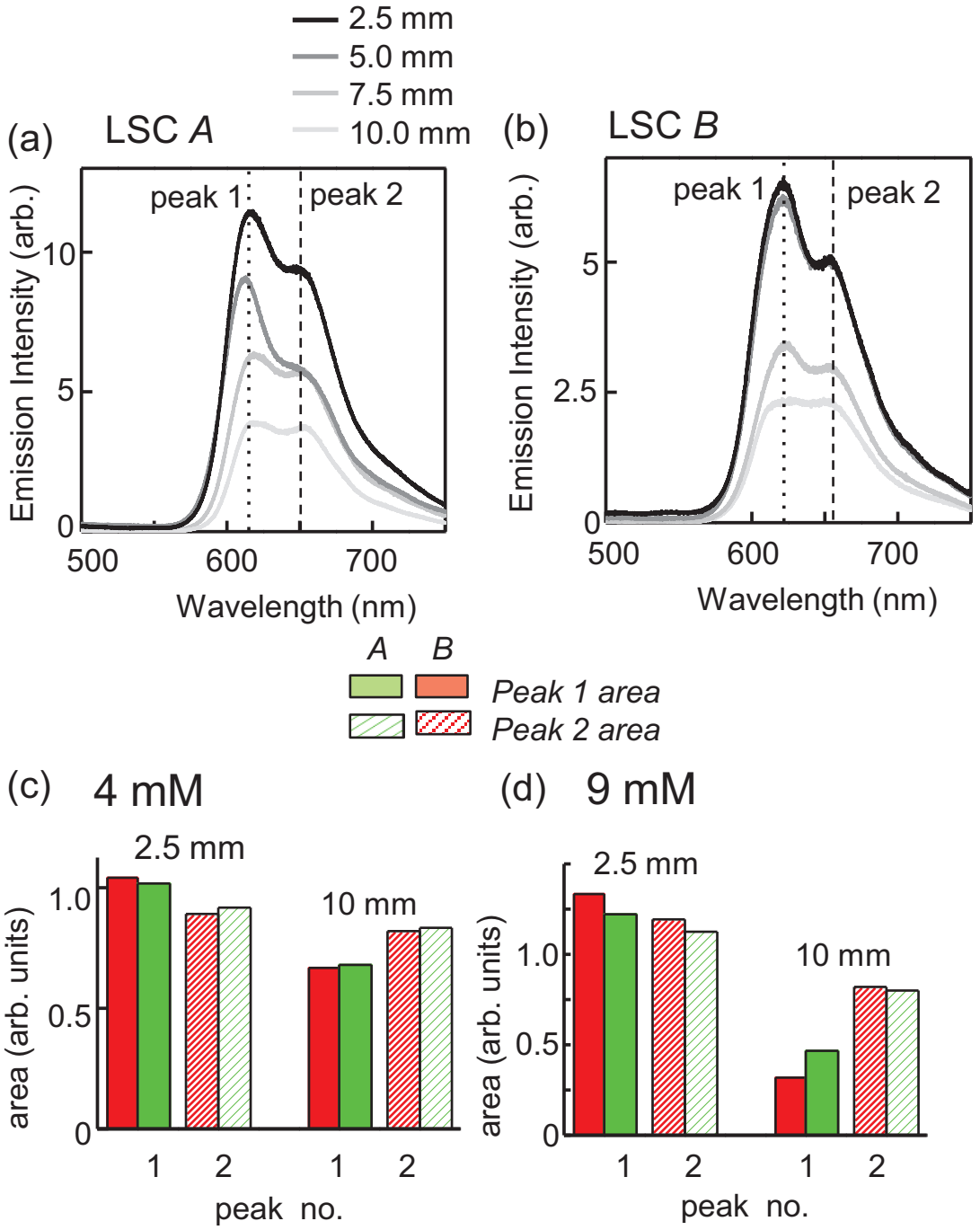

Figure 30: Evaluation of self-absorption losses using pump-probe technique. The emission spectra are shown for different pump-probe separations for (a) LSC *A* and (b) LSC *B*. Dotted and dashed lines indicate the spectral positions of the two peaks, designated Peak 1 and Peak 2. The comparative weights of each peak for the two devices with pump-probe separations of 2.5 and 10 mm are shown for (c) 4 mM and (d) 9 mM dye concentrations.

After these fundamental optical characterisations, we move onto photocurrent measurements. These are carried out by mounting a Si photovoltaic cell with an active area of 2 × 30 mm to the edge of the LSC using index-matched adhesive (Norland 78). To control the phase of the CLC, the LSCs are then mounted on an Instec temperature stage with a reflective white backing layer between the LSC and the stage. The LSC is maintained in the CLC phase (30°C) for 6 minutes and the photocurrent, (I_{LSC}) is measured every 10 seconds. The variation in I_{LSC} with time is shown in Figure 31. Incident light is blocked periodically, indicated by breaks in the data. At the end of the 360 seconds, the LSC is heated to the isotropic phase (40°C) and data are taken for another 360 seconds. Figure 31(a) shows the normalised I_{LSC} for a well-aligned cell (transmission image in Figure 31(b)) in which the current drops 2% after being heated to the isotropic phase. The observed current jump immediately after 360 seconds in Figure 31(a) is a result of the phase change at that point. By comparison, I_{LSC} of a poorly aligned LSC in which many defects disturb the planar alignment, as verified by the defect-rich disordered transmission image in Figure 31(d), is shown in Figure 31(c). Poorly aligned LSCs showed a less-consistent I_{LSC} that increases when the LSC is heated into the isotropic phase. Clearly, the presence of a photonic band-gap in a well-aligned LSC leads to improved performance.

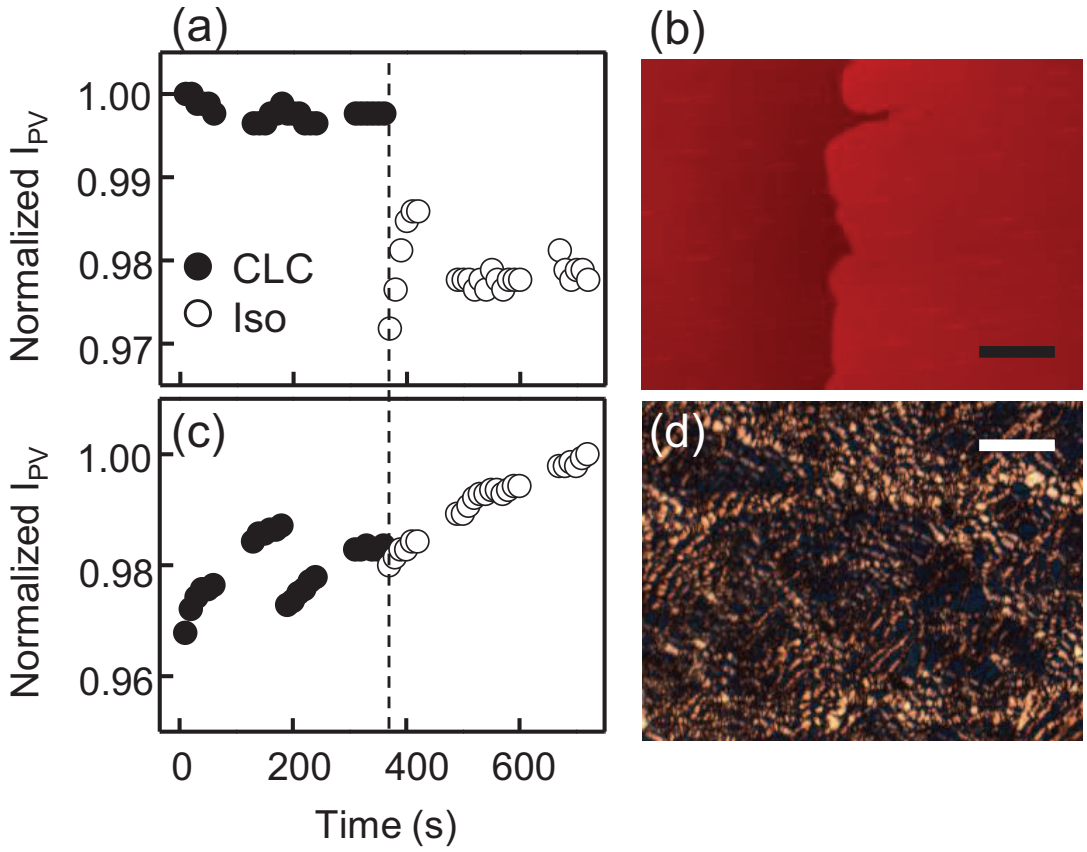

Figure 31: Photocurrent as a function of time for (a) a well-aligned device with a photonic band-gap centred on 690 nm (b) and a poorly aligned control LSC. (c, d) Transmission images of the well- and poorly aligned LSCs, respectively. The dashed line indicates the time when LSCs were heated to the isotropic phase. Scale bar is 50 μm.

Next, we investigate how this improved performance varies with the spectral position of the photonic band-gap, with particular focus on whether absorption or emission plays the greater role in device efficiency. We define the absorption efficiency for different LSCs as the total light absorbed by the LSC divided by the total light incident upon the LSC:

$$\eta_{Abs} = \int_{\lambda} I(\lambda) A_{bs}(\lambda) d\lambda \Big/ \int_{\lambda} I(\lambda) d\lambda \tag{3}$$

where $I(\lambda)$ is the light incident upon the LSC and A_{bs} (λ) is the absorptance, calculated from measured absorption spectra, such as in Figure 29. The absorptance for different LSCs is normalised to the peak of the dye absorption to remove effects of concentration or thickness. Optical efficiency is defined as:

$$\eta_{OPT} = (I_{LSC} \times A_{PV}) / (I_{PV} \times A_{LSC}), \tag{4}$$

where I_{LSC} is the current generated by the LSC attached to the PV cell, I_{PV} is the short circuit current of the bare PV cell, A_{LSC} is the area of the top of the LSC and A_{PV} is the active area of the PV cell. The ratio of $A_{\mathrm{LSC}}/A_{\mathrm{PV}}$ is referred to as the geometric factor for the LSC. We calculate η_{Abs} and η_{OPT} for all our LSCs in both the CLC and isotropic phases and observe a maximum η_{OPT} of ~12% in LSC B. However, here we show the percentage change for each of the efficiencies between the two LC phases in Figure 32(a) and (b). For most LSCs, η_{Abs} is higher in the CLC phase, and, as expected, this improvement diminishes as the photonic band-gap shifts to higher wavelengths. The LSCs with a band-gap >650 nm show barely any change between the isotropic and the CLC phase. The optical efficiency, on the other hand, shows the opposite trend. We observe that despite exhibiting higher absorption in the CLC phase, LSC with band-gaps centred in the 500– 600 nm range do not have a corresponding increase in η_{OPT}. Instead, the most consistent increase in η_{OPT} comes from the LSCs with photonic band-gaps centred above 650 nm, even though those devices have lower η_{Abs} in the CLC phase and additionally suffer from higher self-absorption. The effect of dye concentration on device efficiency shows the most dilute LSC performs the best. With increasing concentration self-absorption gets worse (as seen in Figure 30) and usually that is compensated by higher incident absorption. In these LSCs even that is not the case, which is most likely due to the CLC phase (and in effect, the band-gap) being less uniform and well defined as more dye is added to the LC.

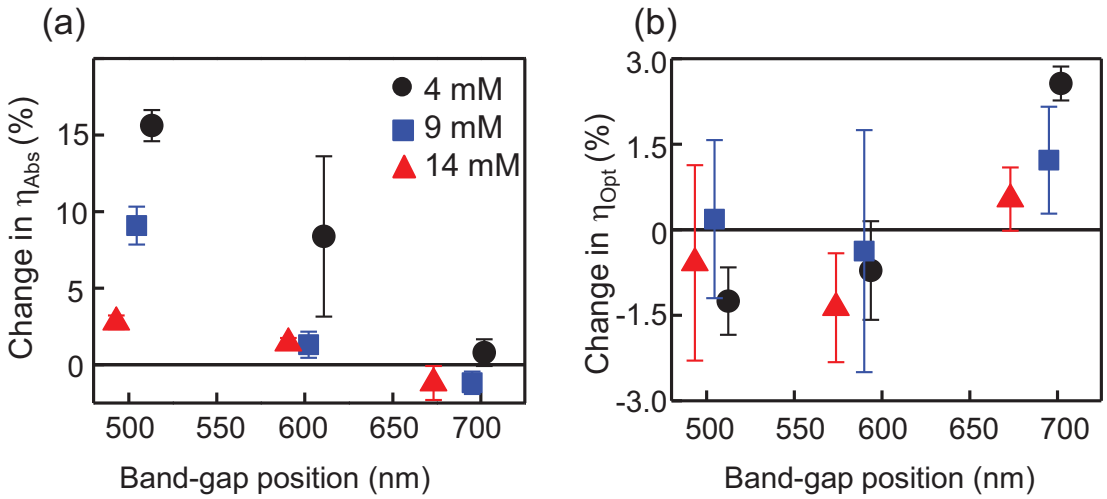

Figure 32: (a) Change in absorption efficiency (η_{Abs}) and (b) change in optical efficiency (η_{OPT}) from CLC to isotropic phase.

9.3 Conclusions

Our studies establish the important result that when using a photonic band-gap type material to enhance performance of an LSC, matching its spectral stop band to maximise emission confinement is more advantageous than trying to enhance incident absorption. In addition, the use of a thin-film composite material that performs the dual functionality of providing both the down conversion of absorbed photons and the photonic band-gap-related confinement of emitted photons makes our devices viable candidates for solution-based processing of LSCs that can be easily incorporated as thin-films onto windows and other similar surfaces.

10 Tuning quantum-dot organization in liquid crystals for robust photonic applications

In order to create photonic LSCs with QDs or QD/LC lasers, a high concentration of QDs is required. In this section we discuss our efforts to modify the ligands of the stock QDs to make it more energetically favorable for QDs to remain dispersed in the LC with minimal disruption to the director.

10.1 Introduction

Semiconductor nanoparticles (quantum dots, QDs) have generated significant interest because of their unique size-tunable properties arising from quantum confinement effects. Such particles have been shown to be useful as building blocks for a wide variety of applications, such as in optoelectronic devices, drug-delivery systems, and biochemical sensors. [141, 142, 143, 144, 145] Recently, significant work has been carried out on developing hybrid liquid crystal (LC)/nanoparticle materials. Studies have looked at creating stable dispersions of metallic, magnetic, and semiconductor particles in the nematic, [146, 147] smectic, [148, 149] and columnar [107, 150] thermotropic phases. [111] Different nanoparticles have been shown to readily localize in regions of low order in the LC phases and to stabilize the defect-rich blue phases [151] and the twist grain boundary phase [152] over a wide temperature range.

One of the key challenges in designing nanoparticle/LC hybrid systems for photonic applications is their stabilization as a composite material over long time periods. Nanoparticles exhibit properties not seen in their bulk phase, and bare nanocrystals (not surface-functionalized) are strongly attracted to each other by electromagnetic forces, producing effectively permanent particle aggregates and complete separation from the solvent. Nanoparticles incorporating surface ligands can avoid this fate if there is an entropic cost to close particle-particle approach. By considering the thermodynamics of the LC/ nanoparticle system, surface ligands can be carefully designed to act as a surfactant between particle and solvent. In general, the surface ligands on a particle will define the alignment of the surrounding LC molecules. In the case of large particles (greater than 1 μm in diameter), this interaction is analogous to the surface-anchoring conditions of an LC device. For example, simple single-chain ligands, such as octadecylamine (ODA), coating a large particle surface will induce homeotropic LC alignment for typical calamitic materials and therefore a radial distribution of LC molecules at the particle surface, producing a defect around the particle in the nematic phase. [48, 3] The inclusion of microscale particles in the nematic phase has been explored extensively in recent years. For large colloidal particles (< ~500 nm in diameter), different topological defects have been shown to form and can be imaged optically [103, 153, 41] and even manipulated using the focused light beam of an optical trap. [51] Such work relies primarily on optical imaging and although recently smaller colloids (~100–500 nm diameter) [154] have been examined, detailed characterization of particles less than 50 nm in liquid crystal solvents is still a challenge and must be deduced by more indirect means.

For large particles, elastic deformation of the host LC phase dominates the physical behavior, but in the case of small nanoparticles approaching the length scale of LC molecules, bulk elasticity descriptions must give way to consideration of discrete interactions between the surface ligands and the LC molecules. Entropic forces, excluded volume effects, and local order parameter perturbations become important in understanding the phase behavior of the system. [109]

The free-energy cost of adding nanoparticles to an LC phase typically promotes either particle clustering, in which particles are depleted from a local area into a small aggregate, or total phase separation. The particles are recruited to regions of low order in the case of existing defects, and across the isotropic to- nematic phase transition, particles preferentially locate in the disordered isotropic phase, leading to pattern formation. [48, 3, 109]

A lack of control over nanoparticle aggregation in LC materials has hampered fundamental research efforts to produce composites with a well-defined structure. Possible material outcomes range from well-separated "colloidal" dispersions of isolated particles to dispersions that include ordered nanoparticle clusters. Even at relatively low particle concentrations (less than 1 wt%), nanoparticles readily aggregate into large flocs and precipitate out of the LC over a period of hours, unless their surface properties are carefully designed.

To address this problem, there have been recent attempts to design nanoparticles with mesogenic liquid-crystal-like ligands using gold [37, 155, 106] and semiconductor [156] nanocrystals. These strategies have proved effective in modulating nanoparticle dispersal in the nematic phase. In general, it has been shown that a rodlike mesogenic segment built into the ligand can align with the surrounding phase, decreasing the free-energy cost of inserting a single nanoparticle when compared to non-mesogenic ligands, such as ODA.

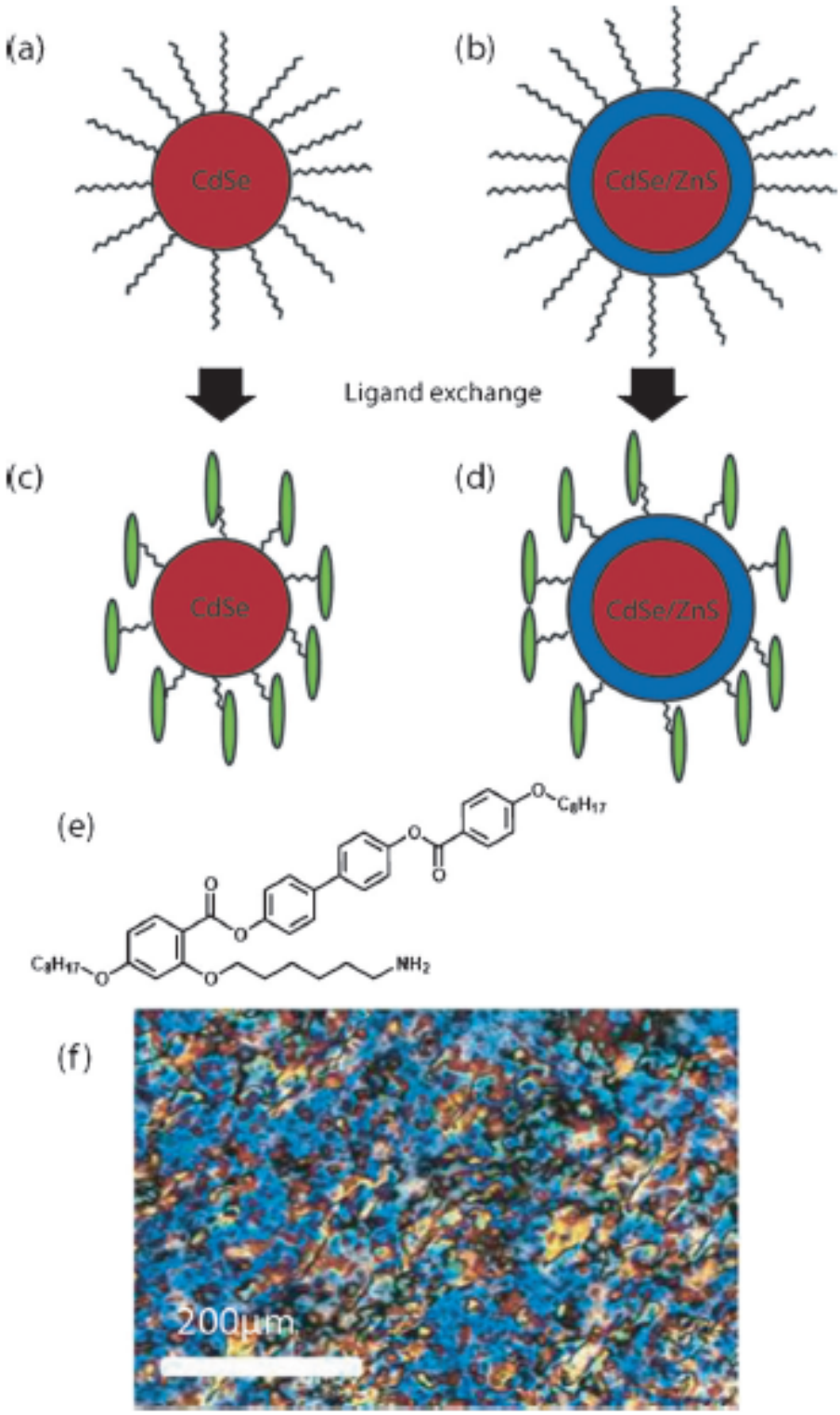

Figure 33: Schematic representation of (a–d) the different quantum dots used in this study including non-mesogenic ODA ligands and the LC ligand (green). e) Molecular structure of the mesogenic ligand (11) and f) nematic phase of **11** at 130 ºC, imaged by using polarized optical microscopy.

Designing surface-modified QDs for colloidal dispersal or controlled cluster assembly in LC phases is an important goal in the development of soft switchable *meta*-materials for photonic applications. Recently, our group has investigated ODA– QDs as emitters in a cholesteric cavity. [82, 1, 34] These nanoparticles tend to form reversible microsized clusters when dispersed in the LC solvent. [3] A finer control of QD assembly either by complete dispersal or controllable cluster packing will greatly enhance the possibilities of these materials for fluid based self assembling *meta*-materials.

In this Article we describe the synthesis of new QDs functionalized with a mesogenic ligand (LC–QDs). We use both core-only (CdSe) and core/shell (CdSe/ZnS) dots, characterizing their dispersion in the nematic and cholesteric phases after ligand exchange. A flexible ligand arm is designed to allow the rodlike mesogenic segment to align with the surrounding LC molecules in the nematic phase, minimizing local deformation of the LC director. Polarized and fluorescence microscopy studies show that the addition of mesogenic ligands prevents particle clustering in the nematic phase at low concentrations when compared to ODA–QDs. At higher concentrations, QD rich clusters form, and by using a combination of X-ray diffraction and photoluminescence (PL) imaging we demonstrate that LC–QD cluster packing in the nematic phase is significantly different to that seen for ODA–QDs. Combining different techniques in a multiscale approach allows us to completely characterize the hybrid material, probing particle packing and interactions for different LC/QD combinations.

10.2 Results and Discussion

10.2.1 Quantum-Dot Synthesis and Characterization

To investigate the effects of mesogenic ligands on QD dispersion and the photonic properties of QD/LC hybrid materials, we prepared four different particles, core only and core–shell QDs with either mesogenic (LC–QDs) or ODA ligands (ODA– QDs), as depicted in Figure 33. The ODA ligand has been previously shown to promote nanoparticle clustering on both gold and semiconductor particles, [3] whereas mesogenic ligands attached to gold particles have been recently demonstrated to promote more uniform dispersion in the nematic phase. Recently, dendrimer-like ligands were also successfully designed to optimize QD dispersion in a liquid crystal. [156]

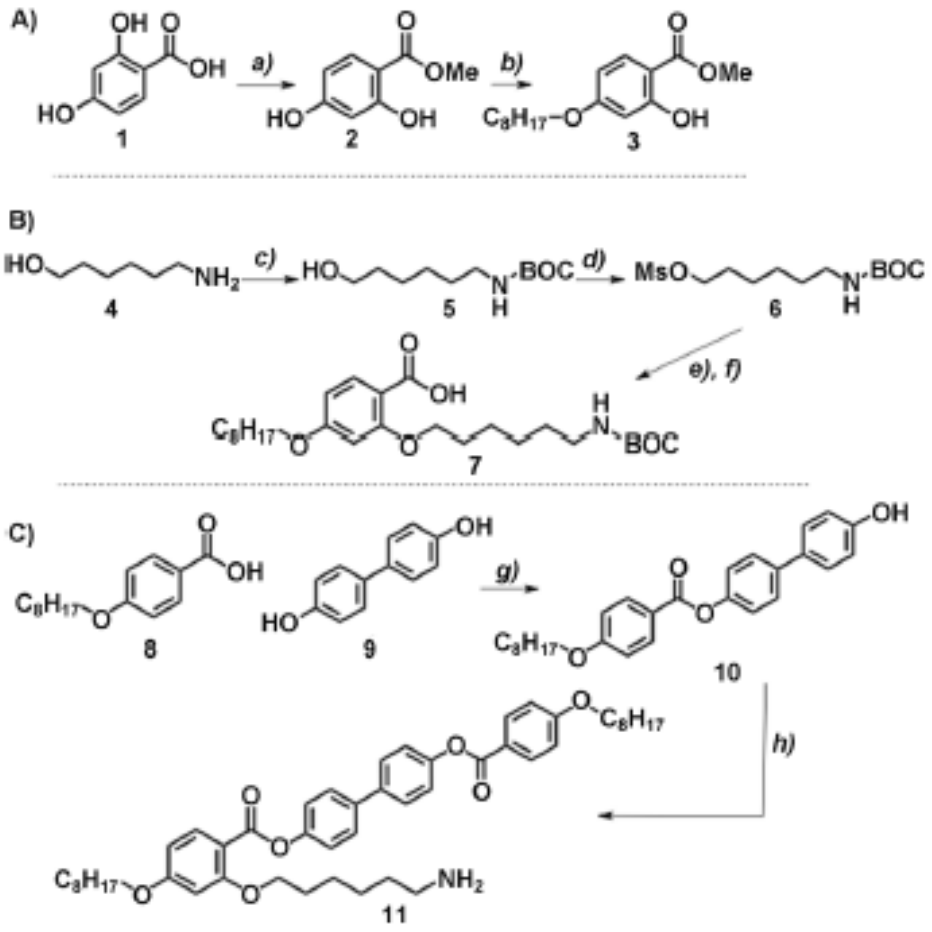

Figure 34: Synthesis of the liquid-crystal ligand: a) H_2SO_4, MeOH; b) 1-bromooctane, K_2CO_3, 2-butanone; c) $(BOC)_2O$, DCM; d) MsCl, TEA, DCM; e) KOtBu, KI, 2-butanone; f) NaOH, MeOH; g) DMAP, EDCI, TEA, THF; h) $SOCl_2$, toluene

ODA-functionalized QDs were supplied by NN Labs Inc. The mesogenic ligand (**11**) was synthesized as shown in Figure 34. Compound **11** (Figure 33e) is liquid crystalline, forming a nematic phase in its pure state. A liquid-crystal texture for this phase is shown in Figure 33f. The rigid core of compound **11** consists of a typical mesogenic unit, while the flexible arm segment allows rotation of the core once attached to a particle surface. Starting with ODA–QDs, a ligand exchange was performed on both core only and core/shell QDs to replace ODA with compound **11**.

Figure 35 shows absorption and emission spectra for each of the four particle types, that is, before and after the ligand exchange. Comparing data before and after the exchange process highlights some important differences between the core-only and core/shell semiconductor particles. These plots reveal that the core-only QDs exhibit a significant blue shift in both the absorption and emission spectra after attachment of the new ligand (Figure 35a,b). In contrast, the core/shell particle spectra are almost unchanged after the ligand exchange. QDs prepared without a shell are highly susceptible to oxidation of the core, and this leads to an effective reduction of the QD size. Since the spectral properties of QDs depend on the particle size, a blue shift in absorption and emission

can be attributed to core oxidation. In addition to this blue shift, we also observed that the core-only QDs' emission intensity was significantly reduced after the exchange. This effect may be due to oxidation-induced surface-defect states that trap electrons, quenching PL emission. For these reasons, core/shell QDs should be preferred for photonic applications where stability and quantum efficiency are important performance factors. The use of a protective ZnS shell does increase the overall particle size; however, the additional bulky ligands will increase the minimum obtainable QD separation, a possible factor in applications.

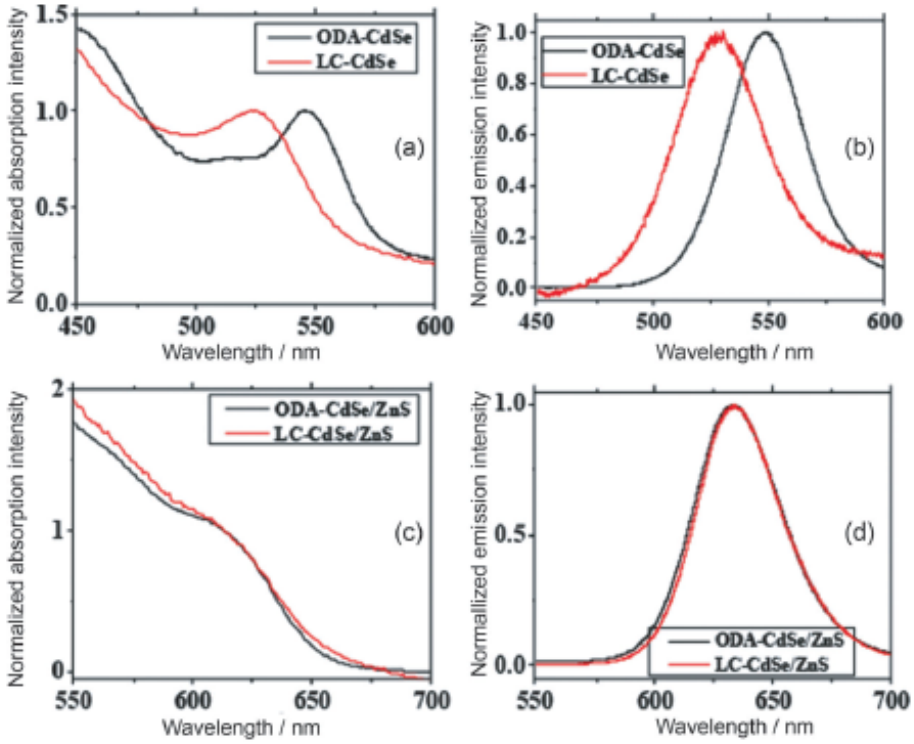

Figure 35: Absorption (a, c) and emission (b, d) spectra for ODA- and LC–QDs in toluene with core-only (a and b) and core/shell (c and d) QDs. Each graph shows spectra taken before and after the ligand exchange.

10.2.2 Quantum-Dot Organization in the Isotropic and Nematic Phases

The goal of this investigation was to characterize the differences between LC–QDs and ODA–QDs when dispersed in nematic and cholesteric liquid crystals with a view towards their use in photonic applications. Therefore, we began by looking at the structure of particle dispersions in the isotropic and nematic phases of the nematic liquid crystal (4-cyano-4'-pentylbiphenyl, 5CB). Using a suite of techniques we cannot only probe QD organization on the microscale, but also characterize particle separation and spectral characteristics on the nanoscale.

Our particles are dispersed in an anisotropic fluid, and so the structure of the composite material is expected to depend on the surface properties of the particle and the liquid-crystalline properties of the host phase. Here, we compare two different cases of surface anchoring, homeotropic alignment using ODA–QDs and LC anchoring using LC–QDs. In the latter case, the rodlike molecule (**11**)

attached to the particle surface is expected to locally align with the host LC director.

Mixtures were prepared at different QD concentrations in 5CB and imaged using fluorescence microscopy over a range of different concentrations from 0.02 wt% up to 0.15 wt%. In general we found that none of the particle types prepared dispersed uniformly in either the isotropic or the nematic phase above 0.02 wt%. Clear differences could be seen, however, between the ODA–QD and LC–QD particles, particularly at low concentrations. Figure 36 shows a comparison of mixtures prepared with the core/shell QDs in the isotropic phase at two different concentrations after 6 hrs of sonication at 43ºC. These fluorescence images highlight micron-scale QD spatial organization in each of the mixtures. Figures 36a,b and 36e,f demonstrate that in the isotropic phase the LC–QDs show enhanced dispersion at both 0.02 wt% and 0.10 wt% with no large clusters visible under the microscope. We observed that the ODA–QDs were only fully dispersed in the isotropic phase (as can be determined by optical microscopy alone) at concentrations <0.05 wt% with sonication of up to 18 hrs. In comparison, the LC–QDs dispersed well up to concentrations of 0.15 wt% with a 6 hr sonication time.

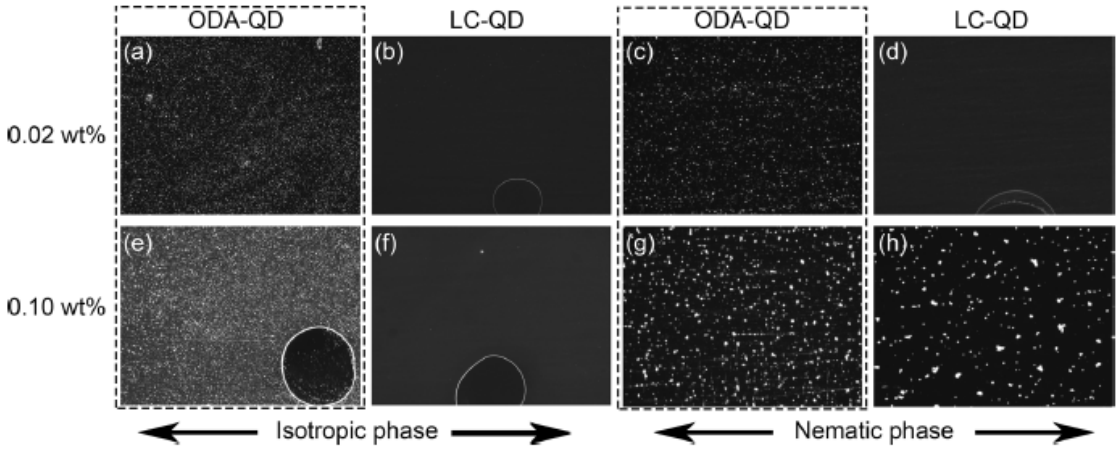

Figure 36: Fluorescence microscopy images of different surface-functionalized QDs in the isotropic and nematic LC phase (5CB). a) ODA–QD, 0.02 wt%, isotropic. b) LC–QD, 0.02 wt% isotropic. c) ODA–QD, 0.02 wt%, nematic. d) LC–QD, 0.02 wt%, nematic. e) ODA–QD, 0.10 wt%, isotropic. f) LC–QD, 0.10 wt% isotropic. g) ODA–QD, 0.10 wt%, nematic and h) LC–QD, 0.10 wt%, nematic.

When we compare the macroscopic differences between ODA–QDs and LC–QDs in the nematic phase (Figure36c,d,g,h) we can immediately see that dispersion is less favorable for the ODA–QDs. At the lower concentration (0.02 wt%), LC–QDs disperse uniformly, but ODA-QDs do not; microsized quantum dot clusters form throughout the material. We observed that the cluster size is a function of cooling rate (from the isotropic to the nematic phase) and concentration. This is expected, since clusters nucleate as a result of thermal particle motion and subsequent depletion from a local area.

For nanoscale particles dispersed in a liquid crystal, entropic effects arising from discrete interactions between surface ligands and surface-localized LC molecules become increasingly important to the phase behavior. [154] The results shown in Figure 36 support this hypothesis, as we can note that in the isotropic phase there are still dispersion differences between QDs with different ligands despite the fact that the nematic director is no longer present. These differences can be attributed to

local ligand–LC interactions near the particle surface.

Fluorescence imaging cannot provide any information on QD organization within clusters below the resolution of light microscopy; therefore, to investigate the material structure in more detail, we performed scanning confocal PL microscopy on the different mixtures. This technique, applied previously by our group, [1, 34, 2] produces PL intensity maps of a 1 μm thick slice combined with emission spectra for each pixel recorded. PL microscopy provides a unique method for characterizing the distribution of fluorescent particles in liquid crystals, as energy-transfer processes, such as Forster resonance energy transfer (FRET), can be detected. In this case, if two particles are close together (<12 nm), FRET produces an average red shift in the QD peak emission as a function of the particle separation. This information can be used to determine the average particle separation within a cluster. [48]

Figure 4 shows PL intensity maps with the corresponding peak-wavelength maps for four different materials: ODA–QDs and LC–QDs in the nematic phase at both 0.02 and 0.1 wt%. In each of the images shown, we focus on a large microscale QD cluster where present. By mapping the peak emission wavelength across a QD cluster, differences in nanoscale particle packing can be elucidated.

Starting at a low concentrations of QDs, the images in Figures 37a,e are consistent with the fluorescence microscopy images shown in Figure 36. The ODA–QDs cluster into defined aggregates whereas the LC–QDs do not. Notice that in Figure 37b, (the peak emission wavelength map corresponding to 37a), there is a significant red shift inside the cluster compared to isolated particles outside the cluster. This indicates that the QDs inside the cluster are relatively closely packed and consistent with recently reported X-ray scattering and PL data, [48, 2] giving an average QD–QD separation of 8.7 nm. Similar results are also seen at higher concentrations (Figures 37c,d).

In Figure 36, we see that the LC–QDs show cluster formation at 0.1 wt%. By comparing the PL spectra with those of the ODA–QD clusters, differences become apparent. Figures 37g,h clearly show that LC–QD clusters exhibit a minimal red-shift. From this result we can conclude that the particles must be 10 nm apart within the assembly.

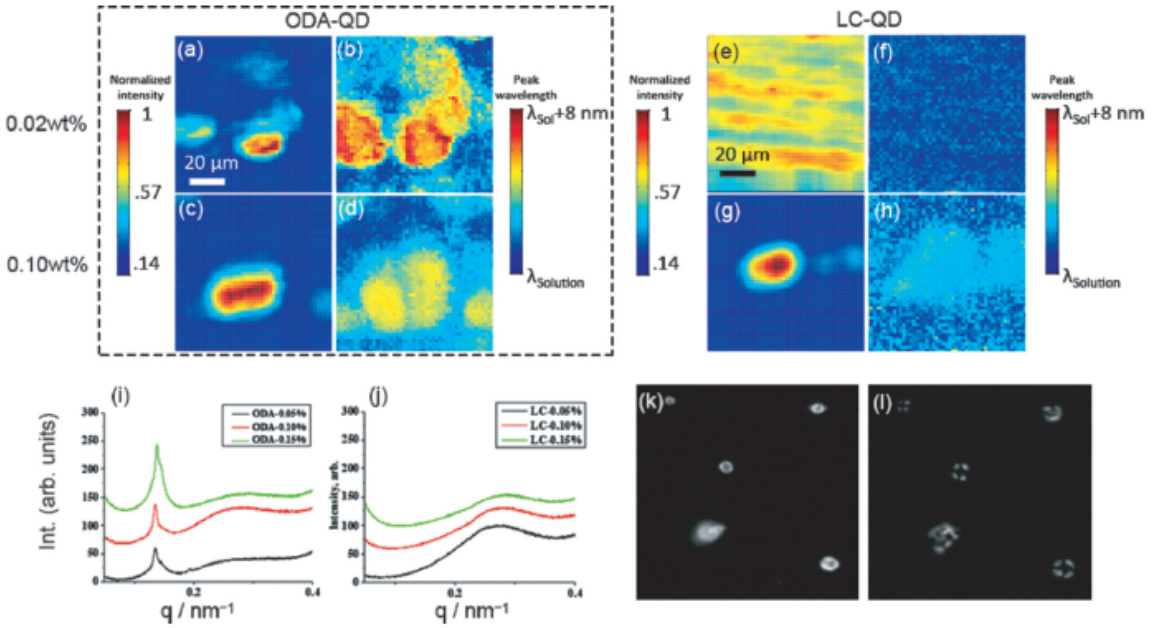

Figure 37: Photoluminescence confocal microscope images of CdSe/ZnS QDs in nematic LC (5CB) are shown for two different concentrations. a) Intensity map and b) peak wavelength map for 0.02 wt% ODA–QD. c) Intensity maps and d) peak wavelength maps for 0.1 wt% ODA–QD. e) Intensity map and f) peak wavelength maps for 0.02 wt% LC-QDs. g) Intensity maps and h) peak wavelength map for 0.1 wt% LC–QDs. Small angle X-ray diffraction data is also shown for i) ODA–QDs at different concentrations in a nematic liquid crystal and j) LC–QD. k) Fluorescence microscopy image of nematic-like LC–QD-rich droplets at 0.1 wt% in 5CB. l) Polarized microscopy image of a similar sample both taken with a 10x objective.

Figures 37i,j show small angle scattering data for the core only QDA–QDs and LC–QDs, dispersed at 0.05, 0.10, and 0.15 wt% in 5CB. Figure 37i shows a clear scattering peak at 0.13 nm^{-1} for all three concentrations. In a disordered particle aggregate with a characteristic particle–particle separation, such a peak corresponds to the average distance between neighboring particles. [103] This peak indicates that the particles have a relatively well-defined separation within the aggregates of 4.8 nm. In the case of core QDs with ODA ligands, this indicates a gap of ~1.7 nm between QDs with some interdigitation of the ODA chains. Carrying out the same measurement on dispersions prepared with the LC–QDs reinforces our conclusions from the PL imaging. The correlation peak is no longer present (Figure 37j) at any of the concentrations studied. Despite the clear presence of the aggregates visualized using fluorescence microscopy, no X-ray peak was detected after scanning multiple samples and sample regions. This result indicates that the LC–QD aggregates seen with microscopy are more disordered and fluid-like than those observed in the ODA–QD system, with no well-defined inter-dot spacing.

Above 0.05 wt%, close-up fluorescence imaging carried out using a 40x microscope objective reveals that the LC–QD clusters are actually spherical liquid-crystalline droplets and not the irregular aggregates more characteristic of the ODA–QDs. This can be seen by looking at fluorescence (Figure 37k) and polarized (Figure 37l) microscopy images of the same sample area. The LC–QDs form luminescent droplets within the host nematic phase and using a planar alignment for the host

phase aligned with one of the polarizers birefringence from the QD-rich structures can be seen with characteristic nematic extinction crosses clearly visible.

These results, when combined with findings from the X-ray measurements and PL spectra provide evidence of fluid–fluid phase separation into a 5CB-rich phase and an LC–QD-rich phase. This result is consistent with observations of LC phase formation in systems of pure LC functionalized nanoparticles [155, 106] and demonstrates how LC ligands much as these can lead to a rich phase behavior. The results described in this section also highlight the importance of carrying out a multiscale characterization of these hybrid materials.

On much larger length scales, QD/LC mixtures have been recently demonstrated to produce interesting patterns, as the materials are slowly cooled from the isotropic to the nematic phase. [3, 109] Particles dispersed in the isotropic phase will seek regions of low order at the phase transition, clustering at defect points. Figure 38 shows an example of this phenomenon for the ODA- and LC–QDs. Figures 38a–c show fluorescence and PL images of ODA–QD clusters in the nematic phase. The PL maps of intensity and peak wavelength reveal that these clusters are relatively densely packed with an average QD spacing of 8.7 nm within the cluster as characterized by their FRET red shift. In comparison, imaging the LC–QDs as the mixture is cooled slowly (Figures 38d–f) reveals some bright clusters with an additional diffuse wormlike pattern. The diffuse pattern forms as the QDs move into the remaining isotropic regions as the material is cooled to the nematic phase. Similar patterns for ODA–QDs have also been observed on very slow cooling. [48] The PL images for this mixture (Figures 38e,f) show that neither the brightest clusters or the diffuse pattern exhibit any significant red shift, demonstrating that the LC–QDs are at least 12 nm apart across the sample. Analysis of such pattern formation using a combination of fluorescence and PL imaging should provide an interesting probe into the thermodynamics of these systems and will be the subject of future investigations.

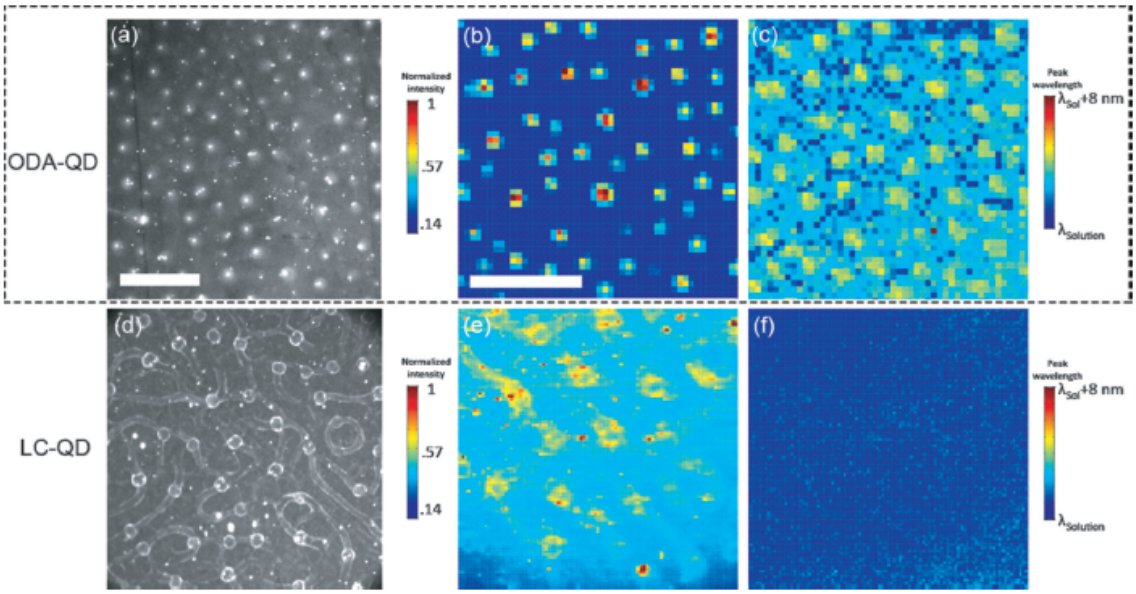

Figure 38: Images characterizing large-scale pattern formation in nematic/QD mixtures comparing the ODA and LC ligands. Fluorescence microscopy (a,d), photoluminescence intensity (b,e), and peak emission wavelength (c,f) for ODA–QD and LC–QDs at 0.1 wt% in 5CB are shown (scale bars=200 μm).

10.2.3 Performance in Soft Photonic Devices

The ability to stably disperse QDs in a liquid-crystal host material provides us with the possibility of soft-assembling photonic devices. In cholesteric devices, embedded QDs can act as emitters coupled to a tunable fluid cavity, producing applications such as the quantum dot liquid crystal laser [157] and switchable cavities able to spatially modulate QD emission. [1, 2] The efficiency of such devices will depend on our control of co-operative effects between adjacent particles. For example energy transfer processes such as FRET can reduce the efficiency of QD cavity coupling if the particles are closely packed in aggregates. Therefore by designing appropriate QD ligands, particle clustering and dispersion can be tuned to optimize device performance.

Figure 39 shows a comparison of the ODA–QD and LC–QD emissions in a cholesteric cavity. The plots include the emission spectra (separated into left and right circular polarizations) of the embedded QDs and the cholesteric stop band. The QD emission spectra reveal clear resonances with the cholesteric cavity for the right-handed component only, as expected. Heating to the isotropic phase removes the resonant structure and the blue (right handed) curve becomes smooth (results not shown). Higher power densities should lead to lasing in a high quality cavity, but in this system lasing was not observed at any applied power. This result may be due to a reduction in cavity quality caused by the large QD-rich aggregates in the system. A large number of Grandjean defects where seen for these materials. In addition, a low concentration overall of emitters when compared with LC/dye lasers is used. These results however demonstrate that the LC ligands do not adversely impact cavity resonance effects. Therefore, by modifying the mesogenic ligand design to produce a uniform QD dispersion at high concentrations it may be possible to induce lasing in these materials.

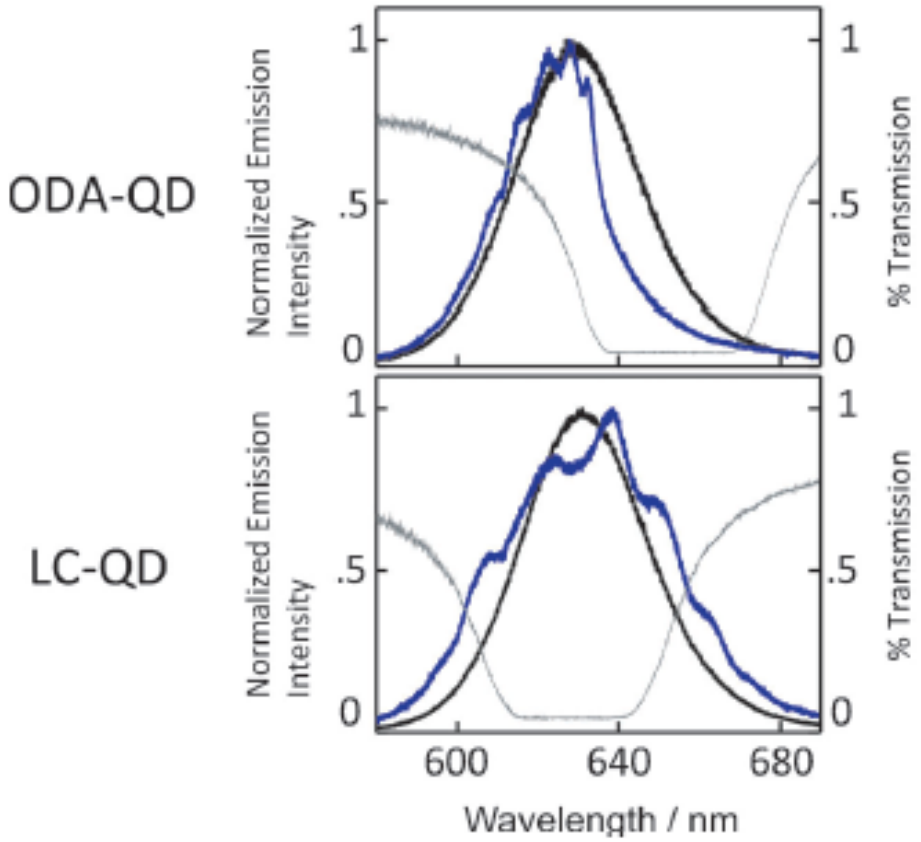

Figure 39: Emission spectra for ODA- and LC–QDs dispersed in a cholesteric material (see Experimental Section) at 0.1 wt% and separated into left handed (black peak) and right-handed (blue peak) components. The cholesteric stop band (transmission spectrum) is also shown (grey) for the righthanded component.

10.3 Conclusion

LC/QD hybrid materials can be potentially applied to new photonic device technologies. Before such ideas can be realized, a clear understanding of particle organization within the host material should be established. Elastic deformations of the nematic director play an important role in phase-separation phenomena and can lead to clustering, aggregation, and even disruption of the host liquid-crystal phase. In addition, at very small length scales, entropic effects can contribute significantly and should be taken into account. We have designed and synthesized a new QD incorporating a mesogenic ligand on a flexible arm capable of aligning with local nematic ordering. We report that core/shell QDs incorporating the LC ligand show excellent dispersion in the isotropic phase and reduced clustering in the nematic phase, with a good dispersion at low concentrations and stable optical performance on ligand attachment. Looking deeper into the structure of the QD clusters for the different ligands, scanning confocal PL microscopy and small angle X-ray diffraction reveal that the LC–QD clusters observed at concentrations above 0.05 wt% are phase-separated liquid-crystalline domains, rich in LC–QDs with an inter-particle separation >12 nm. In a cholesteric device, the new LC–QDs perform comparably to the ODA–QDs but may find use in applications

that take advantage of their fluid like structure for tunable QD assembly.

10.4 Experimental Section

Quantum Dot/Liquid Crystal Mixture Preparation

The different quantum dots are first sonicated in toluene in a sealed glass vial for ~10 mins, then added to a nematic (5CB) or cholesteric (5CB (4-cyano-4'-pentylbiphenyl) and COC (cholesteryl oleyl carbonate) liquid crystal at the required wt%. The mixture is heated to the isotropic phase (above 35ºC for 5CB) and bath-sonicated for eight hours in a glass vial with the cap removed. This method allows the toluene to gradually evaporate from the liquid crystal mixture as the QDs are dispersed. Almost complete toluene removal is verified by measuring the nematic-to-isotropic phase transition point by using differential scanning calorimetry, as this transition is very sensitive to the presence of small amounts of additional solvent. The composite material can then be transferred to a microscope slide or glass capillary. Materials are kept above the isotropic phase transition and carefully cooled at the desired rate for microscopy or X-ray diffraction experiments.

Microscopy and Spectroscopic Methods

Polarized optical microscopy is carried out on a Leica DM2500P upright microscope in the transmission mode with a 10 or 20 objective and Linkam heating stage. Fluorescence microscopy (reflection) can also be carried out on the same microscope without polarizers. For fluorescence imaging of the QDs with a peak emission at 620 nm, a 515–560 nm band-pass filter with white-light mercury lamp illumination was used. Emission was detected using a 580 nm dichroic mirror and a 590 nm Long pass filter. The samples were mounted on standard glass slides under a cover slip, homeotropic liquid crystal alignment was achieved using a CTAB surface coating. Absorption spectral measurements for particles in toluene were performed using a PerkinElmer UV/Vis spectrophotometer.

Photoluminescent scanning confocal microscopy was performed using a custom-built high-resolution scanning confocal microscopy system, as described previously. [1] The excitation sources are several ultrafast, tunable mode-locked lasers that cover the spectral region 350–1200 nm, a high-power Ti:Sapphire laser (MIRA 900), and two optical parametric oscillators (OPO). The excitation is focused on the sample with a high numerical aperture objective. The spot size is diffraction-limited (~600 nm). Glass slides containing the QD/LC material are mounted on a heating stage (Instec Inc.) on a computer-controlled 3D scanning stage. The emission (PL) is collected by the same objective (100X) used for excitation. A spectrometer coupled to a thermo-electrically cooled CCD camera produces spectral images with 1 μm spatial resolution.

X-ray Diffraction

Measurements were carried out at the Stanford Synchrotron Radiation Lightsource, beamline 4–2. Liquid crystal/QD mixtures were prepared at the beamline and filled into 1 mm quartz capillaries; measurements were taken 30 hrs after preparation. The capillaries were mounted in transmission configuration using a custom chamber. Measurements were taken at 11 keV for 1 s per exposure at three spatially separated points on each capillary with a beam size of 0.3x0.1 mm at the sample. The area detector data was analyzed at the beamline using the custom SasTool software.

11 Conclusions

We have demonstrated the viability of using thermotropic liquid crystal materials as an active matrix for quantum dot dispersions. The optical properties of the liquid crystal are capable of manipulating the emission of the quantum dots dispersed within by tuneing the observed peak wavelength of the ensemble as well as amplifying the emission. We have shown that heating the CLC past the isotropic transition temperature is an effective switch for turning off the optical modification but because CLC molecules have a dielectric anisotropy we can also use an applied electric field to switch off the amplification. The cavity created by quantum dots in the cholesteric liquid crystal cavity is weak relative to dye doped LC lasers, so although we have shown that coupling QD emission to the CLC photonic cavity is possible, we still have modifications to do in order to create room temperature QD/LC lasers.

Through replacing the standard octadaecylamine ligands with mesogenic ligands, we have increased our ability to disperse QDs in a nematic liquid crystal with minimal disruption of the LC director. The functionalized QDs more readily disperse in the isotropic LC than the stock QDs, requiring less sonication time, though we observe that high concentrations of QDs persist in creating clusters in the nematic phase. These clusters appear to be more fluid and less close packed than the clusters observed with stock QDs. Preliminary work was done to create a dispersion of these functionalized QDs in a cholesteric liquid crystal. The QDs do cluster in the CLC but the cavity appears to be slightly stronger than that observed in the stock QDs.

Dye doped CLC has been used to create a photonic luminescent solar concentrator. When the CLC stopband is tuned to the absorption of the dye we observe an increase in absorption efficiency but do not see a corresponding increase in PV efficiency. We find that by tuning the stopband of the CLC the emission is more efficiently trapped into the waveguide, minimizing the emission lost though the escape cone due to the planar orientation of the dye molecule.

In addition to making steps toward a homogeneous mixture of QD/LC, we have also demonstrated that the isotropic-nematic LC phase transition can be used as a template for creating clusters of nanoparticles. These micron sized clusters exhibit consistent inter particle spacing which is close enough to allow energy transfer between quantum dots via FRET. This procedure can be expanded for use with different types of nanoparticles, enabling us to create binary clusters with consistent inter particle spacing. The next step in this research is to explore binary systems, moving towards bottom-up fabricated metamaterials.

12 Future Directions

The ability to create ordered clusters of nanoparticles in nematic LC defect sites can be expanded significantly in future work. Our group is currently exploring the addition of magnetic nanoparticles into the clusters[158]. We observe that under a magnetic field the intensity of the QD emission is increased, indicating that the magnetic nanoparticles reorient the cluster, making it more dense while not changing the interparticle separation. These soft assembled clusters respond to low fields of several hundred Gauss which makes them candidates for biosensors.

12.1 Micropillars

We are exploring the potential to further direct the clusters into ordered arrays of columns using micropillars with a homeotropic anchoring surface. Arrays of micropillars of Su-8, an epoxy based negative photoresist, filled with LC have been shown to induce defects in the LC depending on the height of fill. When filled to the top of the LC, defect lines are created at the vertices between pillars. When filled above, the defects are located on top of the pillars[159]. The defect lines should allow us to create columns of nanoparticles. Preliminary work has been started with pillars supplied by Professor Shu Yang's group at the University of Pennsylvania. Table 2 shows a summary of the samples received from Professor Yang's group. The pitch of the pillars determines the defect pattern when filled with LC. Larger pitch lattices induce disclination rings around the top and bottom of the pillar (as seen in Figure 41c), while a short pitch induces defects at interstitials.

Sample	Pillar Diameter (μm)	Pitch (μm)	Height (μm)	Lattice Type
1	10	30	20	square
2	10	40	20	square
3	10	20	50	square
4	10	20	16	square

Table 2: Table of Su-8 pillars received from Professor Yang's group

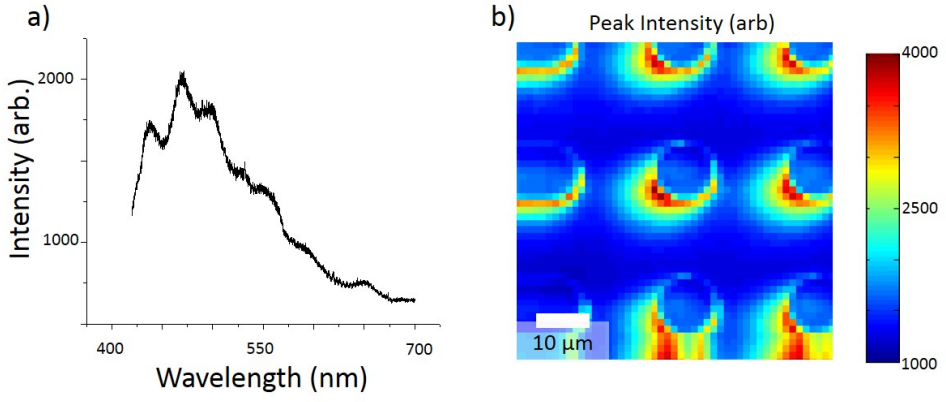

Figure 40: a) PL collected from bare Su-8 pillars on silicon substrate when excited with 409 nm laser and b) PL intensity map of bare pillar sample

To begin preliminary work, I scanned the bare pillars on Si substrate and observed fluorescence

when a 409nm excitation was used as shown in Figure 40a. When scanning the bottom of the substrate, the base of the pillars can be visualized, creating an intensity map shown in Figure 40b. Due to the delicate nature of the pillars, the substrates cannot be cleaned after LC application. For this reason, only a quarter of each substrate should be used at a time. A mixture of 0.02% wt QDs in 5CB was sonicated for 8 hours to create an even dispersion. In a 50 ºC oven, 2 uL of the mixture was dropcast onto two areas of the substrate. One section was covered with a small coverslip and the other was left uncovered. The sample was then cooled at a rate of 0.01 ºC/minute overnight to 25 ºC. The samples were then imaged using polarized optical microscopy and fluorescence microscopy as shown in figure 41.

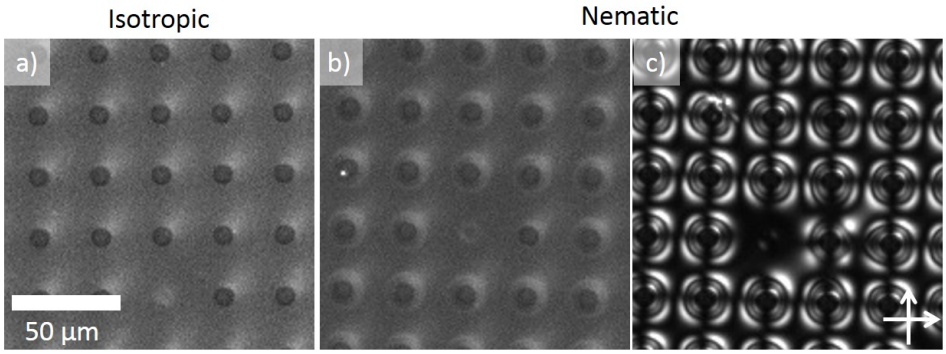

Figure 41: Fluorescence microscopy image of pillars with a) isotropic QD/LC mixture and b) after cooling to the nematic phase as well as c) POM image of the nematic defect texture

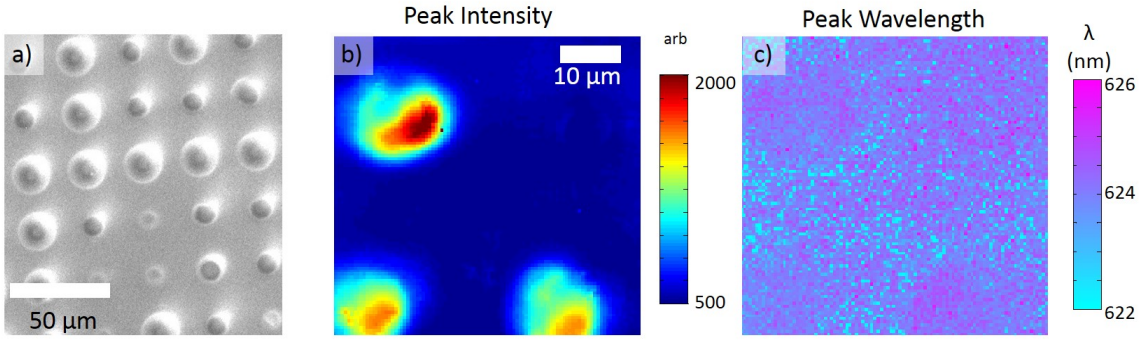

Figure 42: QD/LC mixture over pillars covered by cover slip a) fluorescence microscopy image and b) intensity and c) peak wavelength PL scans showing QD emission

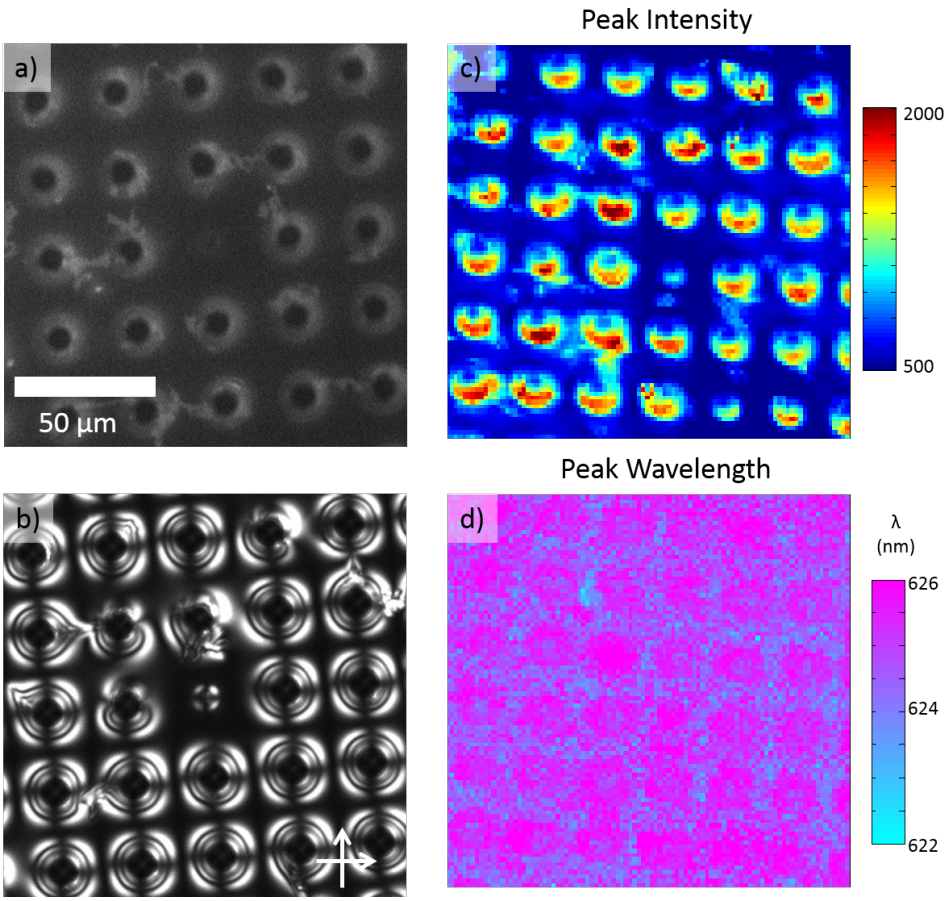

Figure 43: QD/LC mixture over pillars left uncovered a) fluorescence microscopy image along with b) POM image of nematic texture as well as c) intensity and d) peak wavelength PL scans showing QD emission

The samples were then scanned using 409 nm excitation, resulting in the PL maps shown in Figure 42 for the area covered by the coverslip and Figure 43 for the area left uncovered. In these samples we observe that the QDs do collect around the pillars though the effect is much cleaner for the area with the coverslip. There is an asymmetry of the intensity around the pillars due to the fact that the substrate was held at a slight angle off of normal to the laser. Future scans should take care to mount the sample normal to the incident laser. Another difficulty arose because of the emission observed in figure 40a. In future experiments it would be preferable to use a 532nm excitation source to eliminate the background emission.

12.2 LC/QD Laser

With our new QDs functionalized with mesogenic ligands we hope to be able to take steps toward a quantum dot/liquid crystal laser. Preliminary work has been done to assess the coupling between QDs and the CLC photonic cavity. Due to the handedness of CLCs, linearly polarized light does not uni formally observe the photonic cavity. The light with the circular component that matches the handedness of the CLC will observe a reflection band when incident upon the CLC and will observe the photonic cavity when produced inside the CLC. Light with the circular polarization

opposite to the handedness of the CLC will observe neither the reflection band nor the photonic cavity. We probe the QD emission by separating out the two circular components as shown in Figure 44a. The circularly polarized light is first converted to linearly polarized light using a quarter wave plate, resulting in two linear polarizations orthogonal to one another. We separate the linearly polarized light with a Glan laser polarizer which allows us to collect light from either leg. As control samples we prepared films of QD suspended in PMMA and toluene at 0.8 wt% QD in PMMA. The QD/PMMA solution was deposited on glass via spin coater and cured at 140 ºC for one hour. After curing, an alignment layer of PVA was deposited on top of the film as is done for clean glass. The film was then covered with 57.5%, 42.5% COC/5CB mixture to create a photonic cavity that overlaps with the QD emission. A schematic of the cell is shown in Figure 44b. When excited with 532 nm laser light we observe emission from both legs of the setup. It is clear in Figure 44c that one leg contains emission (pink) that is not affected by the reflection band (green) and one that encounters the reflection band of the CLC (blue). It is apparent that the the QD emission within the reflection band is prevented from transmitting through the CLC and we also observe a small amount of coupling and amplification from the edge of the cavity.

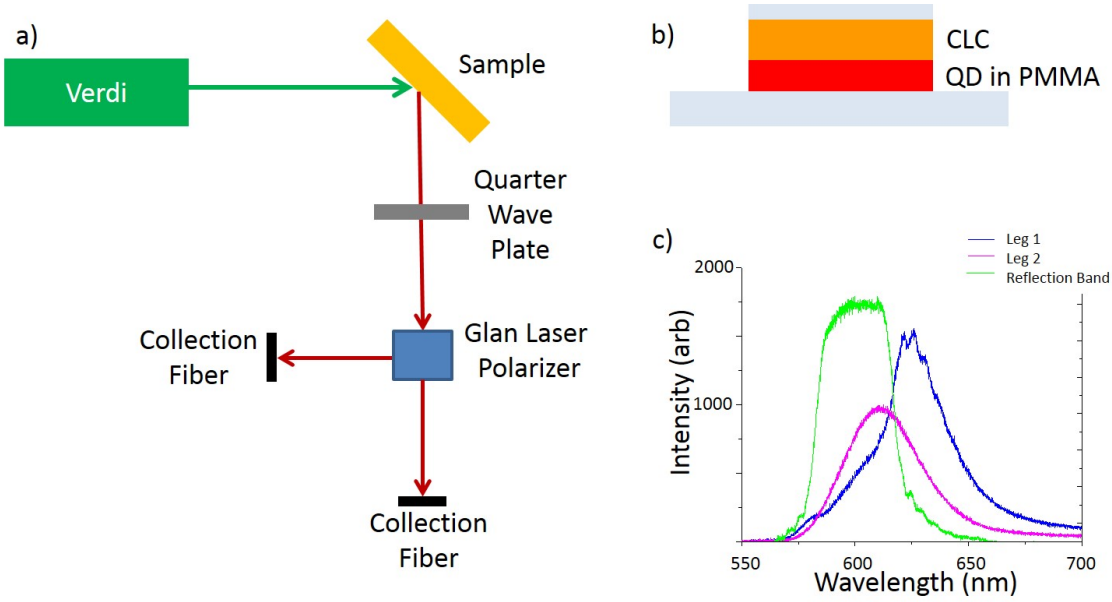

Figure 44: a) Schematic of setup used to collect polarization resolved QD emission, b) schematic of PMMA/QD sample and c) emission collected from both legs overlayed with CLC reflection band

We postulate that the coupling should be stronger when the emission of the QDs originates inside the cavity instead of traveling through it. To test this hypothesis we prepare 0.1 wt% mixtures of stock QDs in CLC as well as 0.1 wt% mixtures of QDs functionalized with mesogenic ligands. Samples were mounted on glass prepared with a planar alignment layer in a 50 ºC oven. The samples were cooled at a rate of 1 ºC/min from the isotropic phase into the nematic phase and left to anneal at 30 ºC overnight. Figure 45a and b show POM images of the cholesteric texture for the stock and functionalized QDs respectively. Notice that the functionalized QDs have formed significant aggregates in the CLC, leading to large defects. When excited by a 532 nm laser we observe the emission of the QDs that couple with the CLC cavity in Figure 45c and d. Both samples appear to couple with the CLC cavity rather than just the functionalized ligands. However, the functionalized

QDs more readily show coupling with the cavity and the amplification is consistently larger than that observed in stock QDs. Moving forward with this project we need to start with a slightly different ligand. At all but very low concentrations we observe significant aggregation in both the stock and functionalized QDs. In order to create a much stronger cavity we must first have an even dispersion that does not foster aggregation due to the disruption of the CLC director. It should also be noted that the collection setup is not as robust as it could be. Some areas of samples display no coupling while others show very strong coupling despite that the sample appears uniform throughout. Through iterations of the setup we were able to increase the consistency of measurements but more work should be done.

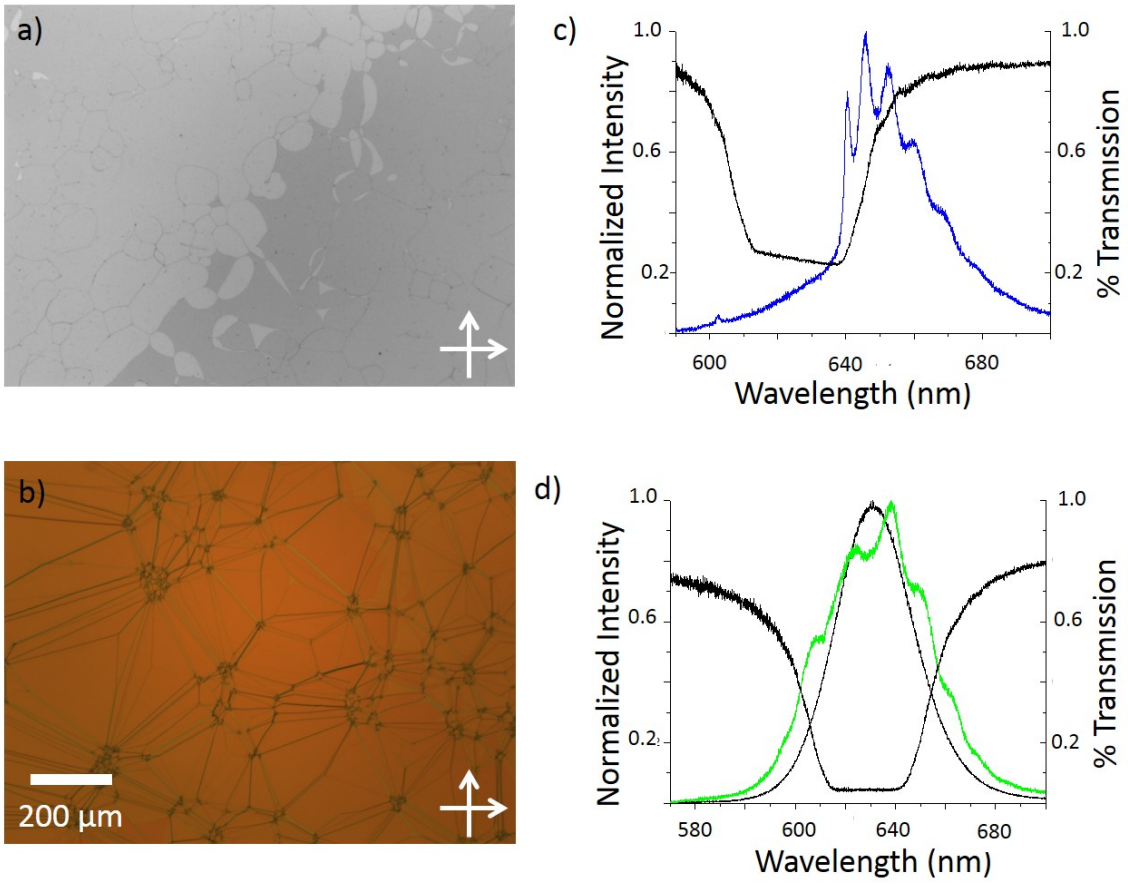

Figure 45: POM images of 0.1 wt% mixtures of a) stock (bw) and b) functionalized QDs (color) in CLC. Emission of embedded QDs in c) stock and d) functionalized QDs

12.3 LC Templated Shells

Though new ligands need to be tried to realize the QD/CLC laser, the current ones can be used to template a new self-assembled structure. Under specific conditions we found that we can form shells of QDs in a nematic LC that are micron sized and hollow in the center which can be seen in Figure 46. The concentration of the QDs in LC must be high, around 0.15 wt% or higher, and the sample must be rapidly cooled. The current technique that consistently creates shells is to transfer

a sample on a planar aligned glass slide from the 50 ºC oven to a 20 ºC plate. The LC undergoes a phase transition in a matter of seconds and the QDs go from an even dispersion to hollow shells. The concentration appears to control the number of shells present and possibly the size of the resulting shells. A confocal scan of the shells can be seen in Figure 46 where the hollow structure is observed. It should be noted that in order to achieve the best resolution from the scanning setup a collection fiber with a 50 μm diameter core must be used. This fiber must then be butt coupled to the standard spectrometer fiber for best results. The preliminary work on the QD shells is very promising, but the ligand exchange process and characterization must be perfected and a concentration study must be performed to determine the true nature of the concentration dependence on the formation of shells. It is possible that instead of concentration, the thickness of the cell may determine the size of the shells, where thicker cells allow for larger shells to form.

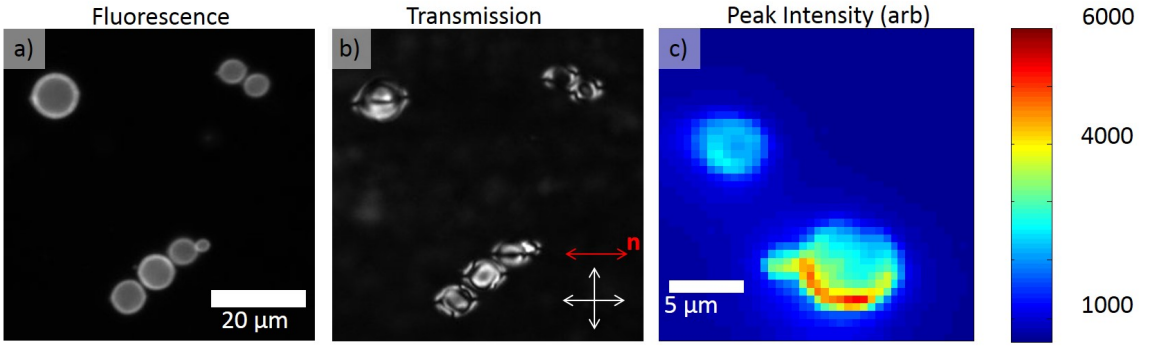

Figure 46: a) Fluorescence and b) POM image of QD shells as well as c) PL map of peak intensity of a shell

From soft assembled metamaterials to three dimensional ordered nanoparticle clusters, using LC materials to assist self-assembly of nanoparticles has shown itself to be a rich field. In addition to creating the clusters, we can modify them by changing the molecular orientation of the LC material either with temperature or electric or magnetic fields. The ability to exchange the stock ligand for a mesogenic one has allowed us to consider many applications that previously could not be realized. More work is needed to allow QDs to integrate more fully into a cholesteric LC though early results are promising. We also have discovered a new structure that can be created with functionalized QDs and the isotropic to nematic phase transition. Once we fully understand the formation of the shells we can experiment with using them to create novel metamaterials that possibly contain magnetic nanoparticles inside the shell or have the outside of the shell decorated with a layer of gold nanoparticles. We have shown that thermotropic liquid crystal materials are a novel and useful matrix for organizing and modifying colloidal nanoparticles.

References

[1] Andrea L. Rodarte, C. Gray, LS Hirst, and S. Ghosh. Spectral and polarization modulation of quantum dot emission in a one-dimensional liquid crystal photonic cavity. *Physical Review B*, 85(3):035430, 2012.

[2] Andrea L. Rodarte, Georgiy V. Shcherbatyuk, Laurel Shcherbatyuk, Linda S. Hirst, and Sayantani Ghosh. Dynamics of spontaneous emission of quantum dots in a one-dimensional cholesteric liquid crystal photonic cavity. *RSC Advances*, 2(33):12759–12763, 2012.

[3] Andrea L Rodarte, Ronald J Pandolfi, Sayantani Ghosh, and Linda S Hirst. Quantum dot/liquid crystal composite materials: self-assembly driven by liquid crystal phase transition templating. *Journal of Materials Chemistry C*, 1(35):5527–5532, 2013.

[4] Andrea L Rodarte, Fredy Cisneros, Linda S Hirst, and Sayantani Ghosh. Dye-integrated cholesteric photonic luminescent solar concentrator. *Liquid Crystals*, (ahead-of-print):1–6, 2014.

[5] Andrea L Rodarte, Zachary S Nuno, Blessing H Cao, Ronald J Pandolfi, Makiko T Quint, Sayantani Ghosh, Jason E Hein, and Linda S Hirst. Tuning quantum-dot organization in liquid crystals for robust photonic applications. *ChemPhysChem*, 15(7):1413–1421, 2014.

[6] Friedrich Reinitzer. BeitrÃ€ge zur kenntniss des cholesterins. *Monatshefte fÃŒr Chemie/Chemical Monthly*, 9(1):421–441, 1888.

[7] Shin-Tson Wu and Deng-Ke Yang. *Fundamentals of liquid crystal devices*. John Wiley & Sons, 2006.

[8] P. J. Collings. *Liquid Crystals: Nature's Delicate Phase of Matter*. Princeton University Press, Princeton, NJ, 2nd edition, 2002.

[9] V. I. Kopp, B. Fan, H. K. Vithana, and a. Z. Genack. Low-threshold lasing at the edge of a photonic stop band in cholesteric liquid crystals. *Optics Letters*, 23(21):1707–1709, nov 1998.

[10] A Muñoz F, P Palffy-Muhoray, B Taheri, et al. Ultraviolet lasing in cholesteric liquid crystals. *Optics letters*, 26(11):804–806, 2001.

[11] Damian J Gardiner, Stephen M Morris, Philip JW Hands, Carrie Mowatt, Rupert Rutledge, Timothy D Wilkinson, and Harry J Coles. Paintable band-edge liquid crystal lasers. *Optics express*, 19(3):2432–2439, 2011.

[12] Linda S. Hirst. *Fundamentals of soft matter science*. CRC Press, 2012.

[13] Hl de Vries. Rotatory power and other optical properties of certain liquid crystals. *Acta Crystallographica*, 4(3):219–226, may 1951.

[14] Olympus. Microscopy resource center. *http://www.olympusmicro.com/primer/techniques/polarized/michel.html*, 2012.

[15] B Kardynal. Introduction to the physics of quantum dots. *Acta Physica Polonica A*, 100(3):275–286, 2001.

[16] Louis Brus. Electronic wave functions in semiconductor clusters: experiment and theory. *The Journal of Physical Chemistry*, 90(12):2555–2560, 1986.

[17] GS Solomon, JA Trezza, AF Marshall, and JS Harris Jr. Vertically aligned and electronically coupled growth induced inas islands in gaas. *Physical review letters*, 76(6):952, 1996.

[18] Alexander W Holleitner, Robert H Blick, and Karl Eberl. Fabrication of coupled quantum dots for multiport access. *Applied Physics Letters*, 82(12):1887–1889, 2003.

[19] A Paul Alivisatos. Perspectives on the physical chemistry of semiconductor nanocrystals. *The Journal of Physical Chemistry*, 100(31):13226–13239, 1996.

[20] Maureen A. Walling, Jennifer A. Novak, and Jason R. E. Shepard. Quantum dots for live cell and in vivo imaging. *International Journal of Molecular Sciences*, 10(2):441–491, 2009.

[21] Prashant V Kamat. Quantum dot solar cells. semiconductor nanocrystals as light harvesters. *The Journal of Physical Chemistry C*, 112(48):18737–18753, 2008.

[22] VL Colvin, MC Schlamp, AP Alivisatos, et al. Light-emitting diodes made from cadmium selenide nanocrystals and a semiconducting polymer. *Nature*, 370(6488):354–357, 1994.

[23] S. Strauf, K. Hennessy, M. T. Rakher, Y.-S. Choi, A. Badolato, L. C. Andreani, E. L. Hu, P. M. Petroff, and D. Bouwmeester. Self-tuned quantum dot gain in photonic crystal lasers. *Phys. Rev. Lett.*, 96:127404, Mar 2006.

[24] A. Imamog¯lu, D. D. Awschalom, G. Burkard, D. P. DiVincenzo, D. Loss, M. Sherwin, and A. Small. Quantum information processing using quantum dot spins and cavity qed. *Phys. Rev. Lett.*, 83:4204–4207, Nov 1999.

[25] J.-H. Choi, A. T. Fafarman, Oh S. J., D.-K. Ko, Kim D. K., Diroll B. T., S. Muramoto, Gillen J. G., Murray C. B., and Kagan C. R. Bandlike transport in strongly coupled and doped quantum dot solids: a route to high-performance thin-film electronics. *Nano letters*, 12(5):2631–2638, 2012.

[26] CP Collier, RJ Saykally, JJ Shiang, SE Henrichs, and JR Heath. Reversible tuning of silver quantum dot monolayers through the metal-insulator transition. *Science*, 277(5334):1978–1981, 1997.

[27] Q. Shao, AA Balandin, AI Fedoseyev, and M. Turowski. Intermediate-band solar cells based on quantum dot supracrystals. *Applied Physics Letters*, 91(16):163503, 2007.

[28] Stanislav Maslovski, Pekka Alitalo, and Sergei Tretyakov. Subwavelength imaging based on frequency scanning. *Journal of Applied Physics*, 104(10):103109, 2008.

[29] Hadiseh Alaeian and Jennifer A Dionne. Plasmon nanoparticle superlattices as optical-frequency magnetic metamaterials. *Optics express*, 20(14):15781–15796, 2012.

[30] Shangjr Gwo, Meng-Hsien Lin, Chieh-Lun He, Hung-Ying Chen, and Toshiharu Teranishi. Bottom-up assembly of colloidal gold and silver nanostructures for designable plasmonic structures and metamaterials. *Langmuir*, 28(24):8902–8908, 2012.

[31] J. Fontana, J. Naciri, R.l Rendel, and B. R. Ratna. Macroscopic self assembly and optical characterization of nanoparticle ligand metamaterials. *Advanced Optical Materials*, 1(1):100–106, 2013.

[32] Hiroshi Yabu. Bottom-up approach to creating three-dimensional nanoring arrays composed of au nanoparticles. *Langmuir*, 29(4):1005–1009, 2013.

[33] Rajratan Basu and Germano S Iannacchione. Evidence for directed self-assembly of quantum dots in a nematic liquid crystal. *Physical Review E*, 80(1):010701, 2009.

[34] Y. K. Verma, R. H. Inman, C. G. L. Ferri, H. Mirafzal, S. N. Ghosh, D. F. Kelley, L. S. Hirst, S. Ghosh, and W. C. Chin. Electrical modulation of static and dynamic spectroscopic properties of coupled nanoscale gase quantum dot assemblies. *Physical Review B*, 82(16):165428, oct 2010.

[35] Delphine Coursault, Johan Grand, Bruno Zappone, Habib Ayeb, Georges Lévi, Nordin Félidj, and Emmanuelle Lacaze. Linear self-assembly of nanoparticles within liquid crystal defect arrays. *Advanced Materials*, 24(11):1461–1465, 2012.

[36] Brandy Kinkead and Torsten Hegmann. Effects of size, capping agent, and concentration of cdse and cdte quantum dots doped into a nematic liquid crystal on the optical and electro-optic properties of the final colloidal liquid crystal mixture. *Journal of Materials Chemistry*, 20(3):448, 2010.

[37] Hao Qi, Brandy Kinkead, Vanessa M. Marx, Huai R. Zhang, and Torsten Hegmann. Miscibility and alignment effects of mixed monolayer cyanobiphenyl liquid crystal capped gold nanoparticles in nematic cyanobiphenyl liquid crystal hosts. *ChemPhysChem*, 10(8):1211–1218, 2009.

[38] Torsten Hegmann, Hao Qi, and Vanessa M. Marx. Nanoparticles in liquid crystals: Synthesis, self-assembly, defect formation and potential applications. *Journal of Inorganic and Organometallic Polymers and Materials*, 17(3):483–508, may 2007.

[39] R. W. Ruhwandl and E. M. Terentjev. Long-range forces and aggregation of colloid particles in a nematic liquid crystal. *Physical Review E*, 55(3):2958–2961, mar 1997.

[40] Sp Meeker, Wc Poon, J. Crain, and Em Terentjev. Colloid-liquid-crystal composites: An unusual soft solid. *Physical review.E, Statistical physics, plasmas, fluids, and related interdisciplinary topics*, 61(6 Pt A):R6083–6, jun 2000.

[41] P. Poulin, H. Stark, T. C. Lubensky, and D. A. Weitz. Novel colloidal interactions in anisotropic fluids. *Science (New York, N.Y.)*, 275(5307):1770–1773, Mar 21 1997. JID: 0404511; ppublish.

[42] Michael D. Lynch and David L. Patrick. Organizing carbon nanotubes with liquid crystals. *Nano Letters*, 2(11):1197–1201, nov 2002.

[43] I. Dierking, G. Scalia, and P. Morales. Liquid crystal & carbon nanotube dispersions. *Journal of Applied Physics*, 97(4):044309, 2005.

[44] Claire Pizzey, Susanne Klein, Edward Leach, Jeroen S van Duijneveldt, and M.Richardson Robert. Suspensions of colloidal plates in a nematic liquid crystal: a small angle x-ray scattering study. *Journal of Physics: Condensed Matter*, 16(15):2479, 2004.

[45] M. Kawasumi, A. Usuki, A. Okada, and T. Kurauchi. Liquid crystalline composite based on a clay mineral. *Molecular Crystals and Liquid Crystals Science and Technology.Section A.Molecular Crystals and Liquid Crystals*, 281(1):91–103, 05/01; 2014/05 1996. doi: 10.1080/10587259608042236; M3: doi: 10.1080/10587259608042236; 05.

[46] M P B van Bruggen and H.N.W.Lekkerkerker F M van der Kooij and. Liquid crystal phase transitions in dispersions of rod-like colloidal particles. *Journal of Physics: Condensed Matter*, 8(47):9451, 1996.

[47] Clayton P. Lapointe, Thomas G. Mason, and Ivan I. Smalyukh. Shape-controlled colloidal interactions in nematic liquid crystals. *Science (New York, N.Y.)*, 326(5956):1083–1086, nov 2009.

[48] Linda S. Hirst, Jennifer Kirchhoff, Richard Inman, and Sayantani Ghosh. Quantum dot self-assembly in liquid crystal media. *Proc. SPIE*, 7618:76180F, 2010.

[49] Rajaa Bitar, Gonzague Agez, and Michel Mitov. Cholesteric liquid crystal self-organization of gold nanoparticles. *Soft Matter*, 7(18):8198, 2011.

[50] Yukihide Shiraishi, Naoki Toshima, Kenji Maeda, Hiroaki Yoshikawa, Jun Xu, and Shunsuke Kobayashi. Frequency modulation response of a liquid-crystal electro-optic device doped with nanoparticles. *Applied Physics Letters*, 81(15):2845, 2002.

[51] U. Tkalec, M. Ravnik, S. Copar, S. Zumer, and I. Musevic. Reconfigurable knots and links in chiral nematic colloids. *Science (New York, N.Y.)*, 333(6038):62–65, Jul 1 2011. JID: 0404511; CIN: Science. 2011 Jul 1;333(6038):46-7. PMID: 21719665; ppublish.

[52] Hiroyuki Yoshida, Yuma Tanaka, Kosuke Kawamoto, Hitoshi Kubo, Tetsuya Tsuda, Akihiko Fujii, Susumu Kuwabata, Hirotsugu Kikuchi, and Masanori Ozaki. Nanoparticle-stabilized cholesteric blue phases. *Applied Physics Express*, 2(12):121501, nov 2009.

[53] P. Borri, W. Langbein, J. M. Hvam, F. Heinrichsdorff, M. . Mao, and D. Bimberg. Ultrafast gain dynamics in inas-ingaas quantum-dot amplifiers. *IEEE Photonics Technology Letters*, 12(6):594–596, jun 2000.

[54] Shoude Chang, Ming Zhou, and Chander Grover. Information coding and retrieving using fluorescent semiconductor nanocrystals for object identification. *Optics express*, 12(1):143–148, jan 2004.

[55] Daniel Loss and David P. DiVincenzo. Quantum computation with quantum dots. *Physical Review A*, 57(1):120–126, jan 1998.

[56] S. M. Feng and T. Chen. Study of polarization state of the transmitted light through the cholesteric liquid crystal. *Displays*, 30(4-5):195–198, dec 2009.

[57] F. Grandjean. The existence of equidistant layers normal to the optic axis in anisotropic liquids (liquid crystals). *CR Hebd Seances Acad Sci*, 172:71–74, 1921.

[58] D. Podolskyy, O. Banji, and P. Rudquist. Simple method for accurate measurements of the cholesteric pitch using a "stripe-wedge" grandjean-cano cell. *Liquid Crystals*, 35(7):789–791, jul 2008.

[59] Marcus Jones, Jovan Nedeljkovic, Randy J. Ellingson, Arthur J. Nozik, and Garry Rumbles. Photoenhancement of luminescence in colloidal cdse quantum dot solutions. *The Journal of Physical Chemistry B*, 107(41):11346–11352, oct 2003.

[60] J. Cheng and B. Meyer. Pretransitional optical rotation in the isotropic phase of cholesteric liquid crystals. *Physical Review A*, 9(6):2744–2760, 1974.

[61] B. Taheri, a. F. Munoz, P. Palffy-muhoray, and R. Twieg. Low threshold lasing in cholesteric liquid crystals. *Molecular Crystals and Liquid Crystals Science and Technology.Section A.Molecular Crystals and Liquid Crystals*, 358(1):73–82, apr 2001.

[62] J. Hu, Li Ls, W. Yang, L. Manna, Wang Lw, and a. P. Alivisatos. Linearly polarized emission from colloidal semiconductor quantum rods. *Science (New York, N.Y.)*, 292(5524):2060–2063, jun 2001.

[63] Mi-Yun Jeong, Hyunhee Choi, and J. W. Wu. Spatial tuning of laser emission in a dye-doped cholesteric liquid crystal wedge cell. *Applied Physics Letters*, 92(5):051108, 2008.

[64] S. G. Lukishova, L. J. Bissell, C. R. Stroud, and R. W. Boyd. Room-temperature single photon sources with definite circular and linear polarizations. *Optics and Spectroscopy*, 108(3):417–424, apr 2010.

[65] P. J. Collings and M. Hird. *Introduction to Liquid Crystals: Chemistry and Physics*. Taylor &; Francis, Philadelphia, 2004.

[66] P. Yeh and C. Gu. *Optics of Liquid Crystal Displays*. John Wiley &; Sons, Inc., Hoboken, 2nd edition, 2010.

[67] EM Purcell. Modification of spontaneous emission. *Phys.Rev*, 69:681, 1946.

[68] John D. Joannopoulos, S. G. Johnson, J. N. Winn, and R. D. Meade. *Photonic Crystals: Molding the Flow of Light*. Princeton University Press, Princeton, 2nd edition, 2008.

[69] S. Strauf, M. T. Rakher, I. Carmeli, K. Hennessy, C. Meier, A. Badolato, M. J. A. DeDood, P. M. Petroff, E. L. Hu, E. G. Gwinn, and D. Bouwmeester. Frequency control of photonic crystal membrane resonators by monolayer deposition. *Applied Physics Letters*, 88:043116, 2006.

[70] T. J. Kippenberg, R. Holzwarth, and S. A. Diddams. Microresonator-based optical frequency combs. *Science (New York, N.Y.)*, 332(6029):555–559, Apr 29 2011. JID: 0404511; ppublish.

[71] DK Armani, TJ Kippenberg, SM Spillane, and KJ Vahala. Ultra-high-q toroid microcavity on a chip. *Nature*, 421(6926):925–928, 2003.

[72] Snjezana Tomljenovic-Hanic, Andrew D. Greentree, C. M. de Sterke, and Steven Prawer. Flexible design of ultrahigh-q microcavities in diamond-based photonic crystal slabs. *Optics express*, 17(8):6465–6475, 2009.

[73] M. Mitov, E. Nouvet, and N. Dessaud. Polymer-stabilized cholesteric liquid crystals as switchable photonic broad bandgaps. *The European physical journal.E, Soft matter*, 15(4):413–419, dec 2004.

[74] Su S. Choi, Stephen M. Morris, Wilhelm T. Huck, and Harry J. Coles. Electrically tuneable liquid crystal photonic bandgaps. *Advanced Materials*, 21(38-39):3915–3918, 2009.

[75] Young-Chol Yang, Chul-Sik Kee, Jae-Eun Kim, Hae Y. Park, Jong-Cheon Lee, and Young-Jae Jeon. Photonic defect modes of cholesteric liquid crystals. *Physical Review E*, 60(6):6852, 1999.

[76] Seiichi Furumi, Shiyoshi Yokoyama, Akira Otomo, and Shinro Mashiko. Electrical control of the structure and lasing in chiral photonic band-gap liquid crystals. *Applied Physics Letters*, 82(1):16, 2003.

[77] Victor I. Kopp, Zhao-Qing Zhang, and Azriel Z. Genack. Lasing in chiral photonic structures. *Progress in Quantum Electronics*, 27(6):369–416, jan 2003.

[78] Ute Resch-Genger, Markus Grabolle, Sara Cavaliere-Jaricot, Roland Nitschke, and Thomas Nann. Quantum dots versus organic dyes as fluorescent labels. *Nature methods*, 5(9):763–775, 2008.

[79] J. Schmidtke and W. Stille. Fluorescence of a dye-doped cholesteric liquid crystal film in the region of the stop band: theory and experiment. *The European Physical Journal B - Condensed Matter*, 31(2):179–194, jan 2003.

[80] Georgy A. Shandryuk, Elena V. Matukhina, Roman B. Vasil, Alexander Rebrov, Galina N. Bondarenko, Alexey S. Merekalov, Alexander M. Gas, and Raisa V. Talroze. Effect of h-bonded liquid crystal polymers on cdse quantum dot alignment within nanocomposite. (Lc):2178–2185, 2008.

[81] PG De Gennes and J. Prost. The physics of liquid crystals, 2nd edn. clarendon. 1993.

[82] AL Rodarte, CGL Ferri, C. Gray, LS Hirst, and S. Ghosh. Directed assembly and in situ manipulation of semiconductor quantum dots in liquid crystal matrices. In *SPIE OPTO*, pages 82790H–82790H–10. International Society for Optics and Photonics, 2012.

[83] S. Crooker, J. Hollingsworth, S. Tretiak, and V. Klimov. Spectrally resolved dynamics of energy transfer in quantum-dot assemblies: Towards engineered energy flows in artificial materials. *Physical Review Letters*, 89(18):186802, oct 2002.

[84] Joseph R. Lakowicz. *Principles of fluorescence spectroscopy*. Springer, 2007.

[85] GV Shcherbatyuk, P Talbot, and S. Ghosh. Controlling photo-induced spectral changes in cdse/zns quantum dots by tuning inter-dot energy transfer. *Applied Physics Letters*, 100(21):212114, 2012.

[86] Jia-Yu Zhang, Xiao-Yong Wang, Min Xiao, and Yong-Hong Ye. Modified spontaneous emission of cdte quantum dots inside a photonic crystal. *Optics Letters*, 28(16):1430–1432, 2003.

[87] B. Gayral, J-M GÃ©rard, B. Sermage, A. Lemaitre, and C. Dupuis. Time-resolved probing of the purcell effect for inas quantum boxes in gaas microdisks. *Applied Physics Letters*, 78(19):2828–2830, 2001.

[88] H. Lohmeyer, C. Kruse, K. Sebald, J. Gutowski, and D. Hommel. Enhanced spontaneous emission of cdse quantum dots in monolithic ii-vi pillar microcavities. *Applied Physics Letters*, 89(9):091107, 2006.

[89] M. Quinten, A. Leitner, JR Krenn, and FR Aussenegg. Electromagnetic energy transport via linear chains of silver nanoparticles. *Optics Letters*, 23(17):1331–1333, 1998.

[90] Chu-Young Cho, Sang-Jun Lee, Jung-Hoon Song, Sang-Hyun Hong, Song-Mae Lee, Yong-Hoon Cho, and Seong-Ju Park. Enhanced optical output power of green light-emitting diodes by surface plasmon of gold nanoparticles. *Applied Physics Letters*, 98(5):051106, 2011.

[91] Alexander O. Govorov, Garnett W. Bryant, Wei Zhang, Timur Skeini, Jaebeom Lee, Nicholas a. Kotov, Joseph M. Slocik, and Rajesh R. Naik. Exciton-plasmon interaction and hybrid excitons in semiconductor-metal nanoparticle assemblies. *Nano Letters*, 6(5):984–994, may 2006.

[92] C. Binns, M. Maher, Q. Pankhurst, D. Kechrakos, and K. Trohidou. Magnetic behavior of nanostructured films assembled from preformed fe clusters embedded in ag. *Physical Review B*, 66(18):184413, nov 2002.

[93] Tae-Ho Kim, Kyung-Sang Cho, Eun K. Lee, Sang J. Lee, Jungseok Chae, Jung W. Kim, Do H. Kim, Jang-Yeon Kwon, Gehan Amaratunga, and Sang Y. Lee. Full-colour quantum dot displays fabricated by transfer printing. *Nature Photonics*, 5(3):176–182, 2011.

[94] Ellen R. Goldman, Igor L. Medintz, Jessica L. Whitley, Andrew Hayhurst, Aaron R. Clapp, H. T. Uyeda, Jeffrey R. Deschamps, Michael E. Lassman, and Hedi Mattoussi. A hybrid quantum dot-antibody fragment fluorescence resonance energy transfer-based tnt sensor. *Journal of the American Chemical Society*, 127(18):6744–6751, may 2005.

[95] X. Michalet, F. F. Pinaud, L. a. Bentolila, J. M. Tsay, S. Doose, J. J. Li, G. Sundaresan, a. M. Wu, S. S. Gambhir, and S. Weiss. Quantum dots for live cells, in vivo imaging, and diagnostics. *Science (New York, N.Y.)*, 307(5709):538–544, jan 2005.

[96] Terry P. Bigioni, Xiao-Min Lin, Toan T. Nguyen, Eric I. Corwin, Thomas A. Witten, and Heinrich M. Jaeger. Kinetically driven self assembly of highly ordered nanoparticle monolayers. *Nature Materials*, 5(4):265–270, 2006.

[97] Andrea Pucci, Marc-Georg Willinger, Feng Liu, Xiangbing Zeng, Valentina Rebuttini, Guylhaine Clavel, Xue Bai, Goran Ungar, and Nicola Pinna. One-step synthesis and self-assembly of metal oxide nanoparticles into 3d superlattices. *ACS nano*, 6(5):4382–4391, 2012.

[98] Denis Andrienko, Guido Germano, and Michael Allen. Computer simulation of topological defects around a colloidal particle or droplet dispersed in a nematic host. *Physical Review E*, 63(4):041701, mar 2001.

[99] Jc Loudet, P. Barois, and P. Poulin. Colloidal ordering from phase separation in a liquid-crystalline continuous phase. *Nature*, 407(6804):611–613, oct 2000.

[100] P. Poulin and D. a. Weitz. Inverted and multiple nematic emulsions. *Physical Review E*, 57(1):626–637, jan 1998.

[101] Makoto Yada, Jun Yamamoto, and Hiroshi Yokoyama. Spontaneous formation of regular defect array in water-in-cholesteric liquid crystal emulsions. 1029(7):7436–7440, 2002.

[102] M. Zapotocky, L. Ramos, P. Poulin, T. C. Lubensky, and D. A. Weitz. Particle-stabilized defect gel in cholesteric liquid crystals. *Science (New York, N.Y.)*, 283(5399):209–212, Jan 8 1999. JID: 0404511; ppublish.

[103] I. Musevic, M. Skarabot, U. Tkalec, M. Ravnik, and S. Zumer. Two-dimensional nematic colloidal crystals self-assembled by topological defects. *Science (New York, N.Y.)*, 313(5789):954–958, Aug 18 2006. LR: 20070319; JID: 0404511; ppublish.

[104] Leonid O. Dolgov and Oleg V. Yaroshchuk. Electrooptic properties of liquid crystals filled with silica nanoparticles of different sorts. *Colloid and Polymer Science*, 282(12):1403–1408, 2004.

[105] A. SzilÃ¡gyi, G. Fetter, and M. ZrÃnyi. Thermotropic behaviour of the complex liquid crystal system containing 8cb [4-cyano-4'-(n-octylbiphenyl)] and organic ferrofluid. *Journal of thermal analysis and calorimetry*, 82(2):525–530, 2005.

[106] Naoki Kanayama, Osamu Tsutsumi, Akihiko Kanazawa, and Tomiki Ikeda. Distinct thermodynamic behaviour of a mesomorphic gold nanoparticle covered with a liquid-crystalline compound. *Chemical Communications*, (24):2640–2641, 2001.

[107] Sandeep Kumar and Laxmi K. Sagar. Cdse quantum dots in a columnar matrix. *Chemical Communications*, 47(44):12182–12184, 2011.

[108] Martin Urbanski, Brandy Kinkead, Torsten Hegmann, and Heinz-S Kitzerow. Director field of birefringent stripes in liquid crystal/nanoparticle dispersions. *Liquid Crystals*, 37(9):1151–1156, sep 2010.

[109] Jonathan Milette, Stephen J. Cowling, Violeta Toader, Cyrille Lavigne, Isabel M. Saez, R. B. Lennox, John W. Goodby, and Linda Reven. Reversible long range network formation in gold nanoparticle-nematic liquid crystal composites. *Soft Matter*, 8(1):173–179, 2012.

[110] Ezequiel R. Soule, Jonathan Milette, Linda Reven, and Alejandro D. Rey. Phase equilibrium and structure formation in gold nanoparticles-nematic liquid crystal composites: experiments and theory. *Soft Matter*, 8(10):2860–2866, 2012.

[111] Javad Mirzaei, Mitya Reznikov, and Torsten Hegmann. Quantum dots as liquid crystal dopants. *Journal of Materials Chemistry*, 22(42):22350–22365, 2012.

[112] B. Y. T. H. Forster. 10th spiers memorial lecture transfer mechanisms of electronic excitation. (10):7–17, 1959.

[113] Cr Kagan, Cb Murray, M. Nirmal, and Mg Bawendi. Electronic energy transfer in cdse quantum dot solids. *Physical Review Letters*, 76(9):1517–1520, feb 1996.

[114] Manuela Lunz, a. L. Bradley, Valerie a. Gerard, Stephen J. Byrne, Yurii K. Gun'ko, Vladimir Lesnyak, and Nikolai Gaponik. Concentration dependence of förster resonant energy transfer between donor and acceptor nanocrystal quantum dot layers: Effect of donor-donor interactions. *Physical Review B*, 83(11):115423, mar 2011.

[115] Gary M. Koenig Jr, Juan J. de Pablo, and Nicholas L. Abbott. Characterization of the reversible interaction of pairs of nanoparticles dispersed in nematic liquid crystals. *Langmuir*, 25(23):13318–13321, 2009.

[116] WH Weber and John Lambe. Luminescent greenhouse collector for solar radiation. *Applied Optics*, 15(10):2299–2300, 1976.

[117] A. Goetzberger and W. Greube. Solar energy conversion with fluorescent collectors. *Applied Physics*, 14(2):123–139, 1977.

[118] JS Batchelder, AH Zewail, and T. Cole. Luminescent solar concentrators. 1: Theory of operation and techniques for performance evaluation. *Applied Optics*, 18(18):3090–3110, 1979.

[119] Jongseung Yoon, Lanfang Li, Andrey V. Semichaevsky, Jae H. Ryu, Harley T. Johnson, Ralph G. Nuzzo, and John A. Rogers. Flexible concentrator photovoltaics based on microscale silicon solar cells embedded in luminescent waveguides. *Nature communications*, 2:343, 2011.

[120] Chun-Hsien Chou, Jui-Kang Chuang, and Fang-Chung Chen. High-performance flexible waveguiding photovoltaics. *Scientific reports*, 3, 2013.

[121] LH Slooff, EE Bende, AR Burgers, T. Budel, M. Pravettoni, RP Kenny, ED Dunlop, and A. Buchtemann. A luminescent solar concentrator with 7.1efficiency. *physica status solidi (RRL)-Rapid Research Letters*, 2(6):257–259, 2008.

[122] Daniel Chemisana. Building integrated concentrating photovoltaics: a review. *Renewable and Sustainable Energy Reviews*, 15(1):603–611, 2011.

[123] Chunhua Wang, Linda S. Hirst, and Roland Winston. Optical design and efficiency improvement for organic luminescent solar concentrators. In *SPIE Optical Engineering Applications*, pages 81240O–81240O–10. International Society for Optics and Photonics, 2011.

[124] Brenda C. Rowan, Lindsay R. Wilson, and Bryce S. Richards. Advanced material concepts for luminescent solar concentrators. *Selected Topics in Quantum Electronics, IEEE Journal of*, 14(5):1312–1322, 2008.

[125] Renata Reisfeld. New developments in luminescence for solar energy utilization. *Optical Materials*, 32(9):850–856, 2010.

[126] Wei LÃŒ, Itaru Kamiya, Masao Ichida, and Hiroaki Ando. Temperature dependence of electronic energy transfer in pbs quantum dot films. *Applied Physics Letters*, 95(8):083102, 2009.

[127] G. V. Shcherbatyuk, R. H. Inman, C. Wang, R. Winston, and S. Ghosh. Viability of using near infrared pbs quantum dots as active materials in luminescent solar concentrators. *Applied Physics Letters*, 96(19):191901, 2010.

[128] RH Inman, GV Shcherbatyuk, D. Medvedko, A. Gopinathan, and S. Ghosh. Cylindrical luminescent solar concentrators with near-infrared quantum dots. *Optics express*, 19(24):24308–24313, 2011.

[129] Sheldon T. Bailey, Gretchen E. Lokey, Melinda S. Hanes, John D. M. Shearer, Jason B. McLafferty, Gregg T. Beaumont, Timothy T. Baseler, Joshua M. Layhue, Dustin R. Broussard, Yu-Zhong Zhang, and Bruce P. Wittmershaus. Optimized excitation energy transfer in a three-dye luminescent solar concentrator. *Solar Energy Materials and Solar Cells*, 91(1):67–75, jan 2007.

[130] Zachar Krumer, Suzanne J. Pera, Relinde J. van Dijk-Moes, Yiming Zhao, Alexander F. de Brouwer, Esther Groeneveld, Wilfried G. van Sark, Ruud E. Schropp, and Celso de Mello DonegÃ¡. Tackling self-absorption in luminescent solar concentrators with type-ii colloidal quantum dots. *Solar Energy Materials and Solar Cells*, 111:57–65, 2013.

[131] G. Maggioni, A. Campagnaro, S. Carturan, and A. Quaranta. Dye-doped parylene-based thin film materials: Application to luminescent solar concentrators. *Solar Energy Materials and Solar Cells*, 108:27–37, 2013.

[132] C. L. Mulder, P. D. Reusswig, a. M. Velázquez, H. Kim, C. Rotschild, and M. a. Baldo. Dye alignment in luminescent solar concentrators: I. vertical alignment for improved waveguide coupling. *Optics express*, 18(9):A79–90, apr 2010.

[133] Ralf B. Wehrspohn and Johannes Upping. 3d photonic crystals for photon management in solar cells. *Journal of Optics*, 14(2):024003, 2012.

[134] M. Peters, JC Goldschmidt, P. Loper, B. Blasi, and A. Gombert. The effect of photonic structures on the light guiding efficiency of fluorescent concentrators. *Journal of Applied Physics*, 105(1):014909, 2009.

[135] Johannes Gutmann, Marius Peters, Benedikt Blasi, Martin Hermle, Andreas Gombert, Hans Zappe, and Jan C. Goldschmidt. Electromagnetic simulations of a photonic luminescent solar concentrator. *Optics express*, 20(102):A157–A167, 2012.

[136] Ivan V. Timofeev, Vasily G. Arkhipkin, Stepan Y. Vetrov, Victor Y. Zyryanov, and Wei Lee. Enhanced light absorption with a cholesteric liquid crystal layer. *Optical Materials Express*, 3(4):496–501, 2013.

[137] Michael G. Debije, My-Phung Van, Paul P. C. Verbunt, Maud J. Kastelijn, Rudy H L. van der Blom, Dirk J. Broer, and Cees W. M. Bastiaansen. Effect on the output of a luminescent solar concentrator on application of organic wavelength-selective mirrors. *Applied Optics*, 49(4):745–751, feb 2010.

[138] Noel C. Giebink, Gary P. Wiederrecht, and Michael R. Wasielewski. Resonance-shifting to circumvent reabsorption loss in luminescent solar concentrators. *Nature Photonics*, 5(11):694–701, 2011.

[139] V. Sholin, J. D. Olson, and S. a. Carter. Semiconducting polymers and quantum dots in luminescent solar concentrators for solar energy harvesting. *Journal of Applied Physics*, 101(12):123114, 2007.

[140] J. Sansregret, JM Drake, WRL Thomas, and ML Lesiecki. Light transport in planar luminescent solar concentrators: the role of dcm self-absorption. *Applied Optics*, 22(4):573–577, 1983.

[141] Nae-Man Park, Tae-Soo Kim, and Seong-Ju Park. Band gap engineering of amorphous silicon quantum dots for light-emitting diodes. *Applied Physics Letters*, 78(17):2575–2577, 2001.

[142] Lei Zhuang, Lingjie Guo, and Stephen Y. Chou. Silicon single-electron quantum-dot transistor switch operating at room temperature. *Applied Physics Letters*, 72(10):1205–1207, 1998.

[143] Jyoti K. Jaiswal, Hedi Mattoussi, J. M. Mauro, and Sanford M. Simon. Long-term multiple color imaging of live cells using quantum dot bioconjugates. *Nature biotechnology*, 21(1):47–51, 2003.

[144] José M Costa-Fernández, Rosario Pereiro, and Alfredo Sanz-Medel. The use of luminescent quantum dots for optical sensing. *TrAC Trends in Analytical Chemistry*, 25(3):207–218, 2006.

[145] AJ Nozik. Quantum dot solar cells. *Physica E: Low-dimensional Systems and Nanostructures*, 14(1):115–120, 2002.

[146] Hao Qi and Torsten Hegmann. Formation of periodic stripe patterns in nematic liquid crystals doped with functionalized gold nanoparticles. *Journal of Materials Chemistry*, 16(43):4197–4205, 2006.

[147] Qingkun Liu, Yanxia Cui, Dennis Gardner, Xin Li, Sailing He, and Ivan I Smalyukh. Self-alignment of plasmonic gold nanorods in reconfigurable anisotropic fluids for tunable bulk metamaterial applications. *Nano letters*, 10(4):1347–1353, 2010.

[148] LJ Martinez-Miranda, Kevin McCarthy, LK Kurihara, Jason J. Harry, and Alexis Noel. Effect of the surface coating on the magnetic nanoparticle smectic-a liquid crystal interaction. *Applied Physics Letters*, 89(16):161917, 2006.

[149] R. Pratibha, W. Park, and II Smalyukh. Colloidal gold nanosphere dispersions in smectic liquid crystals and thin nanoparticle-decorated smectic films. *Journal of Applied Physics*, 107(6):063511, 2010.

[150] Sandeep Kumar and V. Lakshminarayanan. Inclusion of gold nanoparticles into a discotic liquid crystalline matrix. *Chemical communications*, (14):1600–1601, 2004.

[151] Eva Karatairi, Brigita Rozic, Zdravko Kutnjak, Vassilios Tzitzios, George Nounesis, George Cordoyiannis, Jan Thoen, Christ Glorieux, and Samo Kralj. Nanoparticle-induced widening of the temperature range of liquid-crystalline blue phases. *Physical Review E*, 81(4):041703, 2010.

[152] George Cordoyiannis, Venkata S. R. Jampani, Samo Kralj, Surajit Dhara, Vassilios Tzitzios, Georgia Basina, George Nounesis, Zdravko Kutnjak, Chandra S. P. Tripathi, and Patricia Losada-PÃ©rez. Different modulated structures of topological defects stabilized by adaptive targeting nanoparticles. *Soft Matter*, 9(15):3956–3964, 2013.

[153] Yuedong Gu and Nicholas L. Abbott. Observation of saturn-ring defects around solid microspheres in nematic liquid crystals. *Physical Review Letters*, 85(22):4719, 2000.

[154] M. Skarabot and I. MuSevic. Direct observation of interaction of nanoparticles in a nematic liquid crystal. *Soft Matter*, 6(21):5476–5481, 2010.

[155] Wiktor Lewandowski, Kamil Jatczak, Damian Pociecha, and Jozef Mieczkowski. Control of gold nanoparticle superlattice properties via mesogenic ligand architecture. *Langmuir*, 29(10):3404–3410, 2013.

[156] Maksym F. Prodanov, Nataliya V. Pogorelova, Alexander P. Kryshtal, Andrey S. Klymchenko, Yves Mely, Vladimir P. Semynozhenko, Alexander I. Krivoshey, Yurii A. Reznikov, Sergey N. Yarmolenko, and John W. Goodby. Thermodynamically stable dispersions of quantum dots in a nematic liquid crystal. *Langmuir*, 29(30):9301–9309, 2013.

[157] Lin Jer Chen, Jia De Lin, Shuan Yu Huang, Ting Shan Mo, and Chia Rong Lee. Thermally and electrically tunable lasing emission and amplified spontaneous emission in a composite of inorganic quantum dot nanocrystals and organic cholesteric liquid crystals. *Advanced Optical Materials*, 1(9):637–643, 2013.

[158] JJ Amaral, J Wan, AL Rodarte, MT Quint, RJ Pandolfi, M Scheibner, LS Hirst, and Ghosh S. Magnetic field controlled synergistic brightening in magnetic/semiconducting nanoparticle clusters mediated by liquid crystalline molecules. *Advanced Materials*, submitted, 2014.

[159] Apiradee Honglawan, Daniel A Beller, Marcello Cavallaro, Randall D Kamien, Kathleen J Stebe, and Shu Yang. Pillar-assisted epitaxial assembly of toric focal conic domains of smectic-a liquid crystals. *Advanced Materials*, 23(46):5519–5523, 2011.